Winter 11-20-2020

Boron Adsorption In Clay Minerals: Implications for Martian Groundwater Chemistry And Prebiotic Processes

Matthew A. Nellessen
University of New Mexico

Laura Crossey
University of New Mexico

Patrick J. Gasda
Los Alamos National Laboratory

Horton Newsom
University of New Mexico

Abdulmehdi Ali
University of New Mexico

See next page for additional authors

Matthew Nellessen

Candidate

Earth & Planetary Sciences

Department

This thesis is approved, and it is acceptable in quality and form for publication:

Approved by the Thesis Committee:

Laura Crossey , Chairperson

Patrick Gasda

Horton Newsom

Adrian Brearley

Boron Adsorption In Clay Minerals: Implications For Martian Groundwater Chemistry And Prebiotic Processes

By

Matthew Nellessen

B. S., Geology, University of New Mexico, 2018

THESIS

Submitted in Partial Fulfillment of the

Requirements for the Degree of

Master of Science

Earth and Planetary Sciences

The University of New Mexico

Albuquerque, New Mexico

December 2020

Acknowledgements

I would like to thank all of the support and assistance I have received from my family, friends, professors, and everyone else who has helped me along the way in my education. All of the support from my family and friends has helped me to push through my studies and given me the drive to pursue graduate school.

I would like to thank all of the research staff and technicians I have worked with over the years, especially Dr. Abdulmehdi Ali with all of his help with Inductively Coupled Plasma Optical Emission Spectroscopy analysis and the numerous experiments I ran in his lab. I would like to thank Dr. Mike Spilde for all of his assistance for his assistance and obtaining analysis using electron microprobe and scanning electron microscope. I would like to thank Dr. Eric Peterson for his help with x-ray diffraction analysis and all of his insight into clay mineral structure and knowledge. I would like to thank Adriana Reyes-Newell and Sam Clegg and the rest of the LIBS lab at Los Alamos National Laboratory for their assistance and analysis with the LIBS instrument. I would also like to thank Paula Pascetti, Faith Mutchnik, and Mabel Chavez and the rest of the EPS administration for their help through the years.

I would like to thank my committee members, Dr. Laura Crossey, Dr. Patrick Gasda, Dr. Horton Newsom, and Dr. Adrian Brearley for all their help and support with this study.

I would especially like to thank Dr. Horton Newsom, who helped me fuse my love of geology and space into planetary geology, and has been helping me to understand and progress in this field ever since. I thank Dr. Laura Crossey for all of her help and teaching of geochemistry over the past two years and always being available for any questions I had. I thank Dr. Patrick Gasda for introducing me to this project and for all of the professional insight and support he has provided over the past two years. His strong support for me and my research has always made me feel like a welcome member of the Mars community and his positive attitude to see me succeed has kept me driven to pursue this field. I am indebted to everyone’s support for everything I have done.

This study was supported by Los Alamos National Laboratory and Laboratory Directed Research and Development Exploratory Research, the University of New Mexico, and NASA Mars Exploration Program.

Boron Adsorption In Clay Minerals: Implications For Martian Groundwater Chemistry And Prebiotic Processes

By

Matthew Nellessen

B.S., Earth and Planetary Sciences, University of New Mexico, 2018

M.S., Earth and Planetary Sciences, University of New Mexico, 2020

Abstract

Boron has been detected on Mars [*Gasda et al.*, 2017, *Das et al.*, 2019, 2020] within calcium-sulfate veins found within clay-rich rocks on Mars by the Mars Science Laboratory (MSL) rover using Laser Induced Breakdown Spectroscopy (LIBS) analysis. Boron plays a vital role in stabilizing ribose on Earth and has been suggested as a key requirement for life [*Scorei et al.*, 2006, 2012; *Furukawa et al.*, 2013, 2017; *Becker et al.*, 2019]. Additionally, boron readily adsorbs to phyllosilicate clay minerals and is often associated with biologic processes in clay soils. The discovery of boron on Mars in proximity to phyllosilicate bedrock may have strong implications for potential past prebiotic conditions on Mars. This study generates a suite of clays with sorbed boron, including both typical terrestrial clays as well as Mars-analog clays, to understand the controls on boron adsorption and to examine these clay materials with LIBS in an effort to develop standards for future analyses on Mars. These standards can also help to better understand past analyses where boron has been detected. Geochemical and XRD characterization of the suite of clays was also conducted, including a clay collected from boron deposits of the western United States. Characterization analysis determined the baseline chemistry of the clays prior to adsorption and also revealed the purity of the clays. The samples of clays, while predominantly consisting of the expected Fe/Mg phyllosilicate typical of Mars, also contain minor and trace amounts of other minerals. These samples may therefore better represent the impure clay-bearing rocks on Mars. Adsorption analysis revealed that the montmorillonite clays were able to adsorb a significant amount of boron, which was greater than seen in previous literature, although this study attributes this to different experimental conditions. Analysis also determined that there is a positive correlation between concentration of boron in the fluid and final adsorbed concentration of boron on the clay. Experiments concerning the time factor indicated that adsorption happens quickly as

extended exposure to borate fluid did not increase boron adsorption. Further studies will adsorb boron to selected clays at varying pH conditions to analyze the ideal conditions for boron sorption and compare which clay types adsorb boron most effectively. The results of this study provides insight into boron sorption onto Mars-analog clays. Boron-rich clays were created that can be exposed to ribose for organic analysis in follow-up studies. A series of boron-enriched standards were also created that can be used by the MSL and future Mars 2020 rovers. The results of this study may also provide insight into Martian groundwater geochemistry processes and the problems concerning the apparent lack of Martian evaporite deposits.

Table of Contents

List of Figures

List of Tables

Introduction

Boron is an element found in low concentrations in organic-rich soils on Earth affected by biologic activity [*Karahan et al.*, 2006]. Boron is a lightweight element of atomic number 5 and atomic weight of 10.811 g/mol. Boron has a valence of 3 and typically appears as a cation with a charge of +3. Elemental boron does not occur naturally on Earth and boron is typically found in the form of borate minerals or in aqueous solution. When in solution boron appears typically as either borate (BO_3^{3-}) or boric acid (H_3BO_3), (**Figure 1**) depending on the pH of the solution. Boric acid is a weak acid: the turnover from boric acid being abundant at lower pH to borate at higher pH occurs at the pH corresponding to the first acid dissociation constant around pH 8-9.

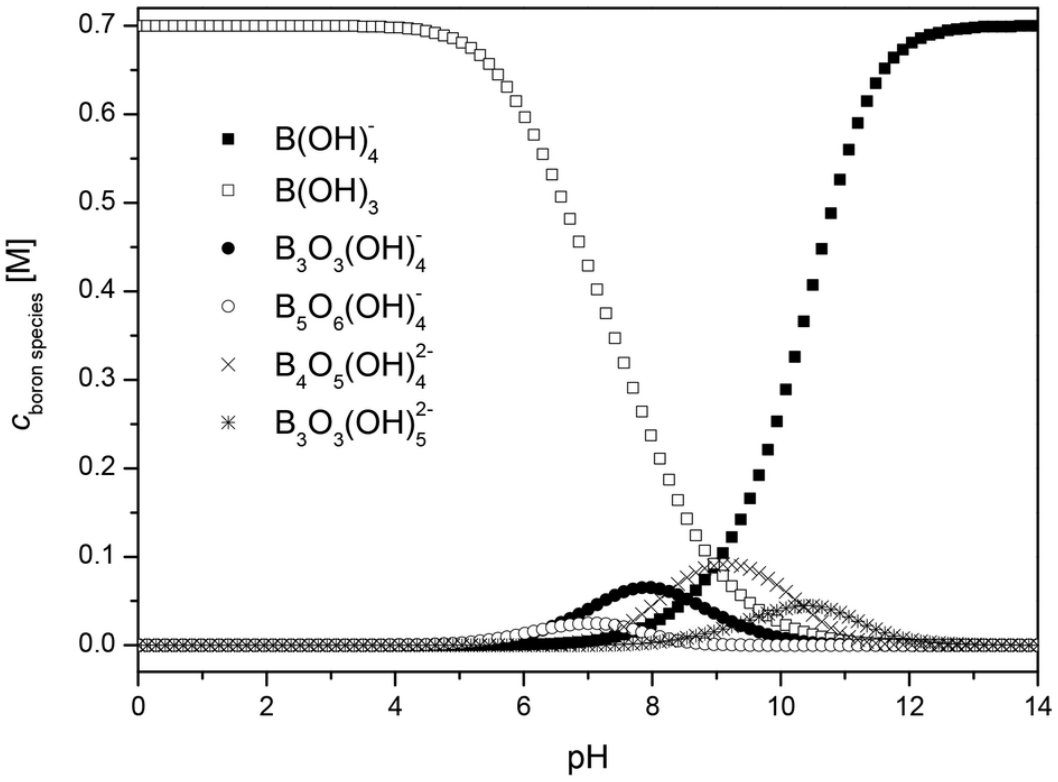

Figure 1: Predominance diagram for boric acid/borate ions (*Schott et al.*, 2014). pKα is at 9.24 between H_3BO_3 and $H_2BO_2^-$ (Drever, 1997).

Boron is typically found as borate in clay-rich environments bound to 2:1 phyllosilicates [*Keren*, 1981; *Goldberg et al.*, 1993, 1997, 2008] when introduced by groundwater or other fluid process to allow boron adsorption [*Keren*, 1981]. The pH of the borate-carrying water affects how well the soil takes up boron. Experimental work has found that a pH range of 8-9 [*Karahan et al.*, 2006; *Keren*, 1981; *Goldberg et al.*, 1993, 2008] provides the most adsorption to levels of 250-500 ppm B onto the clay [*Karahan et al.*, 2006]. As Martian groundwater is likely to have been neutral or alkaline [*Grotzinger et al.*, 2014], this means that Martian groundwater was optimal for boron uptake by clay minerals. Recently, boron was detected in Martian calcium sulfate veins by ChemCam on the NASA *Curiosity* rover in relatively significant quantities up to 300 ppm B within the veins [*Gasda et al.*, 2017, *Das et al.*, 2019].

The MSL Curiosity rover landed in Gale crater in 2012 with the intent of exploring and analyzing the ancient sediments of the crater. Gale crater lies near the boundary of the younger northern lowlands from the older southern highlands. The rover's mission objectives include understanding the past environmental conditions on Mars as well as investigating the potential for past habitability of Mars [*Grotzinger et al.*, 2012]. Gale crater was formed as the result of a meteoritic impact ~3.7 Ga and has a large central mound of sedimentary material, Aeolis Mons (informally referred to as Mount Sharp) [*Milliken et al.*, 2010; *Schwenzer et al.*, 2012; *Newsom et al.*, 2015]. This central uplift is surrounded by mostly mound deposits. The rover landed at Aeolis Palus at the Bradbury landing, which is a member of the Bradbury formation containing mixed sandstones and mudstones [*Grotzinger et al.*, 2014]. The rover traversed to the location referred to Yellowknife Bay on sols ~100-300 before proceeding to traverse its way up Mount Sharp encountering the Murray formation, which has been a large unit consisting mostly of mudstones [*Rampe et al., 2017*]. Above the Murray formation still lies the layered sulfate unit, which may

contain primary evaporite deposits [*Fraeman et al.*, 2016; *Milliken et al.*, 2010]. The abundance of layered sandstones and mudstones, as well as the presence of other sedimentary features such as mud cracks and ripples, indicate the presence of an ancient lacustrine playa lake environment [*Grotzinger et al.*, 2014]. The ChemCam instrument suite is mounted on top of the rover mast, and includes the Laser Induced Breakdown Spectroscopy (LIBS) and Remote Micro Imager (RMI) instruments.

Boron is found throughout the rover's traverse (**Figure 2**), though notably more frequently in the Murray. It is typically found within calcium sulfate filled fractures hosted within phyllosilicate-bearing bedrock [*Morrison et al.*, 2018 ; *Vaniman et al.*, 2014; *Rampe et al.*, 2017; *Bristow et al.*, 2018]. The structure of 2:1 phyllosilicates (**Figure 3**), including smectites, is a strong facilitator for boron adsorption to exposed mineral surfaces. Smectites are a dominant phyllosilicate seen in the Martian bedrock at Gale Crater [*Vaniman et al.*, 2014]. Boron is only detected within the calcium-sulfate veins, and given that these veins are found within smectite-rich bedrock, these smectites have potential to be hosting relatively large quantities of boron. Different phyllosilicates have variable structures and chemistry (**Figure 4**), meaning that the level of adsorption of boron can vary significantly from clay to clay, so in-depth individual clay analysis is necessary for understanding how well boron reacts to specific clays. Adsorption is typically interpreted to occur on the edges of clay surfaces (*Karahan et al.*, 2006; *Keren*, 1981). Boron was likely deposited by groundwater carrying material from dissolved borate-bearing evaporites [*Gasda et al.*, 2017]. Boron adsorption occurs mostly in low temperature environments during early burial diagenesis. At higher temperatures, boron may substitute into the clay structure, replacing Al^{3+} or other deflect sites [*You et al.*, 1996; *Spivack et al.*, 1987; *Williams et al.*, 2001; *Couch*, 1968]. Most evidence suggests that groundwater fluid temperatures at Gale crater did not exceed 50° C, as seen by the

abundance of gypsum found within calcium-sulfate veins as well as very little evidence of extensive illite formation in Gale crater [*Gasda et al.*, 2017; *Vaniman et al.*, 2014; *Bristow et al.*, 2015, 2018]. As the groundwater temperature at Gale likely remained low, any boron in the system would favor adsorption over replacement. Had high temperatures (> 60 °C) been experienced by these exposed materials, anhydrite would have been the sulfate phase, and smectites would have altered to illite [*Pytte et al.*, 1989]. This study will explore the conditions of low-T adsorption.

Boron on Earth is found in low quantities all over the earth, but when found in high concentrations it typically appears in the form of large-scale borate deposits, as seen in Death Valley, California [*Crowley*, 1993; *Tanner*, 2002; *Lowenstein et al.*, 1999] as well as in Turkey and Argentina [*Kasemann et al.*, 2004]. Boron most frequently forms as the mineral colemanite or ulexite [*Crowley*, 1993], an evaporite mineral described in playa lake deposits. This poses similarities to the situation on Mars as Gale Crater is also interpreted to have hosted a paleolake lacustrine depositional environment featuring several evaporite minerals [*Rampe et al.*, 2017; *Schwenzer et al.*, 2016] embedded within the bedrock of its generally mudstone bedrock [*Grotzinger et al.*, 2014]. Similarly, in Jezero crater, the landing site for the Mars 2020 rover, also contains evaporite minerals in the form of carbonates detected from orbital data [*Horgan et al.*, 2020].

Boron often originates from igneous sources [*Kasemann et al.*, 2004] which then is released from host materials through exposure to surface or groundwater conditions and then mobilized in groundwater [*Tanner*, 2002]. This readily isolates boron to be deposited as borate in terrestrial settings. However, a considerable amount of igneous bedrock needs to be weathered to accumulate high concentrations of boron. Basaltic rock typically contains between 0.5 up to 10 ppm B, while felsic rocks may contain up to 100 ppm B [*Ishikawa et al.*, 1992; *Spivack et al.*, 1987; *Chaussidon*

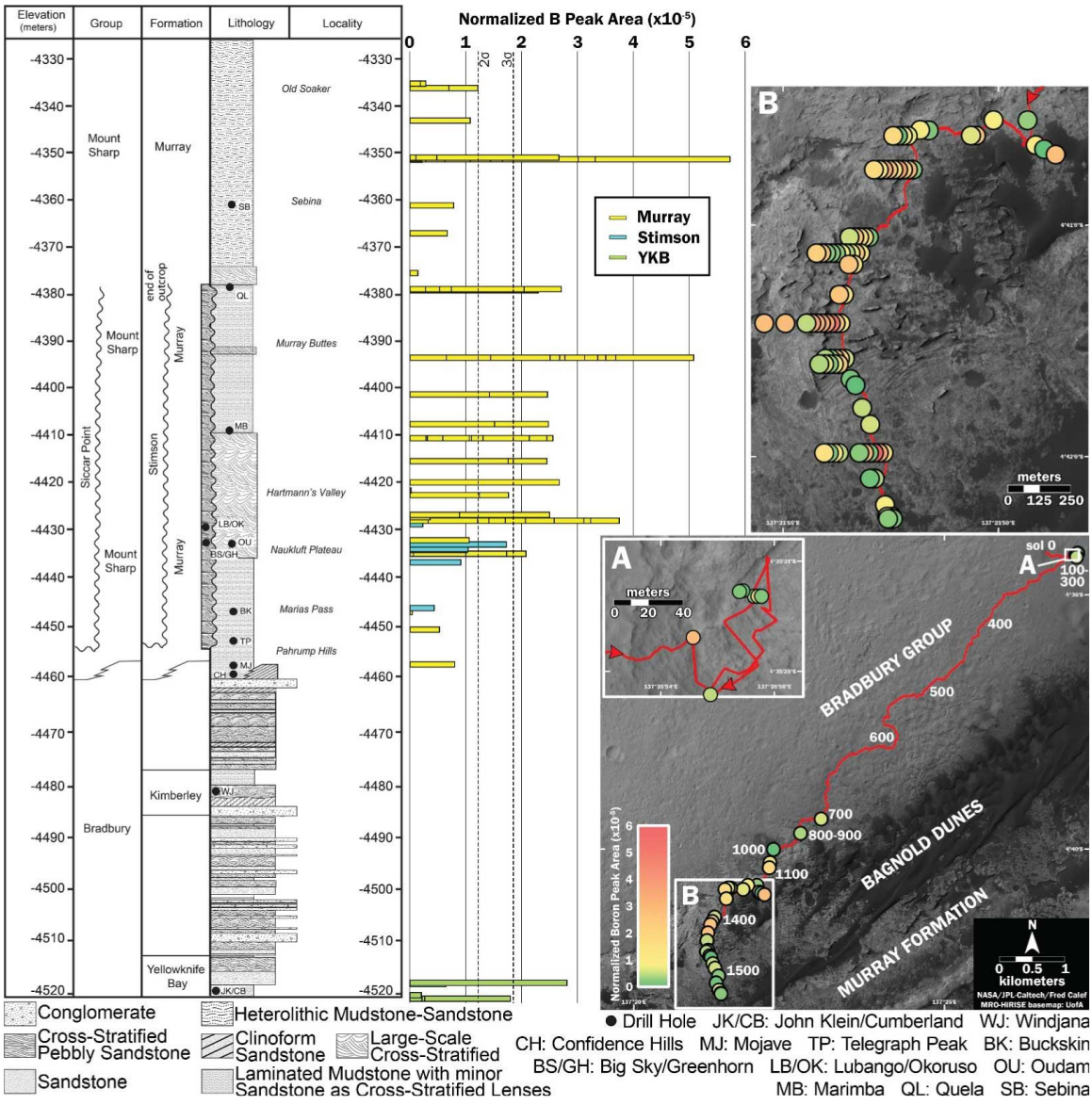

Figure 2: Stratigraphic Column of Gale Crater, detected boron targets, and orbital imagery of MSL traverse. Images A and B display locations of boron detection and these are displayed by frequency next to the stratigraphic column. Boron detection increased upon reaching the Murray Formation, where mudstones and clay-bearing units are more abundant, leading to linkage between boron and clay minerals in Gale Crater. (Figure *Gasda et al.*, 2017)

et al., 1994; *Mohan et al.*, 2008]. As bedrock contains very small quantities of boron, a considerable amount of bedrock needs to be weathered to generate high concentrations of boron. As felsic rocks generally contain more boron, it is therefore easier to accumulate boron in a more felsic environment, as compared to a more basaltic one. Evidence points to the southern highlands

of Mars as being a strong felsic source [*Bernhardt et al.*, 2018; *Sautter et al.*, 2019] and its highly likely that some of this material was brought into Gale crater and it eventually broke down there. Some rocks in Gale crater have been determined to be trachytes and rhyolites [*Cousin et al.*, 2017; *Payre et al.*, 2020; *Rampe et al.*, 2019; *Morris et al.*, 2016], which is indication of a more evolved magma (felsic) and are therefore able to concentrate more boron. So, although boron is very soluble and weathers very easily, its natural concentrations in source rocks is very small and therefore it would take a lot of active water to weather a lot of bedrock in order to concentrate boron in the concentrations seen in Gale crater. Given that there are magnesium sulfates in Gale Crater [*Rapin et al.*, 2019; *Nachon et al.*, 2017; *Milliken et al.*, 2010], which are very soluble and only precipitate out during major drying events, it can be inferred that there was indeed a lot of water available in order to weather a large amount of bedrock.

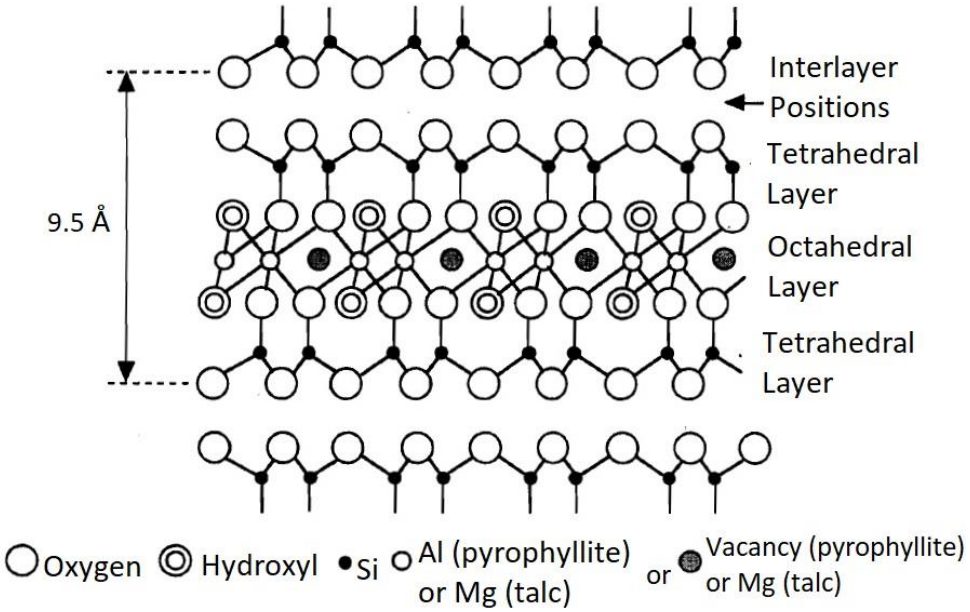

Figure 3: Standard 2:1 phyllosilicate structure, the ideal set-up for the boron adsorption assisted by fluid transport. Octahedral cation is Al/Mg (pyrophyllite/talc) and interlayer positions are empty but may contain cations or water in intermediate members. Boron is assumed to adsorb to exposed, broken mineral surfaces (Figure 2A from *Drever,* 1997)

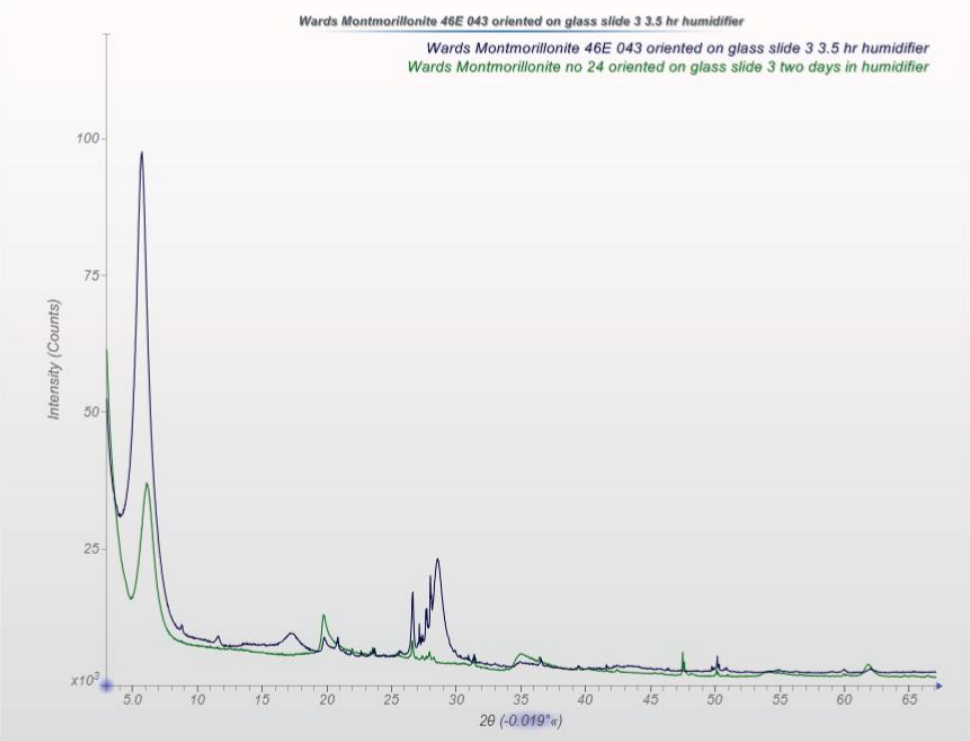

Figure 4: XRD analysis of two bentonite standards demonstrating variability between similar clay samples.

However, large-scale evaporite deposits such as those found on Earth have not yet been seen in Gale crater, despite there being evidence of chloride salts [*Osterloo et al.*, 2008, 2010; *Hynek et al.*, 2015, *Ehlmann et al.*, 2015] and carbonates [*Horgan et al.*, 2020] elsewhere on Mars. This has been a long-standing issue as one expects to find evaporite deposits in a large, ancient paleolake environment that dried out. Evaporite minerals, such as calcium-sulfate, are abundant on Mars in the form of veins [*Nachon et al.*, 2014] or embedded in bedrock, yet not as large outcrops. This is hypothesized to be due to a short period of acid diagenesis [*Rampe et al.*, 2017] and redissolution [*Schwenzer et al.*, 2016], which weathered away highly soluble evaporite minerals and incorporated them into groundwater and dispersed them throughout the bedrock into pore space or by infilling fractures. This may explain why boron is incorporated into Ca-sulfate veins (*Gasda et*

al., 2017). While this concentrated borate solution was being carried by groundwater, it would have come into contact with clay surfaces, allowing a prime opportunity for adsorption. The large-scale evaporites were primary deposits that formed when the Gale paleolake system was still active, roughly 3.5 Ga [*Grotzinger et al.*, 2014; *Frydenvang et al.*, 2017]. The "layered sulfate unit," one of the lithologic units in Gale crater, has been theorized to be a potential primary evaporite deposit and may lead to clues about the source of the boron in Gale crater [*Fraeman et al.*, 2016; *Milliken et al.*, 2010].

As borate typically occurs naturally as evaporite deposits, it also dissolves in solution and is therefore often found in aqueous solutions. Boron is readily taken up by clay minerals [*Keren*, 1981; *Goldberg et al.*, 1993, 1997, 2008] and is therefore often found within sedimentary environments where clays are abundant. Clay minerals come in a variety of species including dioctahedral vs trioctahedral mineral species and 2:1 vs 1:1 clays. Dioctahedral clays contain two cations in octahedral coordination with a vacancy in the third position in order to maintain charge balance [*Drever*, 1997, p.74; **Figure 3**]. This configuration is more common for higher charge cations such as Fe^{3+} or Al^{3+}. In trioctahedral clays, all three octahedral sites are filled with a lower charge cation such Fe^{2+} or Mg^{2+} with no vacancies to maintain charge balance. 2:1 vs 1:1 clays refers to the configuration of the structure of the mineral concerning the octahedral and tetrahedral layers. A 1:1 set-up involves a single tetrahedral layer bonded to a single octahedral layer, whereas a 2:1 structure has two tetrahedral layers separated by a single octahedral layer in between. On Mars a combination of dioctahedral and trioctahedral clays are seen, but they are both typically found in a 2:1 set-up. For this reason, the clays used in this study fall into the category of 2:1 clays and are a mix of dioctahedral and trioctahedral.

Adsorption is defined as the bonding of solid particles or ions onto the surface of another material, in this case where boron or borate is chemically bonded to the surface of clay minerals. Cation exchange is the process by which a material, such as a clay, is able to attract and substitute cations (although borate exist as anions) from the surrounding solution into its own structure or onto its surface [*Birkeland*, 1999]. Cation exchange capacity is net surface charge, usually negative, of the mineral surface [*Birkeland*, 1999]. Cation exchange capacity is dependent on the overall charge of the material and cations in solution. Most soils, which typically are abundant in clay minerals, tend to have an average negative surface charge [*Birkeland*, 1999], although in alkaline water conditions, clays often will contain positive sites suitable for attracting borate anions. This makes clays especially suited for adsorption, as they will naturally tend to attract these cations to the surface of the clays. Then there is the difference between inner and outer sphere complexes, which dictates how the cation binds to the mineral surface (**Figure 5**). An inner sphere complex involves the cation bonding directly to the exposed, broken mineral surfaces and results in stronger bonds

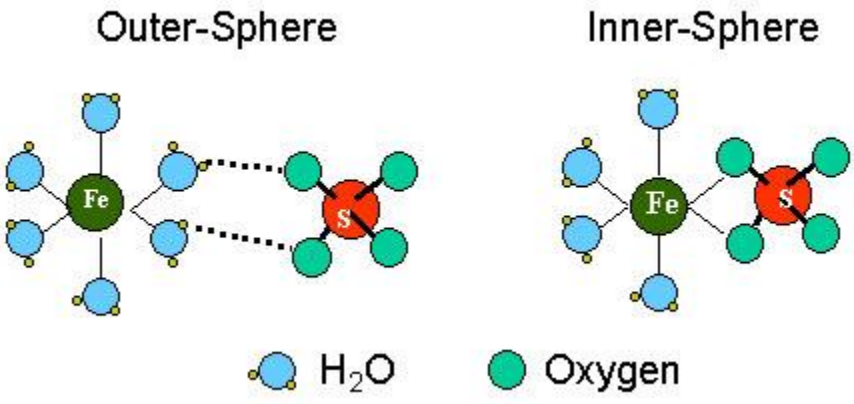

Figure 5: Adsorption differences between inner and outer sphere adsorption complexes. [Molecular complexation. Princeton]

and no dependence on electrostatic dependence [*Drever*, 2002]. An outer sphere complex involves the cation being encased in a hydration shell and bonding is therefore indirect and dependent on electrostatic attraction. While outer sphere complexes tend to favor major cations (Na^+, K^+, Ca^{2+}, Mg^{2+}) with trace elements being displaced to solution, inner sphere complexes may better facilitate adsorption of minor and trace elements [*Drever*, 2002]. This would imply that boron adsorption is likely occurring in inner sphere systems and is therefore directly bonded to the mineral surface.

Boron is hypothesized to be a vital aspect for prebiotic processes to occur on Earth and possibly on Mars [*Scorei et al.*, 2012]. The formation of boron-ribose complexes [*Cafferty et al.*, 2014; *Georgelin et al.*, 2015; *Grew et al.*, 2011; *Larralde et al.*, 1995; *Swadling et al.*, 2010; *Hashizume*, 2015] might allow the formation of ribonucleic acid (RNA), a critical component for life. Borate-ribose complexes are relatively stable in water; without borate, ribose will quickly break down in solution [*Georgelin et al.*, 2015; *Larralde et al.*, 1995; *Chapelle et al.*, 1988]. With boron found on Mars, this poses implications for the habitability of life on Mars [*Scorei et al.*, 2012; *Gasda et al.*, 2017]. The potential for finding prebiotic conditions on Mars is of great interest for Mars research as searching for signs of life or habitability is one of the central mission objectives for both the MSL rover, but also for NASA and the whole of planetary science.

Previous Experimental Work

There has been considerable study of boron adsorption onto clays in terrestrial settings [*Couch*, 1968; *Karahan et al.*, 2006; *Keren*, 1981; *Keren et al.*, 1994; *Okay et al.*, 1995; *Chen et al.*, 2009; *Goldberg et al.*, 1996; *Fleet*, 1965; *Harder*, 1970; *Perry*, 1972; *Yingkai et al.*, 2001]. Experimental findings find that boron ideally adsorbs to 2:1 phyllosilicates. The optimum pH varies slightly from mineral to mineral (**Figure 6**), but the general pH range between 6 and 10 fosters the highest

amount of adsorption of boron onto the clay mineral. The three clays used by [*Karahan et al.*, 2006] were sepiolite, bentonite, and illite, with a decreasing level of boron adsorption respectively. Both illite and bentonite see peak adsorption around a pH of 8, while sepiolite sees peak adsorption around a pH of 9. The Karahan experimental method forms the base for the experimental method used in this study; however, illite and sepiolite are not used in this study and instead this study examines saponite and nontronite, due to their detected presence on Mars [*Vaniman et al.*, 2014]. Other minor adjustments were made to the adsorption procedure to allow better sorption of the boron to the clays.

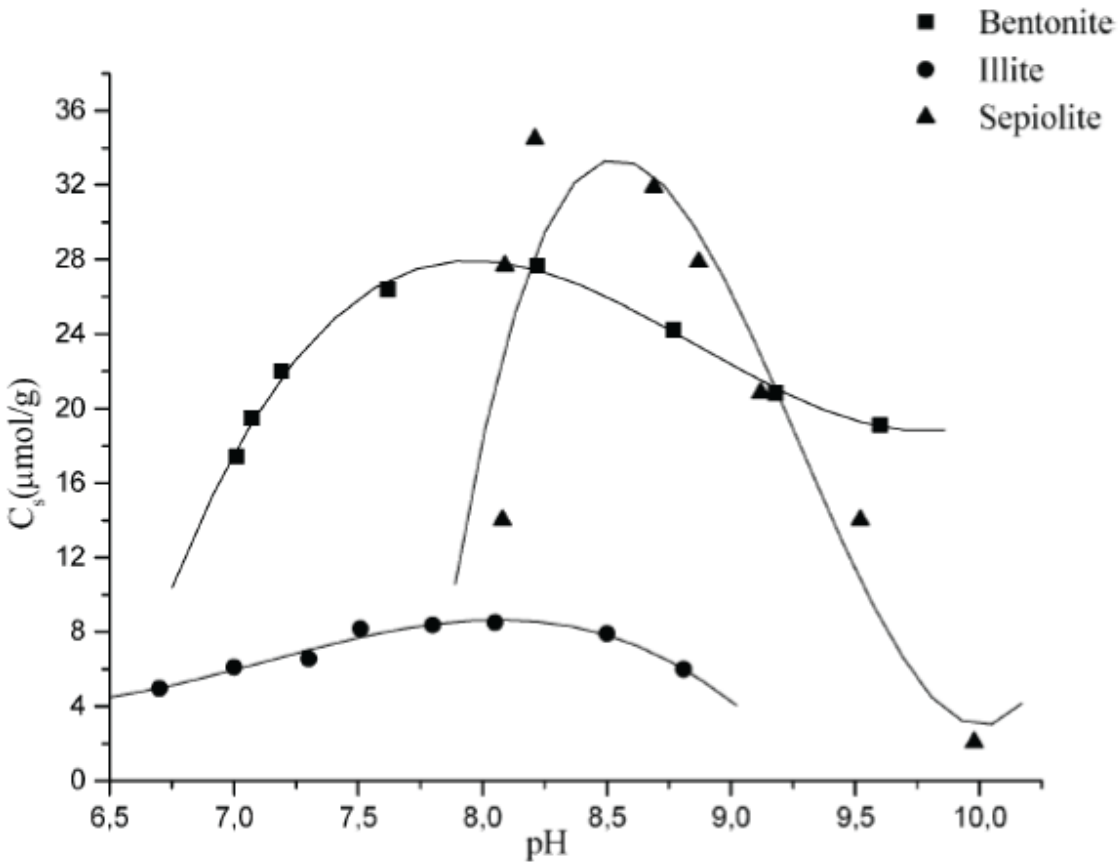

Figure 6: Karahan adsorption curve. Boron concentration for three clay mineral species over pH. All three species demonstrate the highest level of adsorption at alkaline pH between 7 and 9. (Figure *Karahan et al.*, 2006).

Clay minerals additionally most easily allow the sorption of boron in a borate form, $B(OH)_4^-$, rather than as boric acid, $B(OH)_3$, due to its strong charge affinity, further backing increased adsorption at higher pH [*Couch*, 1968; *Keren*, 1981]. Boron also adsorbs to clays more efficiently in a Ca-rich environment or when pH is adjusted by Ca-solutions [*Chen et al.*, 2009] than in the presence of sodium or potassium. This is likely due to calcium cations pulling more of the hydroxide anion from solution to prevent boron from bonding with hydroxide in solution and allowing it to adsorb to the surface of clays instead. This research replicates the methods of boron adsorption seen by previous research, but with Martian clay analogs [*Vaniman et al.*, 2014; *Bristow et al.*, 2015, 2018; *Treiman et al.*, 2014] in order to understand boron adsorption in a Martian environment as well as develop a method for creating a suite of standards to better quantify boron detection by LIBS.

Objectives

The objective of this research is to measure boron adsorption in a suite of Mars analog clays and to utilize these clays as LIBS standards. The adsorbed boron is measured and quantified via LIBS analysis in order to create references for detecting boron on Mars using the LIBS instruments aboard the *Curiosity* and future Mars 2020 rovers. Current boron detection using LIBS spectroscopy is limited by interference with other elemental peaks, notably iron [*Gasda et al.*, 2017]. Boron analysis will help to further understand Martian geochemistry and groundwater history. It is expected these experimental analyses of the Mars analogs saponite and nontronite will reflect previous test results with maximum boron adsorption around a pH of 8 to 9 due to their similar structure and behavior to the other smectite species used in previous research.

This study also hopes to better understand the range of boron adsorption across a range of clay compositions. Experiments have been previously run on a selection of smectite clays [*Couch,* 1968; *Karahan et al.*, 2006; *Keren,* 1981; *Keren et al*., 1994; *Okay et al.*, 1995; *Chen et al.*, 2009; *Goldberg et al.*, 1996; *Fleet,* 1965; *Harder,* 1970; *Perry,* 1972; *Yingkai et al.*, 2001] however saponite and nontronite were not incorporated into these tests, so this experimental analysis is the first to include these Fe- and Mg-smectites. Understanding how saponite and nontronite interact with boron is important for understanding how the clay minerals on Mars interact with boron and facilitated its deposition. For this study, the adsorption analysis of the Mars analog clays is being deferred for analysis on montmorillonite in order to reproduce, refine, and improve the methods used in previous experiments. This is to ensure the reproducibility of the methods and experiments used in this study. This study replaces the traditional colorimetric analysis for detecting boron with ICP-OES, as it provides a more accurate measurement for boron. Furthermore, investigating how pH conditions control boron adsorption to these clays may also provide insight into how much boron to expect within clay-rich rocks on Mars.

Analog studies and experimental analyses are integral for proper planetary research. The understanding of how geologic and aqueous processes occur on Mars or any other planetary body is done by comparing them to similar processes on Earth. The data collected on Mars from rovers, landers, and orbiters provides a lot of essential information on the planet, but it is still an incomplete dataset with many holes. These holes are filled by conducting analog studies and experimental analysis with similar conditions seen on Mars. This may include analysis of similar environments on earth or constructing an experiment in the lab under Mars conditions. This study uses terrestrial clays considered to be strong analogs to clays analyzed on Mars and then conducts

experimental analysis on these clays with aqueous and geochemical conditions relevant to the Martian setting of Gale crater.

A second goal of this study is to characterize a suite of Mars-analog clays to serve as standards for LIBS analysis. Clays were selected based on their similarity to clays encountered on Mars as well as clays that are expected to adsorb the largest quantity of boron. Montmorillonites experience strong adsorption of boron [*Karahan et al.*, 2006] and therefore make good references for how well boron adsorbs to a clay. Gale Crater contains abundant clay minerals, which are mostly Fe-rich saponite or potentially nontronite [*Vaniman et al.*, 2014]. These two smectite clays are trioctahedral and dioctahedral, respectively, and both may potentially allow for strong sorption of boron. Clays on Mars tend to be abundant in Fe and Mg, compared to the Al-rich clays seen on Earth, so for this reason talc is included in the experimental analysis to provide a strong Mg-endmember to complement the Fe-rich saponite and nontronite samples.

Methods

***Experimental Materials & Mineralogical Characterization*--** The clay samples in this study includes a griffithite, a saponite, a nontronite, two Ca-rich montmorillonite, a talc, and an unknown clay collected from the bottom of the Rio Tinto Boron Mine in California (**Table 1**). The griffithite sample (from Bronson Caves, Los Angeles, CA, USA), which is a ferrous saponite, comes from Allan Treiman (Lunar and Planetary Institute) and is considered to be a very strong analog to clays found on Mars [*Treiman et al.*, 2014]. The saponite sample, SaA1 purchased from Excalibur Minerals, is a monoclinic saponite from near Santa Barbara, Curacao in the Netherlands Antilles. The saponite sample has a general chemical makeup of $(Ca_{0.5},Na)_{0.3}(Mg,Fe)_3(Si,Al)_4O_{10}(OH)_2*4H_2O$. The nontronite sample, NAU-2 from Uley Mine in

southern Australia, is a nontronite standard from the Clay Mineral Society, has had extensive chemical analyses conducted on it (*Keeling*, 2000) and is additionally one of the LIBS standards used by ChemCam [*Vaniman et al.*, 2012]. Previous literature describes the sample as mostly nontronite with minor amounts of plagioclase feldspar and trace amounts of quartz, biotite, talc, and ilmenite [*Keeling*, 2000]. The nontronite is theorized to have formed from the fracturing and weathering of amphibolite with the breakdown of amphibole grains and light weathering of plagioclase into a solution rich in Fe and Si to eventually alter into nontronite. The montmorillonite sample, Ward's no 24, comes from Ward's Minerals and is a monoclinic smectite mineral from Wyoming, USA.

Table 1: Experiment grid of clay samples used for this study and the adsorption conditions.

Clay	**Sample ID**	**pH**	**B Fluid Concentration (ppm)**
Griffithite	Griff	6 to 11	200
Saponite	SaA1	6 to 11	200
Nontronite	Nau-2b	6 to 11	200
Rio Tinto	RTB1	6 to 11	200
Talc	BCS203a	6 to 11	200
Montmorillonite Ward's 46	MontA	6 to 11	200
Montmorillonite Ward's 24	MontB	6 to 11	200

The various clay samples are analyzed by X-Ray Diffraction (XRD). These experiments reveal the crystal structure and makeup of the clay samples prior to adsorption of boron. Further analysis after adsorption determines how the structure of the clay changes to accommodate the boron. This characterization of clay crystal structure assists in explaining how well boron adsorbs to each individual clay. Additionally, it assists in determining the position of the boron when it adsorbs to the clays. The XRD instrument used is the Rigaku SmartLab at the University of New Mexico (UNM) Department of Earth and Planetary Sciences (EPS) X-ray Diffraction Laboratory, equipped with a sealed tube copper target source. It is operated at 40 kV and 40 mA. The detector is the D/teX Ultra 1-dimensional detector that is used in conjunction with Ni-foil Cu Kβ filter. Copper is used for the source of the X-ray radiation because its Kα wavelength provides the best resolution and intensity for measuring diffraction peaks of most materials.

To prepare a clay sample for XRD analysis, first the sample must be powdered to a fine, evenly mixed grain size. Then 1 g of the powdered clay sample is added to a 30 mL vial and filled to the top with distilled water and shaken by hand for a few seconds. Then the vial is left to allow the entire solid volume to settle until the supernatant is clear. The supernatant is then decanted and this process is repeated one more time, in order to ensure any surface salts are removed. Then the vial is again filled with distilled water, but additionally with 0.05 grams of an anti-flocculent such as sodium pyrophosphate, in order to prevent the clay from clumping in solution. The vial is then shaken again and allowed to settle for 4 hours. After the 4 hours have passed, the top 5 cm of the solution is removed as this contains the clay fraction of the sample. This is pipetted into a plastic weighing boat and allowed to dry for a few days. To prepare the mount, 0.05 g of the dried sample is weighed out suspended in 2 mL of distilled water. With an eye dropper, this suspension is applied to a glass slide and surface tension should retain the entire volume. The slide is then left

to dry overnight and is then ready for analysis the next day. [*Poppe et al.*, 2001; *Moore & Reynolds*, 1997]. During analysis, JADE software is used to compare patterns with a standards library and it identifies the best fit.

The clay samples were also sent to a commercial analytical laboratory, ActLabs, for elemental analysis (**Table 2**). Inductively Coupled Plasma Mass Spectroscopy (ICP-MS) was run for calculating most of the bulk analysis for the major and minor elements. Prompt Gamma Neutron Activation Analysis (PGNAA) was run for the calculating the composition of boron within the samples. The clays that were sent to ActLabs included the unaltered Mars analog clays and terrestrial clays as well as the Rio Tinto clay and one of the montmorillonites that had been saturated with boron. The unaltered samples were analyzed to determine a baseline chemistry to determine if there was any structural boron in the samples and if so, how much. The Rio Tinto and boron-montmorillonite were analyzed to determine the amount of boron that had been introduced into the clays.

Additional analyses were performed on the Rio Tinto clay sample on the Scanning Electron Microscope (SEM) and the Electron Probe Micro-Analyzer (EPMA) at the UNM EPS Scanning Electron Microscope and Electron Microprobe Laboratory. We used a Tescan Vega 3 with IXRF EDS system for SEM and JEOL 8200 electron microprobe using Phi-Rho-Z correction on Probe for EPMA, a 3rd party software from Probe Software, Inc. The first step in this approach was to use the SEM in order to image the clay as well as attempting a semi-quantitative analysis of the sample to search for boron. First the sample, which was previously powdered for other experiments, is prepped for analysis by placing on a mount and coated in a gold-palladium coating to be analyzed in the SEM. Then the instrument parameters are set with an accelerating voltage of the beam at 15 kV in order to prevent any charging effects as well as not to overwhelm any

potential boron signature that could be present. The beam current is kept to about 9 pA. Several EDS scans are conducted at a couple locations in order to determine rough chemical composition of the clay sample. EDS analysis of low atomic number (Z) elements is either difficult or impossible due to the nature of x-rays and detection. Low Z elements emit low-energy x-rays, which are easily adsorbed by the sample and therefore make detection difficult. As boron is a low Z element (5), it is unlikely that EDS will be able to detect and quantify the amount of boron in the samples, given the low concentration.

The second step of the analysis is done under EPMA. To prep the Rio Tinto sample, the sample is mounted on a carbon stub in order to avoid interference with Al. Before the Rio Tinto sample is looked at, a sample of dravite is analyzed, which is a species of tourmaline with a high concentration of boron in it. It has the standard chemical formula of $Na(Mg_3)Al_6(Si_6O_{18})(BO_3)_3(OH)_3(OH)$ (Dravite, 2019). This is to help calibrate the EPMA for being able to detect boron. As boron is a low weight element and not as easily quantified by SEM or EPMA, it is necessary to ensure the instrument is recently calibrated with a known boron standard for a more accurate analysis. The dravite sample is run with an accelerating voltage of 15 kV and a beam current of 20 nA. A total of three analysis points were analyzed under quantitative analysis to calibrate the EPMA. After the probe is properly calibrated with the dravite sample, then began the analysis of the Rio Tinto sample. The accelerating voltage is kept at 15 kV, however the beam current is dropped to 10 nA in order to decrease the amount of charge running through the beam. The Rio Tinto sample is known to have much less boron than the dravite sample, due to the prior analysis via PGNAA, so the stronger current used in the dravite is not necessary for the Rio Tinto sample. A higher current is also used for the dravite to help provide a better count signal for calibration. Two different clay maps are generated of the sample at two different areas covering a

Table 2: ActLabs analysis of clay samples consisting of major, minor, & trace element analysis. Major/minor/trace elements by Li-tetraborate Fusion ICP-MS, PGNAA for B, peroxide Fusion ICP-OES for Li, C and S are measured by loss of ignition and IR of CO_2 and SO_2 gas

Table 2A: Major element analysis expressed as component oxide

	Analyte Symbol	Mass	SiO2	Al2O3	Fe2O3(T)	MnO	MgO	CaO	Na2O	K2O	TiO2	P2O5	LOI	Total
	Unit Symbol	g	%	%	%	%	%	%	%	%	%	%	%	%
	Detection Limit		0.01	0.01	0.01	0.001	0.01	0.01	0.01	0.01	0.001	0.01		0.01
	Analysis Method	PGNAA	FUS-ICP	FUS-ICP	FUS-ICP	FUS-ICP	FUS-ICP	FUS-ICP	FUS-ICP	FUS-ICP	FUS-ICP	FUS-ICP	GRAV	FUS-ICP
Talc 1a	JCRMR901	1.02	59.63	0.92	1.22	0.008	30.49	0.44	0.05	< 0.01	0.02	0.19	5.87	98.83
Talc 1b	JCRMR902	1.03	60.97	0.11	0.09	0.005	30.86	0.34	< 0.01	< 0.01	0.003	0.04	6.13	98.57
Talc 1c	JCRMR903	1.06	56.2	2.44	0.57	0.006	31.57	1	0.03	< 0.01	0.077	0.06	8.13	100.1
Talc 2	BCS203a	1.03	59.36	0.31	0.22	0.005	32.33	0.26	0.01	< 0.01	0.008	0.1	6.64	99.26
Talc 3a	DC60131	1.02	60.85	0.09	0.29	0.004	31.7	0.39	0.02	< 0.01	0.003	0.16	5.15	98.65
Talc 3b	DC60132	1.02	48.22	7.55	2.64	0.024	29.18	2.58	0.05	0.03	0.514	0.11	9.34	100.2
Rio Tinto	RTB1	1.08	51.32	9.24	3.48	0.123	11.65	4.85	3.05	3.31	0.492	0.05	12.33	99.89
Saponite	SaA1	1.07	45.99	12.76	11.1	0.155	10.42	10.25	0.77	0.04	0.826	0.06	8.3	100.7
Montmorllionite Ward's 46	WMB24b	1.03	59.69	18.88	3.9	0.019	2.1	1.16	2.21	0.55	0.145	0.06	11.09	99.8
Nontronite	Nau-2b	1.02	50.22	2.6	33.53	0.009	0.77	1.39	0.26	0.04	0.079	0.02	10.14	99.05
Montmorllionite Ward's 24	WMB24a	1.1	57.87	16.03	1.72	0.079	5.94	1.33	1.13	0.86	0.274	0.05	13.99	99.27

Table 2B: Minor and trace element analysis

	Analyte Symbol	B	C-Total	Total S	C-Organic (HCl leach)	Sc	Be	V	Ba	Sr	Y	Zr	Cr	Co
	Unit Symbol	ppm	%	%	%	ppm	ppm	ppm	ppm	ppm	ppm	ppm	ppm	ppm
	Detection Limit	2	0.01	0.01	0.02	1	1	5	2	2	1	2	20	1
	Analysis Method	PGNAA	CS	CS	IR	FUS-ICP	FUS-ICP	FUS-ICP	FUS-ICP	FUS-ICP	FUS-ICP	FUS-ICP	FUS-MS	FUS-MS
Talc 1a	JCRMR901	5	0.3	< 0.01	0	< 1	< 1	11	2	2	2	21	< 20	4
Talc 1b	JCRMR902	9	0.54	< 0.01	0	< 1	< 1	< 5	3	< 2	< 1	4	< 20	< 1
Talc 1c	JCRMR903	4	0.73	< 0.01	0	2	< 1	10	5	19	< 1	18	30	1
Talc 2	BCS203a	8	0.56	< 0.01	0	1	< 1	< 5	2	4	2	6	< 20	< 1
Talc 3a	DC60131	8	0.06	< 0.01	0	< 1	< 1	< 5	3	4	< 1	2	< 20	< 1
Talc 3b	DC60132	8	0.6	0.01	0	13	< 1	105	9	20	8	56	40	7
Rio Tinto	RTB1	967	1.47	0.02	0	8	2	117	235	531	13	32	< 20	7
Saponite	SaA1	7	0.08	< 0.01	0	40	< 1	241	15	48	14	36	630	48
Montmorllionite Ward's 46	WMB24b	61	0.33	0.28	0	6	2	6	234	239	43	186	< 20	1
Nontronite	Nau-2b	< 2	0.05	< 0.01	0	17	1	138	16	108	3	16	20	11
Montmorllionite Ward's 24	WMB24a	15	0.1	< 0.01	0	6	4	79	417	161	34	242	< 20	2

Table 2C: Trace element and rare earth element analysis

	Analyte Symbol	Ni	Cu	Zn	Ga	Ge	As	Rb	Nb	Mo	Ag	In	Sn	Sb
	Unit Symbol	ppm	ppm	ppm	ppm	ppm	ppm	ppm	ppm	ppm	ppm	ppm	ppm	ppm
	Detection Limit	20	10	30	1	1	5	2	1	2	0.5	0.2	1	0.5
	Analysis Method	FUS-MS	FUS-MS	FUS-MS	FUS-MS	FUS-MS	FUS-MS	FUS-MS	FUS-MS	FUS-MS	FUS-MS	FUS-MS	FUS-MS	FUS-MS
Talc 1a	JCRMR901	< 20	< 10	< 30	1	1	< 5	< 2	< 1	< 2	< 0.5	< 0.2	< 1	< 0.5
Talc 1b	JCRMR902	< 20	< 10	< 30	1	< 1	< 5	< 2	< 1	< 2	< 0.5	< 0.2	< 1	< 0.5
Talc 1c	JCRMR903	30	< 10	< 30	4	2	< 5	< 2	1	< 2	< 0.5	< 0.2	< 1	< 0.5
Talc 2	BCS203a	< 20	< 10	< 30	1	2	< 5	< 2	< 1	< 2	< 0.5	< 0.2	< 1	< 0.5
Talc 3a	DC60131	< 20	< 10	< 30	< 1	< 1	< 5	< 2	< 1	< 2	< 0.5	< 0.2	< 1	< 0.5
Talc 3b	DC60132	< 20	< 10	< 30	12	1	< 5	< 2	5	< 2	< 0.5	< 0.2	1	< 0.5
Rio Tinto	RTB1	< 20	20	80	15	4	15	199	13	17	< 0.5	< 0.2	2	16.7
Saponite	SaA1	220	110	90	12	1	< 5	< 2	3	< 2	< 0.5	< 0.2	< 1	1
Montmorllionite Ward's 46	WMB24b	< 20	< 10	70	27	< 1	11	14	29	4	0.8	< 0.2	9	1.4
Nontronite	Nau-2b	80	10	120	2	< 1	< 5	< 2	< 1	< 2	< 0.5	< 0.2	< 1	< 0.5
Montmorllionite Ward's 24	WMB24a	< 20	< 10	70	21	2	< 5	29	23	< 2	0.9	< 0.2	3	0.5

Table 2D: Rare earth element analysis

	Analyte Symbol	Cs	La	Ce	Pr	Nd	Sm	Eu	Gd	Tb	Dy	Ho	Er	Tm
	Unit Symbol	ppm	ppm	ppm	ppm	ppm	ppm	ppm	ppm	ppm	ppm	ppm	ppm	ppm
	Detection Limit	0.5	0.1	0.1	0.05	0.1	0.1	0.05	0.1	0.1	0.1	0.1	0.1	0.05
	Analysis Method	FUS-MS	FUS-MS	FUS-MS	FUS-MS	FUS-MS	FUS-MS	FUS-MS	FUS-MS	FUS-MS	FUS-MS	FUS-MS	FUS-MS	FUS-MS
Talc 1a	JCRMR901	0.5	1.5	3	0.35	1.5	0.3	0.06	0.4	< 0.1	0.3	< 0.1	0.2	< 0.05
Talc 1b	JCRMR902	< 0.5	0.1	0.3	< 0.05	0.2	< 0.1	< 0.05	< 0.1	< 0.1	< 0.1	< 0.1	< 0.1	< 0.05
Talc 1c	JCRMR903	< 0.5	0.8	1.8	0.23	0.9	0.2	< 0.05	0.2	< 0.1	0.2	< 0.1	< 0.1	< 0.05
Talc 2	BCS203a	< 0.5	0.4	1.4	0.22	1.1	0.3	< 0.05	0.3	< 0.1	0.3	< 0.1	0.1	< 0.05
Talc 3a	DC60131	< 0.5	< 0.1	0.3	< 0.05	0.2	< 0.1	< 0.05	< 0.1	< 0.1	< 0.1	< 0.1	< 0.1	< 0.05
Talc 3b	DC60132	< 0.5	3.3	8.2	1.01	4.1	0.9	0.19	1	0.2	1.4	0.3	1	0.14
Rio Tinto	RTB1	35	36.3	70	7.71	27.4	5.1	1.07	3.5	0.5	2.7	0.5	1.3	0.2
Saponite	SaA1	< 0.5	2.3	5.8	0.99	5.1	1.6	0.62	2.1	0.4	2.5	0.5	1.6	0.22
Montmorllionite Ward's 46	WMB24b	< 0.5	57.3	120	14.1	50.5	11.4	0.74	9.6	1.7	9.4	1.8	4.8	0.7
Nontronite	Nau-2b	< 0.5	1.8	4.3	0.63	2.8	0.7	0.16	0.7	0.1	0.7	0.2	0.4	0.06
Montmorllionite Ward's 24	WMB24a	1.3	46.8	115	11.3	39.7	7.4	0.98	5.9	1.1	6.4	1.3	4.1	0.61

Table 2E: Trace element and rare earth element analysis

	Analyte Symbol	Yb	Lu	Hf	Ta	W	Tl	Pb	Bi	Th	U	Li	Li2O
	Unit Symbol	ppm	ppm	ppm	ppm	ppm	ppm	ppm	ppm	ppm	ppm	%	%
	Detection Limit	0.1	0.01	0.2	0.1	1	0.1	5	0.4	0.1	0.1	0.01	0.01
	Analysis Method	FUS-MS	FUS-MS	FUS-MS	FUS-MS	FUS-MS	FUS-MS	FUS-MS	FUS-MS	FUS-MS	FUS-MS	FUS-Na2O2	FUS-Na2O2
Talc 1a	JCRMR901	0.2	0.03	0.5	< 0.1	< 1	< 0.1	< 5	< 0.4	2	0.7	< 0.01	< 0.01
Talc 1b	JCRMR902	< 0.1	< 0.01	< 0.2	< 0.1	< 1	< 0.1	< 5	< 0.4	0.1	0.2	< 0.01	< 0.01
Talc 1c	JCRMR903	< 0.1	0.01	0.5	0.1	< 1	< 0.1	< 5	< 0.4	3	0.9	< 0.01	< 0.01
Talc 2	BCS203a	< 0.1	0.01	< 0.2	< 0.1	< 1	< 0.1	< 5	< 0.4	0.3	1.9	< 0.01	< 0.01
Talc 3a	DC60131	< 0.1	< 0.01	< 0.2	< 0.1	< 1	< 0.1	< 5	< 0.4	< 0.1	1.7	< 0.01	< 0.01
Talc 3b	DC60132	1	0.16	1.7	0.6	< 1	< 0.1	< 5	< 0.4	11.9	3.8	< 0.01	< 0.01
Rio Tinto	RTB1	1.3	0.23	1.2	1.2	< 1	0.5	25	< 0.4	17.7	8.8	0.28	0.6
Saponite	SaA1	1.5	0.23	1	0.2	< 1	< 0.1	15	< 0.4	0.3	6	< 0.01	< 0.01
Montmorllionite Ward's 46	WMB24b	4.4	0.65	7.8	3.5	< 1	0.4	58	0.6	42.7	13.9	< 0.01	< 0.01
Nontronite	Nau-2b	0.4	0.07	0.2	< 0.1	1	< 0.1	15	< 0.4	0.2	0.1	< 0.01	< 0.01
Montmorllionite Ward's 24	WMB24a	4.4	0.68	7.9	1.7	3	0.1	43	0.4	25.9	3.7	0.01	0.03

thin area of the clay and a thicker region of the clay. For both maps, scans are taken that focus on imaging the overall backscatter, and concentration maps for boron, sodium, potassium, calcium, and iron.

The study then proceeds to take quantitative analysis of 13 single points scattered throughout the sample, some of which fall on the above measured maps. These 13 point measurements have quantitative analysis by calculating the wt% of SiO_2, Al_2O_3, K_2O, CaO, B_2O_3, FeOT, Na_2O, MgO, TiO_2 as well as H_2O. This involves the calibration of these components to other known standards first. Si, Al, Ti, and K are calibrated using a the JEOL standard for orthoclase. Ca and Mg are calibrated using the JEOL standard for diopside. FeOT are done using the JEOL hematite standard and Na is done with JEOL albite standard. B is found using the dravite standard from above and then H_2O is found by difference. As for the map scans, spectrometer 1 uses the TAPJ crystal and is dedicated to scanning for Al and Si. Spectrometer 2 uses the PETL crystal and is designated for the scanning Ca and K. Spectrometer 3 uses the LDE3H crystal and is left to just scan for B. Spectrometer 4 uses the LiFH crystal and was scanning for Fe. Lastly, spectrometer 5 also uses a TAPJ crystal and scans for Na and Mg. The thirteen points gives individual point analyses and are also averaged together to give a rough general sample concentration.

The study generates boron-enriched clay minerals in the lab that will be used to test their interactions with ribose (a related study at LANL also involved with this study) and their ability to allow biotic processes to begin (**Figure 7**). The relationship between boron adsorption and pH is studied in both Mars-like and common terrestrial clay minerals including montmorillonite, and talc, and analogs to Martian clays, such as saponite, nontronite, and griffithite [*Vaniman et al.*, 2014; *Treiman et al.*, 2014].

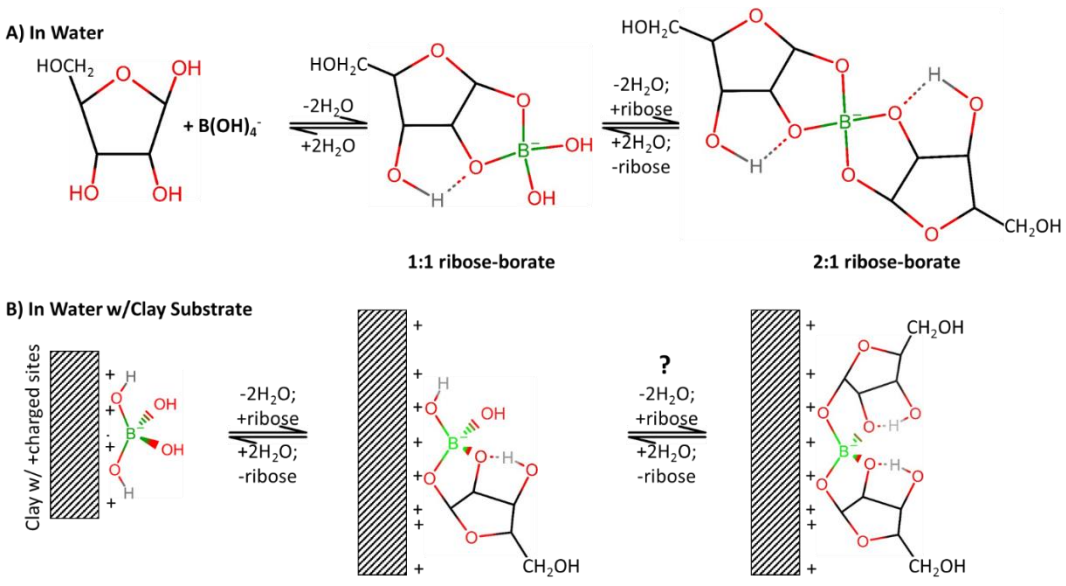

Figure 7: Borate-ribose complex in solution. Boron and ribose bond together, thereby stabilizing ribose from breaking down. The lower method shows how the boron-ribose complex is stabilized by being additionally bound to the surface of a clay, while the upper method, in just water, doesn't allow for boron-ribose complexes to remain stable and not break down (Figure *Gasda et al.*, 2019).

***Experimental Procedure*--**Using methods described in [*Karahan et al.*, 2006], (**Figure 6**) 37.5 mL of 200 ppm B solution made from boric acid (H_3BO_3) in a solution of 0.1 M $CaCl_2$ is added to 1.5 g of each clay sample in a plastic container and shaken for 10 hours to allow ample time for adsorption and then left to settle. pH is varied from 6 to 11 in increments of 1 for each clay type to determine the relationship between pH and boron adsorption. Samples are created and analyzed in quadruplicate. pH is adjusted by adding droplets (~0.05 mL) of either HCl or NaOH (at a concentration of 1 M). pH is measured both before and after adsorption period. Samples are centrifuged at 2600 rpm for 60 minutes, then shaken again, and centrifuged again for 2600 rpm for another 60 minutes. After allowing for the material to finish settling, the supernatant is removed. The supernatant is saved for Inductively Coupled Plasma - Optical Emission Spectroscopy (ICP-OES) analysis of the solution. The remaining boron-enriched clay is rinsed with a pH-similar fluid.

Samples are analyzed with ICP-OES in two forms, the clay with adsorbed boron and the supernatant removed from the samples. For analyzing the supernatant, boron adsorption is measured by the total loss of boron from the original solution. Some of the original boron solution is run alongside the supernatant to determine the amount of boron from control to after adsorption. Assuming the clay adsorbed boron in significant quantities, this is reflected by a decrease in boron detected in the supernatant in comparison to the original boron solution.

The clay samples that were exposed to the boron solution are then run through ICP-OES to analyze the amount of boron directly adsorbed by the clay. First the boron-exposed clays must be run through acid digestion using the procedure [*Martin et al.*, 1996], where the samples are ground into a fine powder and ~1 g of the powdered clay is exposed to acid. The clay samples are exposed to 2 mL of concentrated HNO_3 and 4 mL of concentrated HCl and left to sit and shake for 175 min. Afterwards 2% HNO_3 is added to bring the solutions up to 25 mL and left to sit overnight. Then the samples are ready for ICP-OES analysis using the methods defined in [*Martin et al.*, 1996].

The first experimental run consisted of analysis of just one of the montmorillonite samples in order to determine whether or not the clay would be capable of adsorbing boron. The boron was run at two separate concentrations, one at a lower value ~50 ppm B and a second higher concentration of over 500 ppm B. The second experimental set (**Table 3**) contained both species of montmorillonites, of which both were run at varying conditions. For pH tests, the pH was varied from 6 to 10 in increments of 1, while keeping the concentration steady at ~200 ppm B. For the concentration tests, the pH was held at 8, while boron concentration varied from 200, 100, 50, 25, and 10 ppm B. For the adsorption time tests, samples were held at pH 8 and a concentration of 200

ppm B, and were shaken for either 10 or 20 hours. The third experimental again contained both montmorillonites at ~200 ppm varied pH from 6 to 11, and shaken for 10 hours (**Table 4**).

Table 3: Experimental conditions for second round of adsorption analysis on two montmorillonites with varying adsorption concentrations. Samples analyzed on ICP-OES.

Sample	Sample Code Name	pH	B Concentration (ppm)	Sorption Time
Montmorillonite A	MonA6	6	200	10 Hours
Montmorillonite A	MonA7	7	200	10 Hours
Montmorillonite A	MonA8-200	8	200	10 Hours
Montmorillonite A	MonA9	9	200	10 Hours
Montmorillonite A	MonA10	10	200	10 Hours
Montmorillonite A	MonA6bl	6	Blank	10 Hours
Montmorillonite A	MonA7bl	7	Blank	10 Hours
Montmorillonite A	MonA8bl	8	Blank	10 Hours
Montmorillonite A	MonA9bl	9	Blank	10 Hours
Montmorillonite A	MonA10bl	10	Blank	10 Hours
Montmorillonite A	MonA8-100	8	100	10 Hours
Montmorillonite A	MonA8-50	8	50	10 Hours
Montmorillonite A	MonA8-25	8	25	10 Hours
Montmorillonite A	MonA8-10	8	10	10 Hours
Montmorillonite A	MonA8long	8	200	48 Hours
Montmorillonite B	MonB6	6	200	10 Hours
Montmorillonite B	MonB7	7	200	10 Hours
Montmorillonite B	MonB8-200	8	200	10 Hours
Montmorillonite B	MonB9	9	200	10 Hours
Montmorillonite B	MonB10	10	200	10 Hours
Montmorillonite B	MonB6bl	6	Blank	10 Hours
Montmorillonite B	MonB7bl	7	Blank	10 Hours
Montmorillonite B	MonB8bl	8	Blank	10 Hours
Montmorillonite B	MonB9bl	9	Blank	10 Hours
Montmorillonite B	MonB10bl	10	Blank	10 Hours
Montmorillonite B	MonB8-100	8	100	10 Hours
Montmorillonite B	MonB8-50	8	50	10 Hours
Montmorillonite B	MonB8-25	8	25	10 Hours
Montmorillonite B	MonB8-10	8	10	10 Hours
Montmorillonite B	MonB8long	8	200	48 Hours

Table 4: Experimental conditions for third round of adsorption analysis of two montmorillonite species.

Sample	Sample Code Name	pH	B Concentration (ppm)	Sorption Time	# Samples
Montmorillonite A	MN3-A6	6	200	10 Hours	4
Montmorillonite A	MN3-A7	7	200	10 Hours	4
Montmorillonite A	MN3-A8	8	200	10 Hours	4
Montmorillonite A	MN3-A8	9	200	10 Hours	4
Montmorillonite A	MN3-A10	10	200	10 Hours	4
Montmorillonite A	MN3-A11	11	200	10 Hours	4
Montmorillonite B	MN3-B6	6	200	10 Hours	4
Montmorillonite B	MN3-B7	7	200	10 Hours	4
Montmorillonite B	MN3-B8	8	200	10 Hours	4
Montmorillonite B	MN3-B9	9	200	10 Hours	4
Montmorillonite B	MN3-B10	10	200	10 Hours	4
Montmorillonite B	MN3-B11	11	200	10 Hours	4

The LIBS analysis is run independently at Los Alamos National Laboratory by the engineering unit for ChemCam, which is similar to the instrument onboard the MSL rover. The LIBS instrument fires an infrared laser focused to ~200-500 microns at selected rock targets up 7 m away from the rover [*Wiens et al.*, 2012; *Maurice et al.*, 2012]. Data collection usually consists of a raster of multiple observation points (spaced a few milliradians apart) and firing the LIBS laser 30 times at each shot point. The rover typically will analyze between 2 and 6 targets daily, providing ChemCam analyses from throughout the rover's traverse. The RMI instrument provides context imagery of the samples analyzed. The laser excites atoms within the target to produce a light-emitting plasma, with this signal being captured and analyzed by three spectrometers housed within ChemCam [*Wiens et al.*, 2012; *Maurice et al.*, 2012]. Based on the peak positions of the spectra, chemical abundances are calculated and can be converted into chemical weight percent in the form oxide wt% [*Clegg et al.*, 2017]. LIBS is capable of detecting all the elements and oxides can be calculated from the spectra. Boron is detectable by LIBS analysis, however the key

distinguishable boron peaks overlap some of the major iron peaks, so boron detection becomes difficult when iron is abundant in the sample. LIBS is a viable detection method as it provides quick, precise, and remote measurements in the form of point analyses. While not as accurate as mass spectroscopy, measuring with LIBS will allow for direct comparison with rover analyses.

Geochemical Modeling

Geochemical modeling consisted of the analysis of water samples from saline lakes including Mono Lake, Searles Lake, and Lonar Crater lake which have been used as Mars analog solutions in other studies [*Pawar*, 2010; *Smith*, 1979; *Domagalski et al.*, 1989] and groundwater elevated in boron from Bangladesh [*Halim et al.,* 2010] (**Table 5**). The focus of this modeling was to determine speciation of borate and to understand the effects various ions in solution have on borate speciation. Geochemist's Workbench was used for geochemical modeling on this study. Geochemist's Workbench (GWB) uses datasets of thermodynamic equilibrium constants to calculate chemical equilibria. GWB is used in this study to map stability diagrams, examine speciation of boron, and track reaction process in conditions simulating the experiments [*Bethke*, 2011]. The goal of this study is to generate the speciation diagrams given the water composition of the selected literature waters as well as some the lab experiments. In addition to speciation diagrams, some analysis consisted of comparing the ion activities of boron to other major ions to determine how they affect borate in solution.

Table 5: Water samples from groundwater wells, several alkaline lakes, and this study's experimental analysis used for geochemical modeling for predictive analysis of borate aqueous geochemistry.

Sample	Description	Source	pH	Temp (C)	HCO3 (mg/L)	Cl (mg/L)	NO3 (mg/L)	SO4 (mg/L)	Br (mg/L)	Na (mg/L)	K (mg/L)	Mg (mg/L)	Ca (mg/L)	Ba (µg/L)	Sr (µg/L)	Si (mg/L)	Fe (mg/L)	As (µg/L)	Mn (µg/L)	B (mg/L)	Dominant B Species	% B dominant phase
1	Bangladesh Groundwater Low B 1	Halim	7.3	26.1	202.07	263.56	0.46	2.10	1.27	73.26	3.41	39.38	89.28	200.6	488.60	21.00	0.44	1.2	44.5	0.234	N/A	N/A
2	Bangladesh Groundwater Low B 2	Halim	7.0	25.0	169.89	599.35	15.30	0.96	3.47	336.79	8.63	37.00	41.19	55.8	455.30	16.56	0.66	32.8	81.7	0.320	N/A	N/A
3	Bangladesh Groundwater High B 1	Halim	7.9	27.2	216.86	458.32	3.67	0.18	1.36	339.86	5.88	4.71	11.08	52.8	129.10	11.07	0.34	4.9	27.3	0.797	N/A	N/A
4	Bangladesh Groundwater High B 2	Halim	7.3	28.3	155.23	941.84	3.63	0.09	3.74	501.18	24.80	42.59	91.92	213.4	718.00	16.37	0.55	0.5	26.3	0.863	N/A	N/A
5	Mono Lake	Domagalski	9.65	25.0	0	11210	0	5880	0	35140	1890	43.7	5.8	0.0	0.00	0	0	0.0	0.0	0	N/A	N/A
6	Searles Lake Brine	Smith	9.9	25.0	0	98200	0	40800	449	111000	17700	0	0	0.0	0.00	33	0	98000.0	0.0	4039	N/A	N/A
7	Lonar Pre-Monsoon	Pawar	10.5	27.0	0	4126	4.2	21.75	0	7599.81	0	101.24	57.18	0.0	0.0	0.0	0.0	0.0	0.0	0	N/A	N/A
8	Lonar Post-Monsoon	Pawar	10.3	28.0	0	3265	2.4	21.18	0	5967.98	0	74.66	46.35	0.0	0.0	0.0	0.0	0.0	0.0	0	N/A	N/A
9	Lab 0 ppm B	N/A	8	25	0	70906	0	0	0	0	0	0	40078	0.0	0.0	0.0	0.0	0.0	0.0	0	N/A	N/A
10	Lab 10 ppm B	N/A	8	25	0	70906	0	0	0	0	0	0	40078	0.0	0.0	0.0	0.0	0.0	0.0	10	CaB(OH)4+	50.70%
11	Lab 25 ppm B	N/A	8	25	0	70906	0	0	0	0	0	0	40078	0.0	0.0	0.0	0.0	0.0	0.0	25	B(OH)3	62.30%
12	Lab 50 ppm B	N/A	8	25	0	70906	0	0	0	0	0	0	40078	0.0	0.0	0.0	0.0	0.0	0.0	50	B(OH)3	54.1
13	Lab 100 ppm B	N/A	8	25	0	70906	0	0	0	0	0	0	40078	0.0	0.0	0.0	0.0	0.0	0.0	100	CaB(OH)4+	55.9
14	Lab 200 ppm B	N/A	8	25	0	70906	0	0	0	0	0	0	40078	0.0	0.0	0.0	0.0	0.0	0.0	200	CaB(OH)4+	58.3
15	Lab 500 ppm B	N/A	8	25	0	70906	0	0	0	0	0	0	40078	0.0	0.0	0.0	0.0	0.0	0.0	500	B(OH)3	53.3
16	Lab 200 ppm B pH 6	N/A	6	25	0	70906	0	0	0	0	0	0	40078	0.0	0.0	0.0	0.0	0.0	0.0	200	B(OH)3	68.9
17	Lab 200 ppm B pH 7	N/A	7	25	0	70906	0	0	0	0	0	0	40078	0.0	0.0	0.0	0.0	0.0	0.0	200	B(OH)3	47.5
18	Lab 200 ppm B pH 9	N/A	9	25	0	70906	0	0	0	0	0	0	40078	0.0	0.0	0.0	0.0	0.0	0.0	200	CaB(OH)4+	73.8
19	Lab 200 ppm B pH 10	N/A	10	25	0	70906	0	0	0	0	0	0	40078	0.0	0.0	0.0	0.0	0.0	0.0	200	CaB(OH)4+	80
20	Lab 0.5 M CaCl2	N/A	8	25	0	35453	0	0	0	0	0	0	20039	0.0	0.0	0.0	0.0	0.0	0.0	200	CaB(OH)4+	51.6
21	Lab 0.25 M CaCl2	N/A	8	25	0	17727	0	0	0	0	0	0	10019.5	0.0	0.0	0.0	0.0	0.0	0.0	200	B(OH)3	53.1
22	Lab 0.1 M CaCl2	N/A	8	25	0	7091	0	0	0	0	0	0	4007.8	0.0	0.0	0.0	0.0	0.0	0.0	200	B(OH)3	67.7

Results

Mineralogy

XRD analysis was run on several of the clay samples prior to adsorption experiments in order to gain an understanding of their mineralogic makeup to serve as a baseline before borate and later organic reaction experiments. The samples run through XRD were the nontronite, saponite, griffithite, the unknown clay retrieved from the Rio Tinto borax mine, as well as two montmorillonites. These particular samples were run through XRD in order to compare the structure of the clays before and after adsorption experiments. The distinctive 001 and 060 peaks common of phyllosilicate clays were seen strongly in all of the clay samples (**Figures 8 & 9**). Several of the clays were also revealed not to be completely pure samples, which may make them suitable for adsorption experiments as their application for Mars data can be compared to Mars clays, which are also not pure. XRD analysis of montmorillonite samples revealed them to be relatively pure samples with minor secondary minerals including quartz and feldspar. The analysis of the nontronite revealed that it was very pure and almost entirely nontronite (**Figure 10**). The griffithite and saponite (**Figures 11 & 12**), while they were indicated to be mostly clay mineral in makeup, were observed including minor amounts of plagioclase feldspar and pyroxene. The Rio Tinto sample (**Figure 13**) was largely an unknown clay mineral which could not be matched with the standards in the JADE mineral library, but did contain minor amounts of plagioclase and calcite in it as well. Given the detection of boron in this sample by ICP-MS and LIBS analysis, it is possible this sample contains a borate mineral phase, but it is below the detection limit for XRD identification. Lastly, the two montmorillonites displayed typical montmorillonite XRD patterns, but there were differences between the two indicating variance between similar species of clays

(**Figure 14**). Further characterization is required to positively identify the clay mineral present in the sample, but that is beyond the scope of this study.

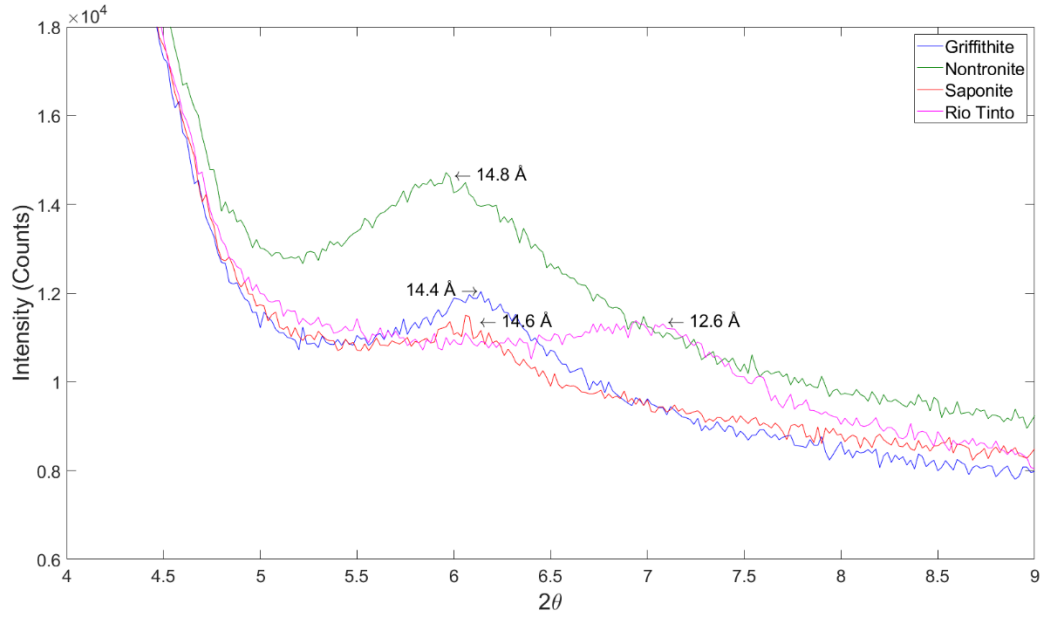

Figure 8: XRD clay samples 001 peak. XRD analysis of all four clay samples displaying the distinctive 001 peak indicative of clay minerals.

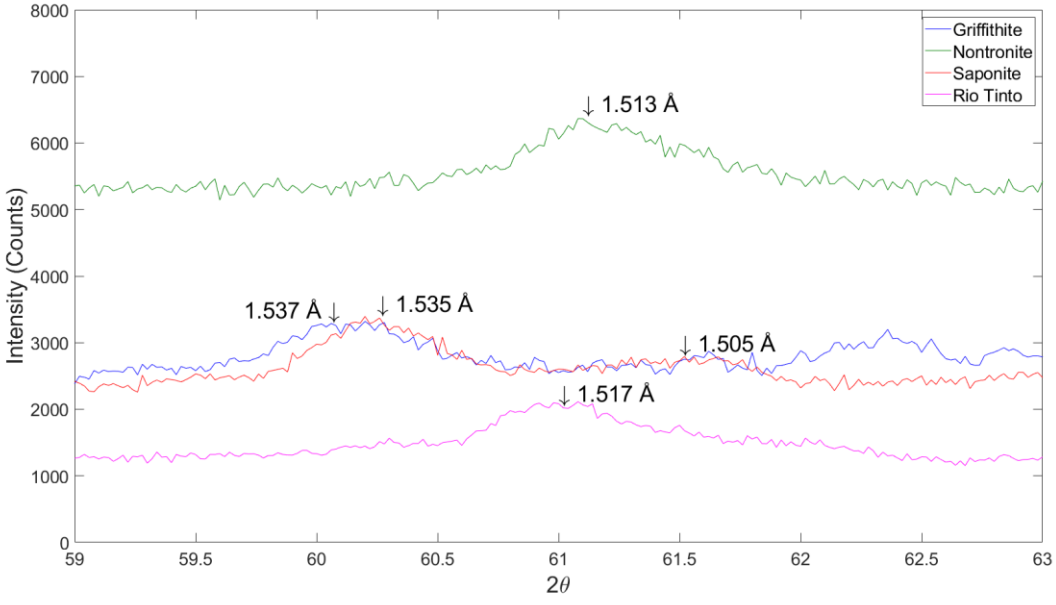

Figure 9: XRD clay samples 060 peak. XRD analysis of all four clay samples displaying the distinctive 060 peak indicative of clay minerals.

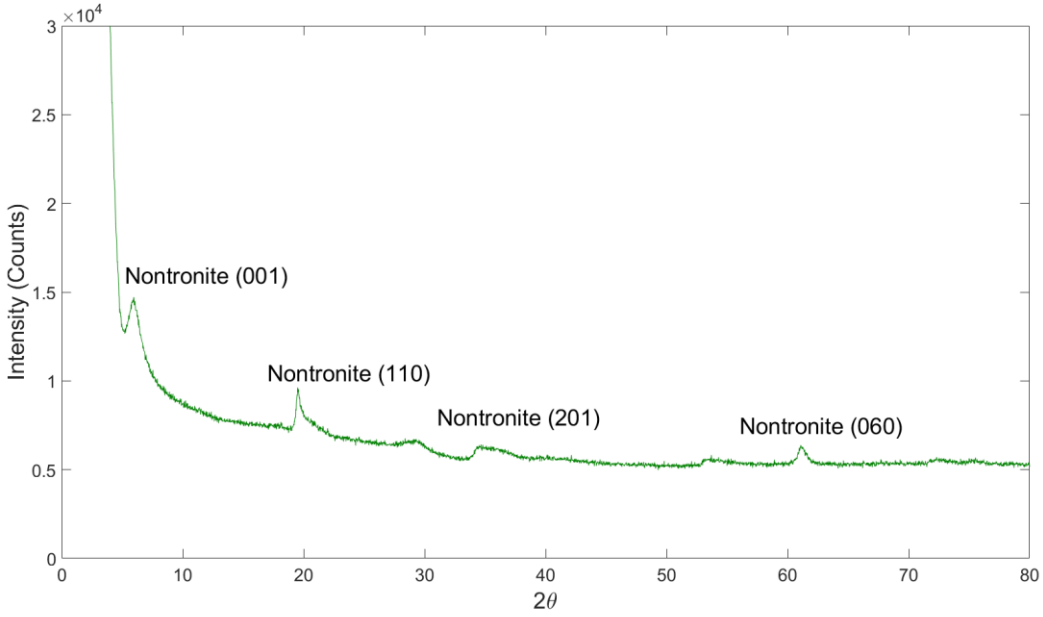

Figure 10: XRD nontronite pattern. Results from XRD analysis of nontronite clay displaying a typical nontronite signal.

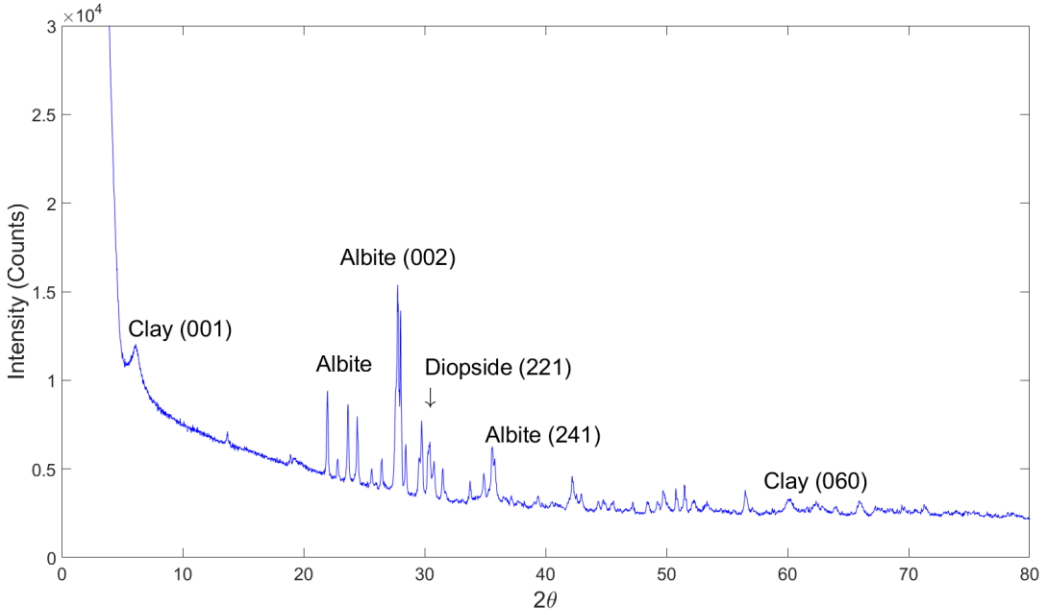

Figure 11: XRD griffithite pattern. Results from XRD analysis of griffithite clay displaying a clay mineral signal, with additional plagioclase and pyroxene peaks.

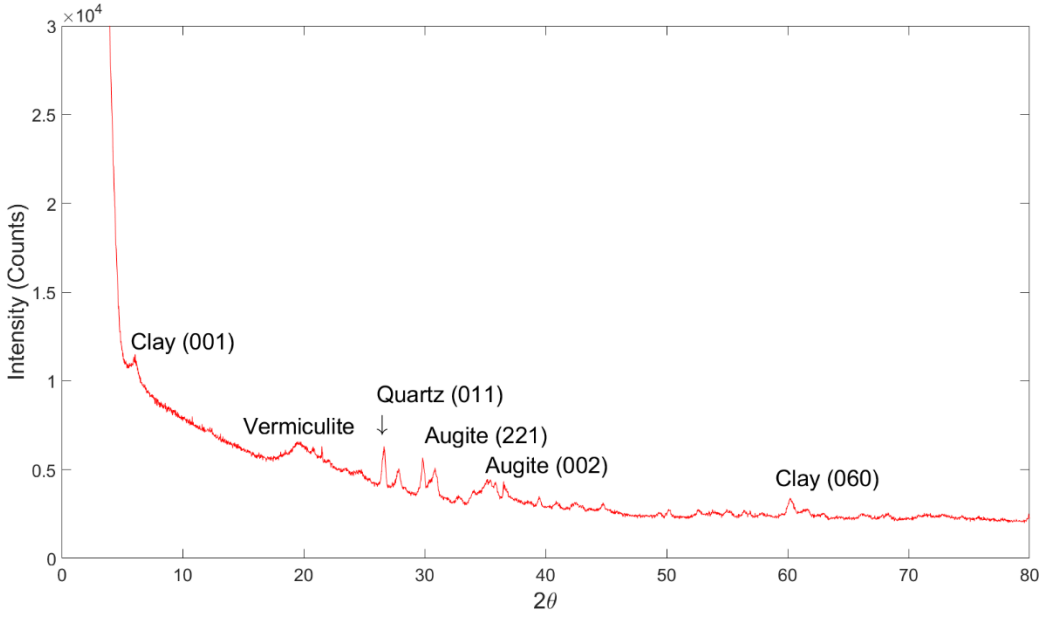

Figure 12: XRD saponite pattern. Results from XRD analysis of saponite clay displaying a clay mineral signal, with additional plagioclase and pyroxene peaks.

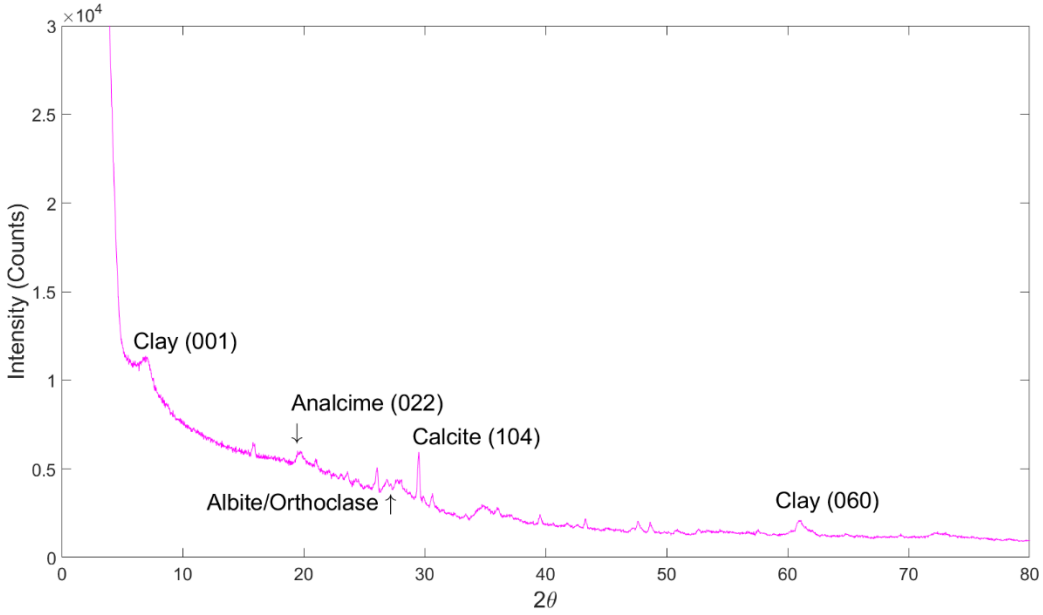

Figure 13: Results from XRD analysis of Rio Tinto clay displaying a clay mineral signal, with additional plagioclase and calcite peaks.

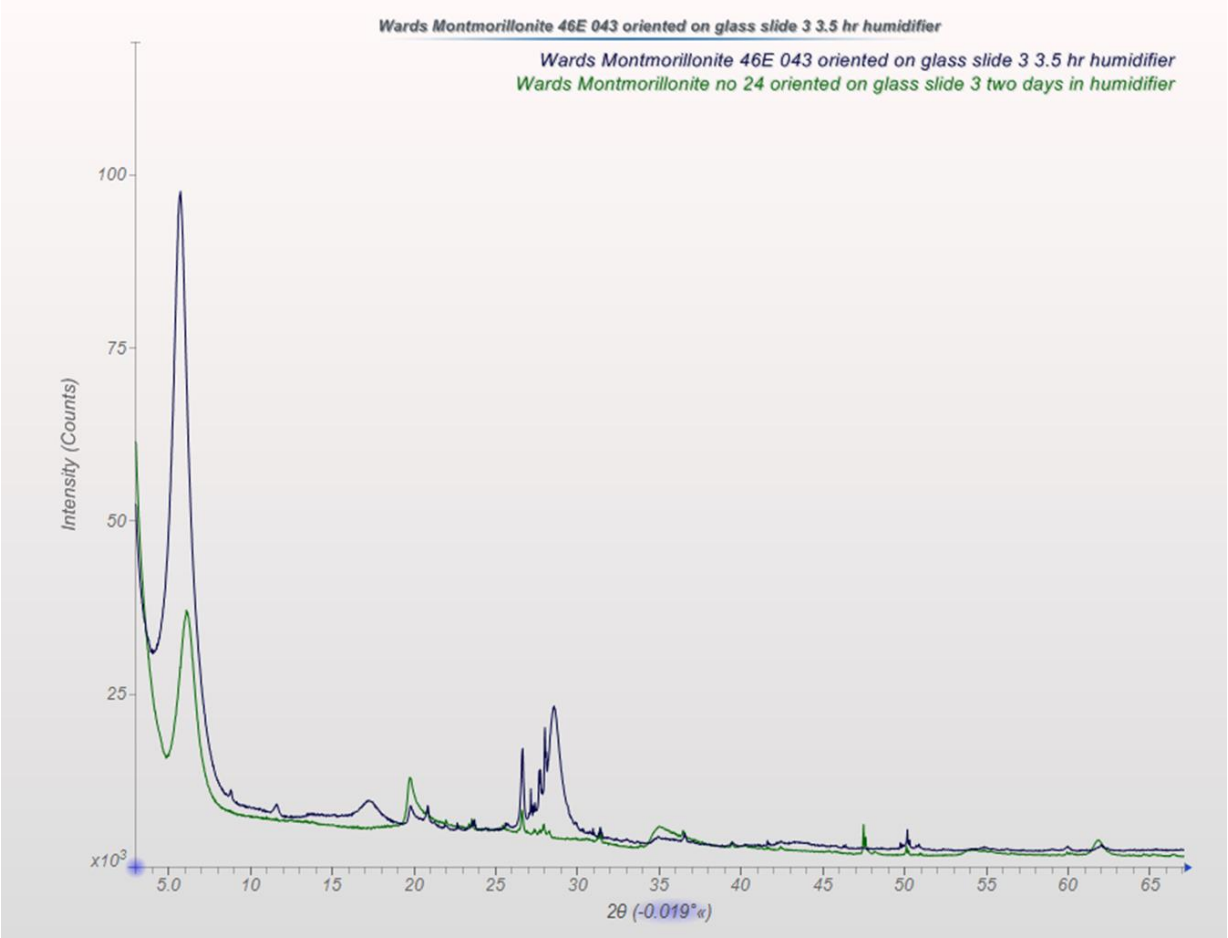

Figure 14: Results from XRD analysis of two montmorillonite clays. “Montmorillonite no 24” is Montmorillonite A in these experiments, while “Montmorillonite 46E 043” represents Montmorillonite B.

Adsorption Experimental Results

The first experimental test used a montmorillonite sample, Ward’s 46E 043, to attempt to adsorb boron to the clay and detect it using ICP-OES. For this test, two borate solutions were created, one at a low concentration at ~50 ppm and one at high concentration at >500 ppm. Initial analysis using ICP-OES was run by detecting the amount of boron from the removed supernatants in relation to the original borate solutions (**Figure 15**). The lower concentration samples detected boron in the range of ~69 ppm in both the borate solution and the boron-enriched samples. There was no change detected between the original borate solution and the subsequent supernatants because this concentration of boron is close to the detection limits of the ICP-OES, making this

measurement difficult. However, at the high concentration, there was a noticeable change detected between the original borate solution (753 ppm B) and the following supernatant (647 ppm B). At this concentration there is a clear loss of boron from solution, which can be likely attributed to sorption of the boron by the clay sample. Furthermore, while the low concentration boron samples were not able to reflect a loss of boron from solution, all of the samples of both concentrations did still fall on the calibration curve between the calibration targets and the standard targets demonstrating the high level of accuracy of detecting boron by ICP-OES.

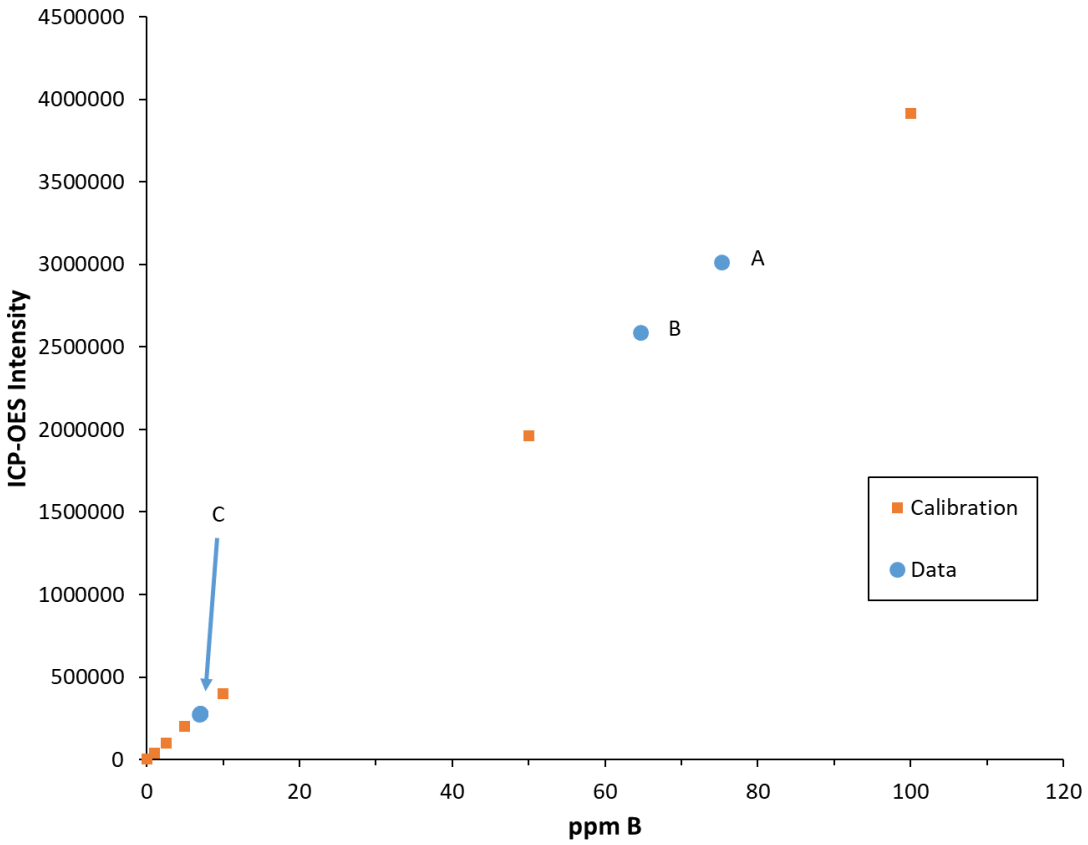

Figure 15: ICP-OES first round adsorption experiment results. Results from first preliminary test displaying that any adsorption at low concentration was not detectable while at high concentration, a significant amount of boron was lost from solution and assumed sorbed to the clay. Point A represents the starting borate solution of high concentration (diluted 1:10). Point B represents the boron concentration of the supernatant removed from the clay sample after adsorption (diluted 1:10). Point C represents the starting borate solution of low concentration (diluted 1:10) and 4 supernatants (diluted 1:10) removed from clay samples.

The second and third tests were a series of experiments and run on the two montmorillonite clays (A & B) (**Table 6-8**). Montmorillonite A is another Ward's sample (Ward's 24) and Montmorillonite B is the Ward's 46E 043 used in the previous test (**Figure 16 & 17**). For this round of experiments the samples were reacted with varying concentrations of borate-carrying fluid, varied adsorption times, and different pH conditions. The concentration was tested at 200, 100, 50, 25, and 10 ppm B in the second set and only 200 ppm for the third. For the test with varying concentration, the samples were tested at pH 8. The results of this experiment displayed that the amount of boron that is adsorbed by the clay is increases with an increase in initial boron concentration (**Figure 18**). While montmorillonite B increased linearly, montmorillonite A increased non-linearly and saw a steep increase in boron adsorption at higher fluid concentration. Calculating a linear or Langmuir sorption behavior, a partition coefficient (K_d) can be calculated using the formula

$$K_d = \frac{V_w(C_0 - C_i)}{M_{sed} * C_i} [EPA],$$

where V_w represents the volume in solution, C_0 represents the known concentration of an ion in solution, C_i represents the concentration left in the supernatant, and M_{sed} represents the mass of the solid. Freundlich fitting can calculated by linearizing the equation

$$\frac{x}{m} = KC^n \rightarrow \log\frac{x}{m} = \log K + n * \log C$$

where *x/m* is the adsorbed concentration, *K* is the calculated partition coefficient, *n* is the adsorption intensity, and *C or C_i* is the fluid concentration [*Ayawei et al.*, 2017]. Both clays were analyzed using Langmuir and Freundlich fitting (**Table 9, Figures 19-20**) and from these fits were able to construct adsorption isotherms (**Figures 21-22**). For Montmorillonite A, the Freundlich fit

Table 6: Results from the second round of adsorption analysis

Sample	Fluid Concentration (mg/L)	Conc (Karahan) (µmol/g)
MonB6	209	19.9
MonB7	209	181
MonB8-200	209	40.4
MonB9	209	111
MonB10	209	173
MonB8long	209	52.5
MonB6bl	0.00	<0.100
MonB7bl	0.00	<0.100
MonB8bl	0.00	<0.100
MonB9bl	0.00	<0.100
MonB10bl	0.00	0.025
MonB8-100	81.9	15.8
MonB8-50	54.6	10.5
MonB8-25	18.2	2.21
MonB8-10	10.0	2.95
MonA6	209	29.0
MonA7	209	39.9
MonA8-200	209	63.5
MonA9	209	116
MonA10	209	185
MonA8long	209	43.3
MonA6bl	0.00	<0.100
MonA7bl	0.00	<0.100
MonA8bl	0.00	<0.100
MonA9bl	0.00	<0.100
MonA10bl	0.00	<0.100
MonA8-100	81.9	17.6
MonA8-50	54.6	8.68
MonA8-25	18.2	3.78
MonA8-10	10.0	1.76

Table 7: Results from third round of adsorption analysis for Montmorillonite A

Sample ID	Base Solution (mL)	$CaCl_2$ (M)	Reported Concentration (mg/L)	Volume (L)	Mass B on Clay (g)	µmol B/ g clay	mg B/kg clay	pH Before	pH After
MN3-A6a	193	0.1	189	0.0375	1.50	10.2	110	6.05	6.33
MN3-A6b	193	0.1	121	0.0375	1.50	166	1800	5.94	6.45
MN3-A6c	193	0.1	116	0.0375	1.51	177	1920	6.14	6.49
MN3-A6d	193	0.1	171	0.0375	1.50	51.8	560	6.03	6.46
MN3-A7a	193	0.1	168	0.0375	1.50	59.6	645	6.98	6.77
MN3-A7b	193	0.1	172	0.0375	1.51	49.9	540	7.01	6.76
MN3-A7c	193	0.1	171	0.0375	1.51	50.4	545	6.99	6.73
MN3-A7d	193	0.1	172	0.0375	1.50	48.7	527	7.00	6.78
MN3-A8a	193	0.1	144	0.0375	1.51	113	1220	7.97	7.68
MN3-A8b	193	0.1	149	0.0375	1.51	103	1110	8.00	7.71
MN3-A8c	193	0.1	149	0.0375	1.50	102	1100	8.02	7.71
MN3-A8d	193	0.1	149	0.0375	1.50	103	1120	7.99	7.71
MN3-A9a	193	0.1	105	0.0375	1.50	205	2220	8.99	8.92
MN3-A9b	193	0.1	103	0.0375	1.50	208	2250	8.99	8.82
MN3-A9c	193	0.1	166	0.0375	1.50	63.6	687	9.03	8.84
MN3-A9d	193	0.1	160	0.0375	1.50	76.0	821	9.01	8.87
MN3-A10a	193	0.1	157	0.0375	1.50	84.8	917	10.3	9.29
MN3-A10b	193	0.1	161	0.0375	1.51	74.2	802	10.1	9.29
MN3-A10c	193	0.1	160	0.0375	1.50	77.0	832	10.1	9.25
MN3-A10d	193	0.1	168	0.0375	1.51	57.7	623	9.94	9.25
MN3-A11a	193	0.1	197	0.0375	1.50	<0.001	<0.001	11.0	9.43
MN3-A11b	193	0.1	182	0.0375	1.50	26.4	285	11.0	9.36
MN3-A11c	193	0.1	157	0.0375	1.50	84.8	917	11.1	9.37
MN3-A11d	193	0.1	159	0.0375	1.51	79.1	855	11.0	9.35

Table 8: Results from third round of adsorption analysis for Montmorillonite B

Sample ID	Base Solution (mL)	$CaCl_2$ (M)	Reported Concentration (mg/L)	Volume (L)	Mass B on Clay (g)	µmol B/ g clay	mg B/kg clay	pH Before	pH After
MN3-B6a	191	0.1	165	0.0375	1.51	61.7	667	5.91	7.30
MN3-B6b	191	0.1	169	0.0375	1.51	52.2	564	6.10	7.18
MN3-B6c	191	0.1	166	0.0375	1.50	57.6	623	6.15	7.12
MN3-B6d	191	0.1	174	0.0375	1.51	40.8	441	6.12	7.09
MN3-B7a	191	0.1	165	0.0375	1.50	60.5	654	7.03	7.14
MN3-B7b	191	0.1	166	0.0375	1.50	59.6	644	7.04	7.15
MN3-B7c	191	0.1	165	0.0375	1.50	60.0	648	7.01	7.15
MN3-B7d	191	0.1	176	0.0376	1.50	34.5	373	7.01	7.14
MN3-B8a	191	0.1	166	0.0375	1.50	59.4	642	8.01	7.64
MN3-B8b	191	0.1	145	0.0375	1.50	108	1160	8.00	7.64
MN3-B8c	191	0.1	145	0.0375	1.51	107	1160	8.01	7.61
MN3-B8d	191	0.1	150	0.0375	1.51	95.8	1040	8.00	7.66
MN3-B9a	191	0.1	108	0.0375	1.50	192	2080	8.99	8.39
MN3-B9b	191	0.1	108	0.0375	1.51	192	2080	9.01	8.40
MN3-B9c	191	0.1	118	0.0375	1.50	170	1840	9.02	8.43
MN3-B9d	191	0.1	121	0.0375	1.51	162	1750	9.02	8.45
MN3-B10a	191	0.1	91.3	0.0375	1.51	230	2480	10.0	8.80
MN3-B10b	191	0.1	90.9	0.0375	1.50	232	2510	10.2	8.84
MN3-B10c	191	0.1	93.1	0.0375	1.51	226	2440	10.0	8.84
MN3-B10d	191	0.1	91.6	0.0375	1.50	230	2490	10.0	8.82
MN3-B11a	191	0.1	84.6	0.0375	1.51	246	2660	11.0	8.98
MN3-B11b	191	0.1	82.2	0.0375	1.50	252	2720	11.0	8.99
MN3-B11c	191	0.1	80.9	0.0375	1.50	255	2760	11.1	9.01
MN3-B11d	191	0.1	79.2	0.0375	1.50	259	2800	11.0	9.02

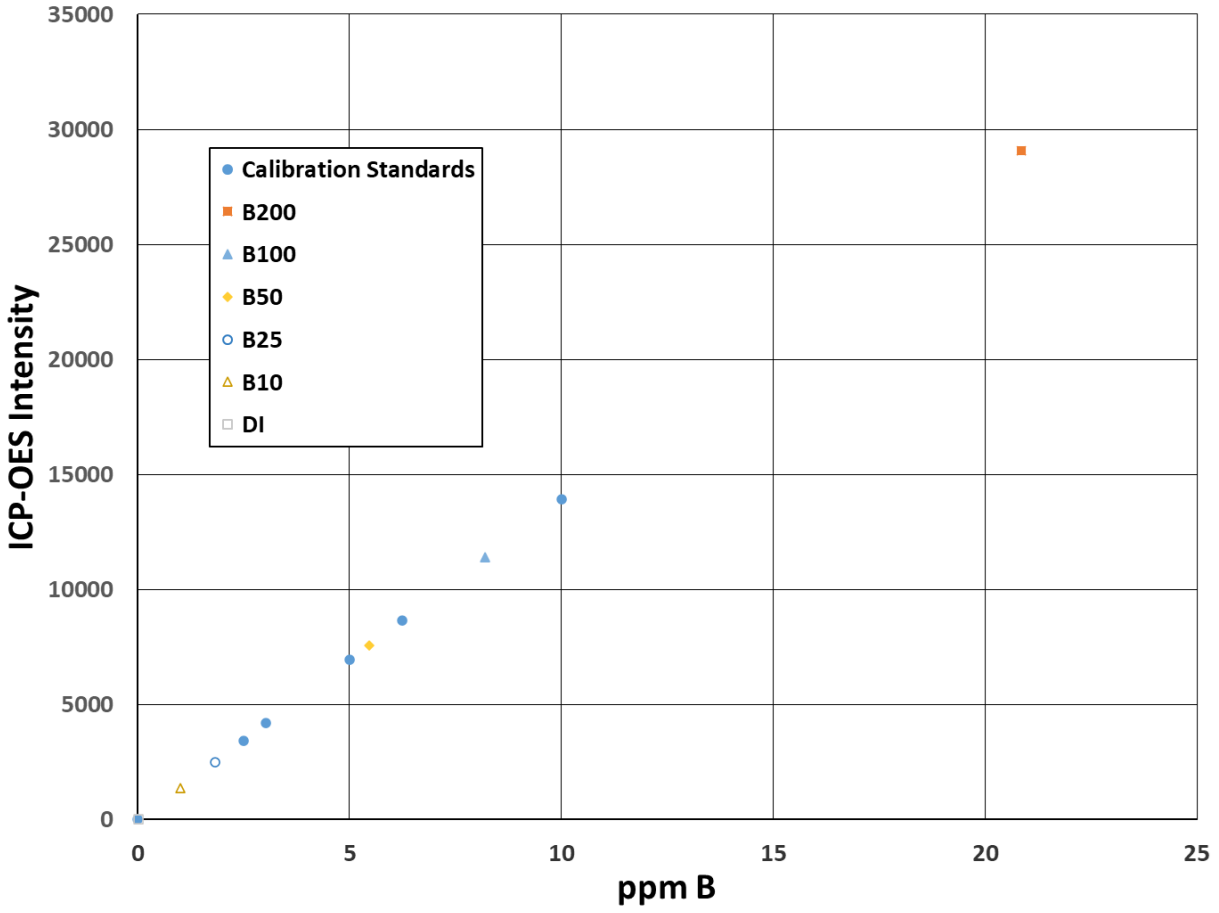

Figure 16: ICP-OES second round standards and starter solution. Results from second preliminary test displaying calibration curve with calibration standards and boron-carrying fluids

had a slightly better correlation with an R^2 of 0.9778 compared to the linear fit of 0.9735. Montmorillonite B, which had the high concentration B point (Freundlich was calculated with and without this point, while linear was calculated without) saw better correlation with the linear fit with an R^2 of 0.9962, while the Freundlich fits, with and without the high B point, were 0.9373 and 0.9202 respectively. Adsorption time was tested at the 200 ppm B and pH 8 level by adjusting sorption times of both 10 and 20 hours. Despite the 20 hours sample allowing more

time for adsorption of more boron, the amount of boron lost from solution between the two samples was negligible (**Figure 23**).

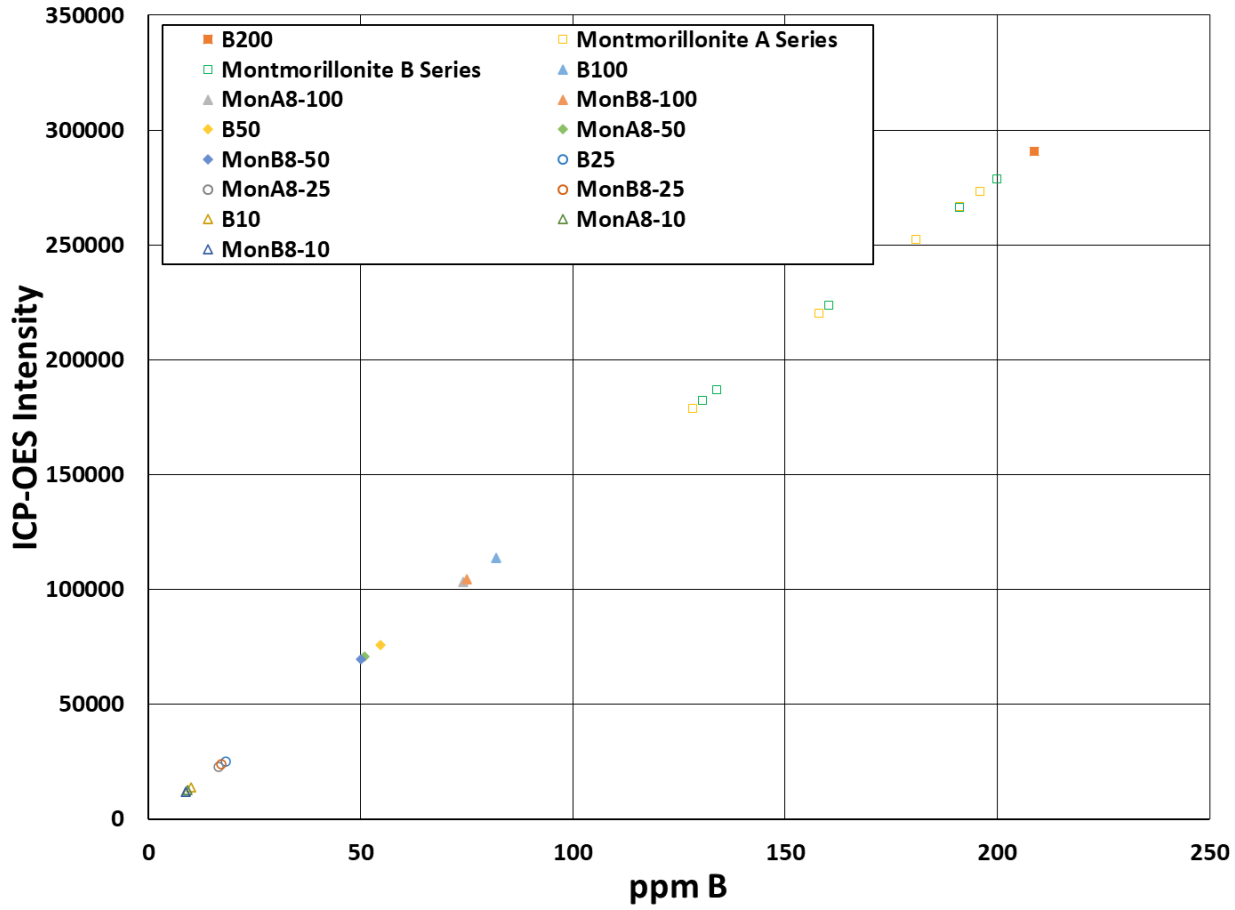

Figure 17: ICP-OES second round adsorption analysis results. Results from second preliminary test displaying how boron was lost from solution at different concentration ranges, indicating some degree of adsorption of boron to the clays.

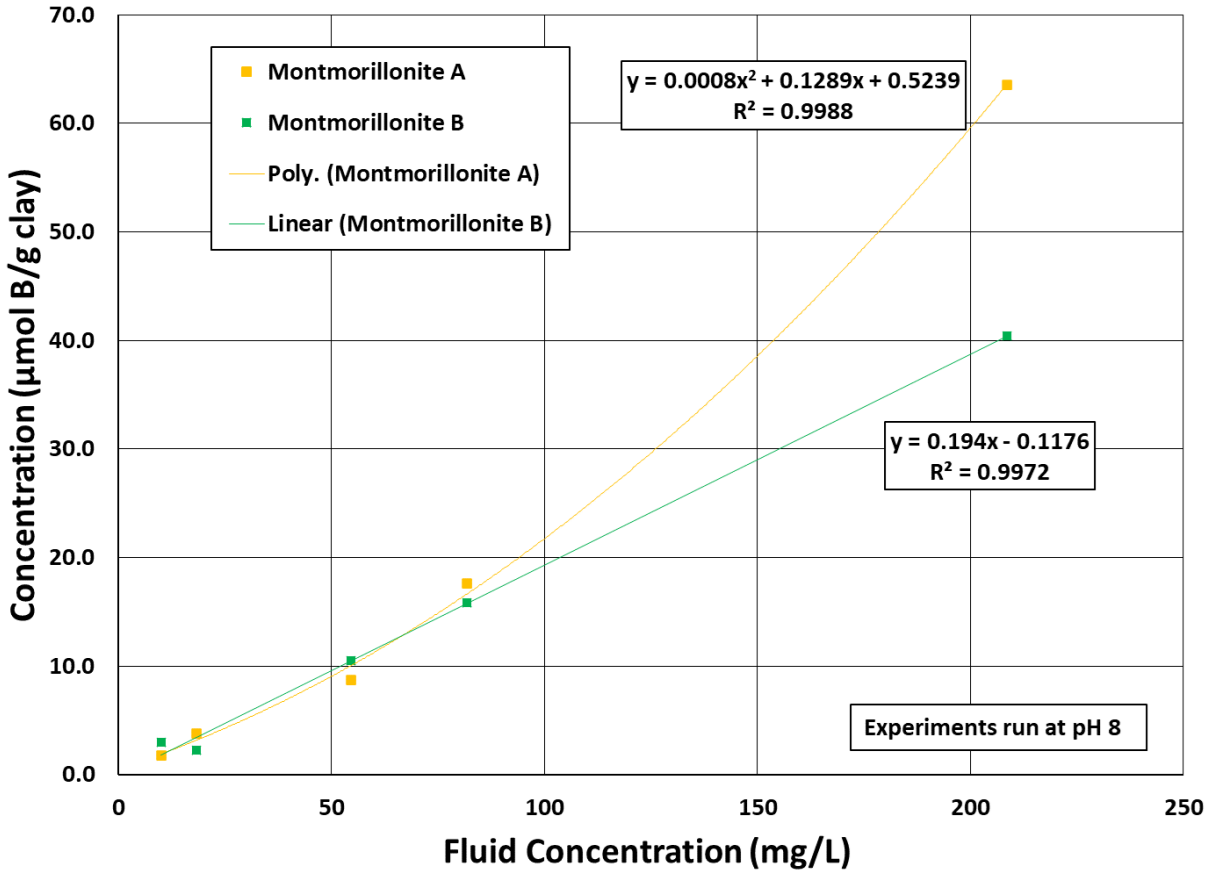

Figure 18: ICP-OES initial fluid concentration vs adsorbed concentration. Results from second preliminary test displaying the positive relationship between initial boron concentration in the fluid and the final concentration adsorbed onto the clay. Montmorillonite A fitted with polynomial relation; Montmorillonite B fitted with linear relation.

Table 9: Results for calculating concentrations used for K_d calculations and isotherm fitting.

Sample	C_o (mg B/L)	pH	Ionic Strength	Concentration on solid (mg B/kg)	C_i (mg B/L)	C_0 (M)	Log(C)	Log(x/m)
MontB	10.0	8	1 M CaCl2	31.9	8.73	9.27E-04	0.941	1.504
MontB	18.2	8	1 M CaCl2	23.9	17.2	1.68E-03	1.237	1.378
MontB	54.6	8	1 M CaCl2	113	50.1	5.05E-03	1.700	2.054
MontB	81.9	8	1 M CaCl2	171	75.0	7.57E-03	1.875	2.233
MontB	209	8	1 M CaCl2	437	183	1.93E-02	2.263	2.640
MontB	753	8	1 M CaCl2	5310	647	6.97E-02	2.811	3.725
MontB	209	6	1 M CaCl2	215	200	1.93E-02	2.301	2.332
MontB	209	9	1 M CaCl2	1200	161	1.93E-02	2.205	3.079
MontB	209	10	1 M CaCl2	1870	134	1.93E-02	2.126	3.272
MontA	10.0	8	1 M CaCl2	19.0	9.25	9.27E-04	0.966	1.279
MontA	18.2	8	1 M CaCl2	40.9	16.6	1.68E-03	1.219	1.611
MontA	54.6	8	1 M CaCl2	93.8	50.9	5.05E-03	1.706	1.972
MontA	81.9	8	1 M CaCl2	190	74.3	7.57E-03	1.871	2.279
MontA	209	8	1 M CaCl2	687	181	1.93E-02	2.258	2.837
MontA	209	6	1 M CaCl2	313	196	1.93E-02	2.292	2.496
MontA	209	7	1 M CaCl2	431	191	1.93E-02	2.282	2.635
MontA	209	9	1 M CaCl2	1260	158	1.93E-02	2.199	3.100
MontA	209	10	1 M CaCl2	2000	128	1.93E-02	2.109	3.301

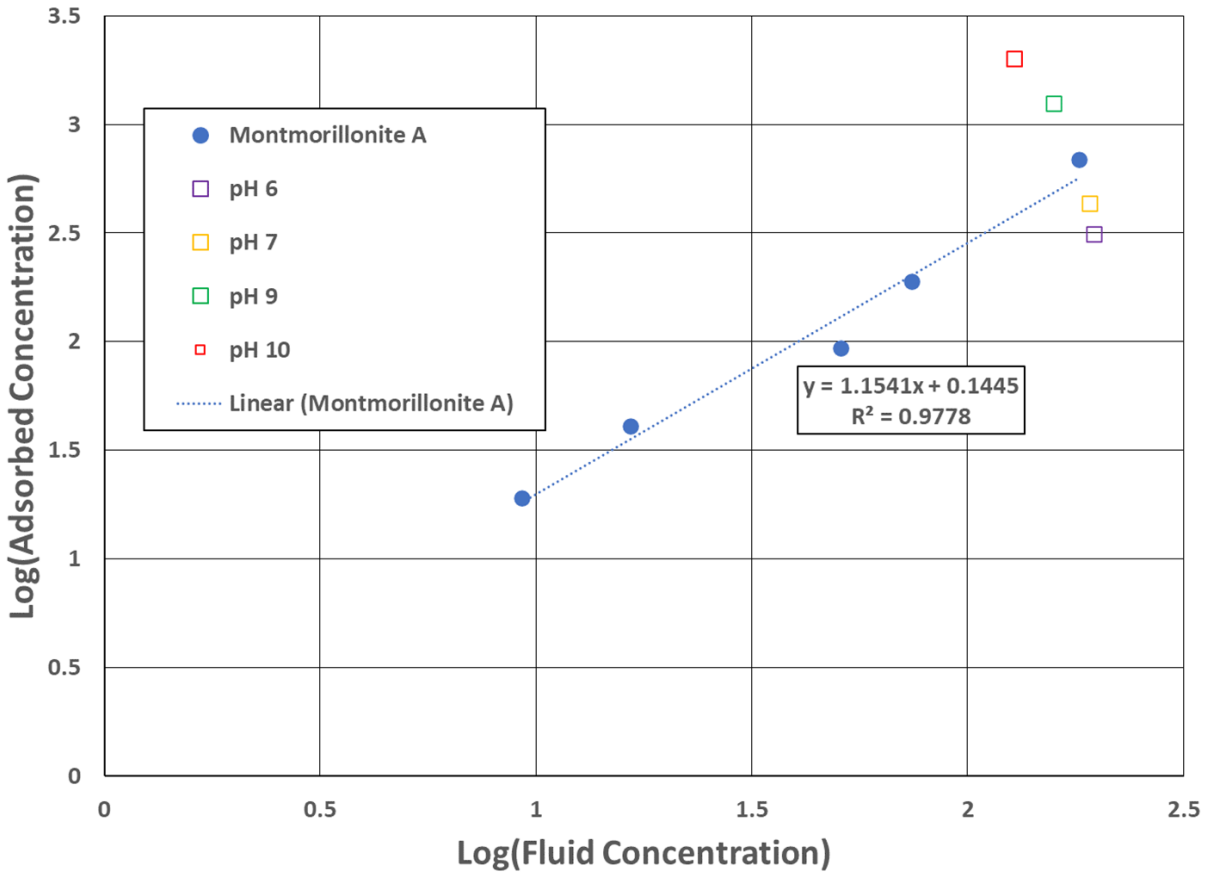

Figure 19: Freundlich fitting and K_d calculation for Montmorillonite A

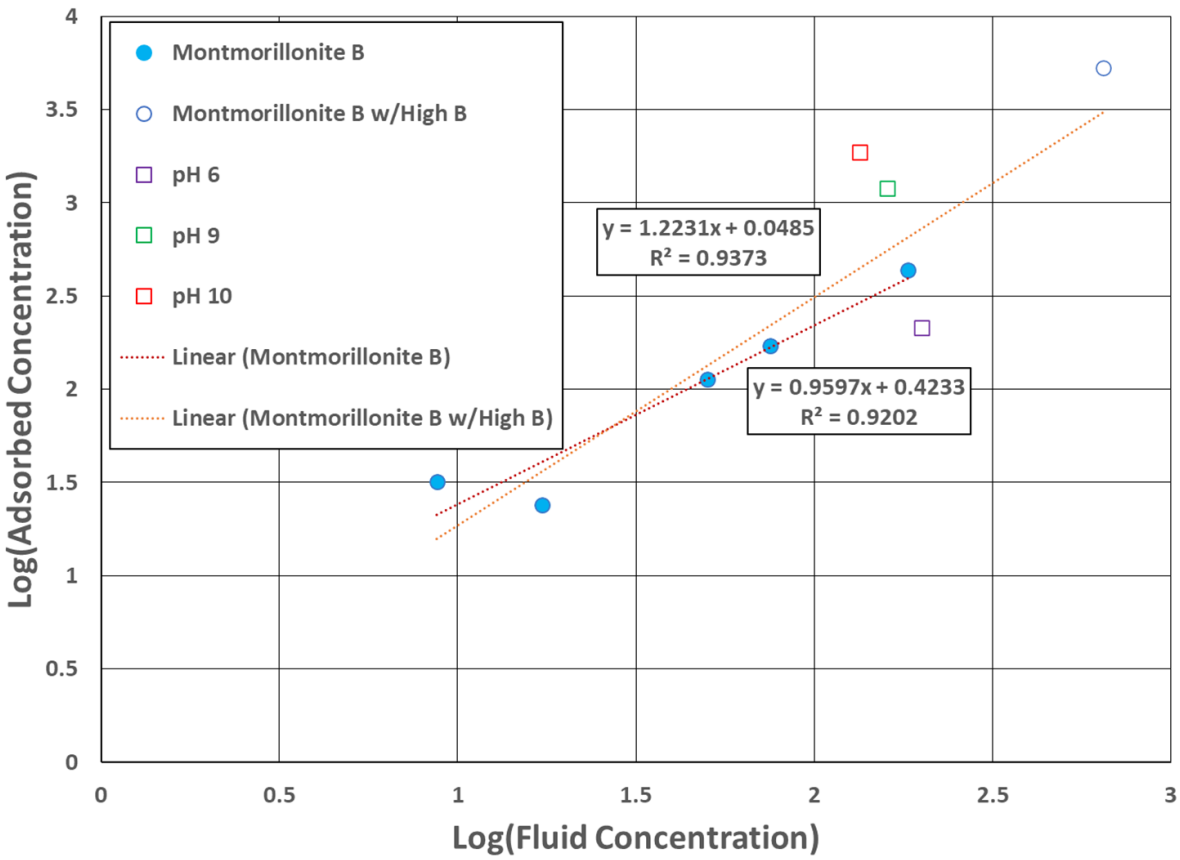

Figure 20: Freundlich fitting and K_d calculation for Montmorillonite B both using the high B point and without

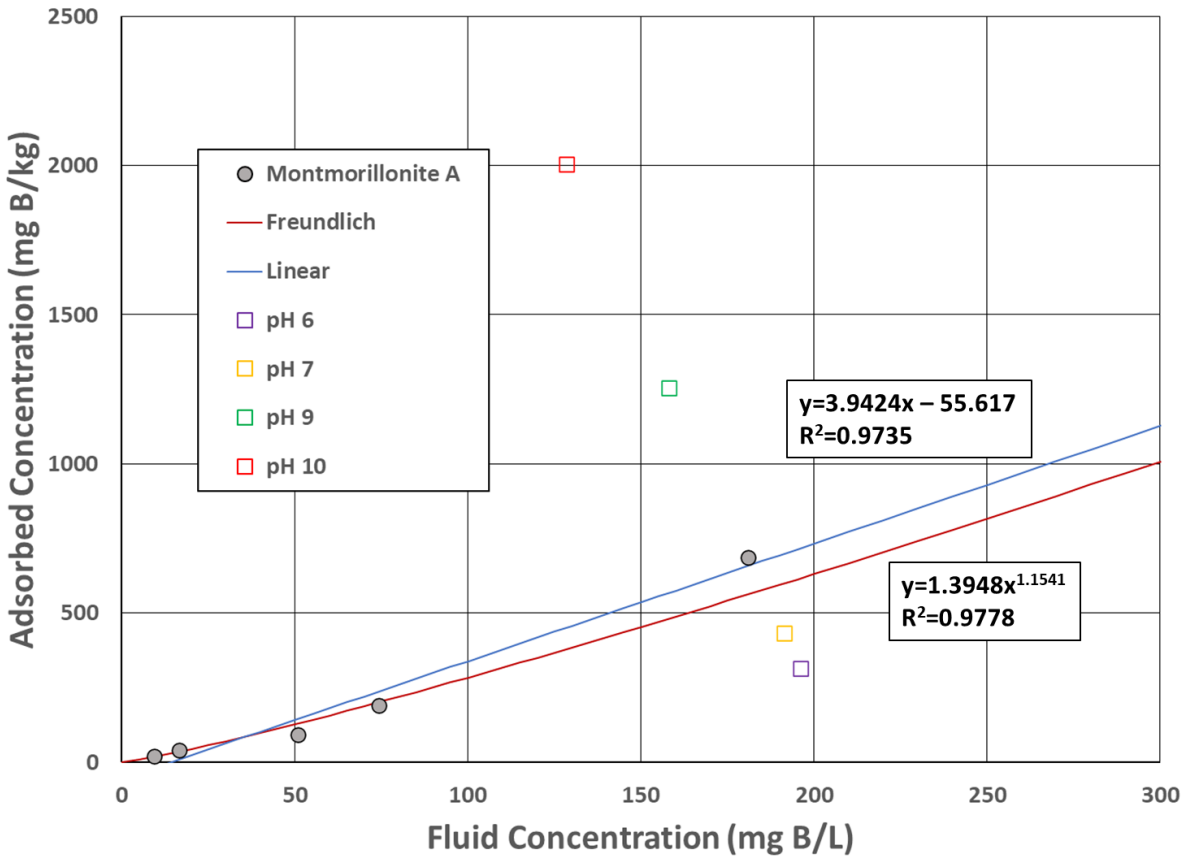

Figure 21: Adsorption isotherms for Montmorillonite A with both Freundlich and Langmuir (linear) fitting

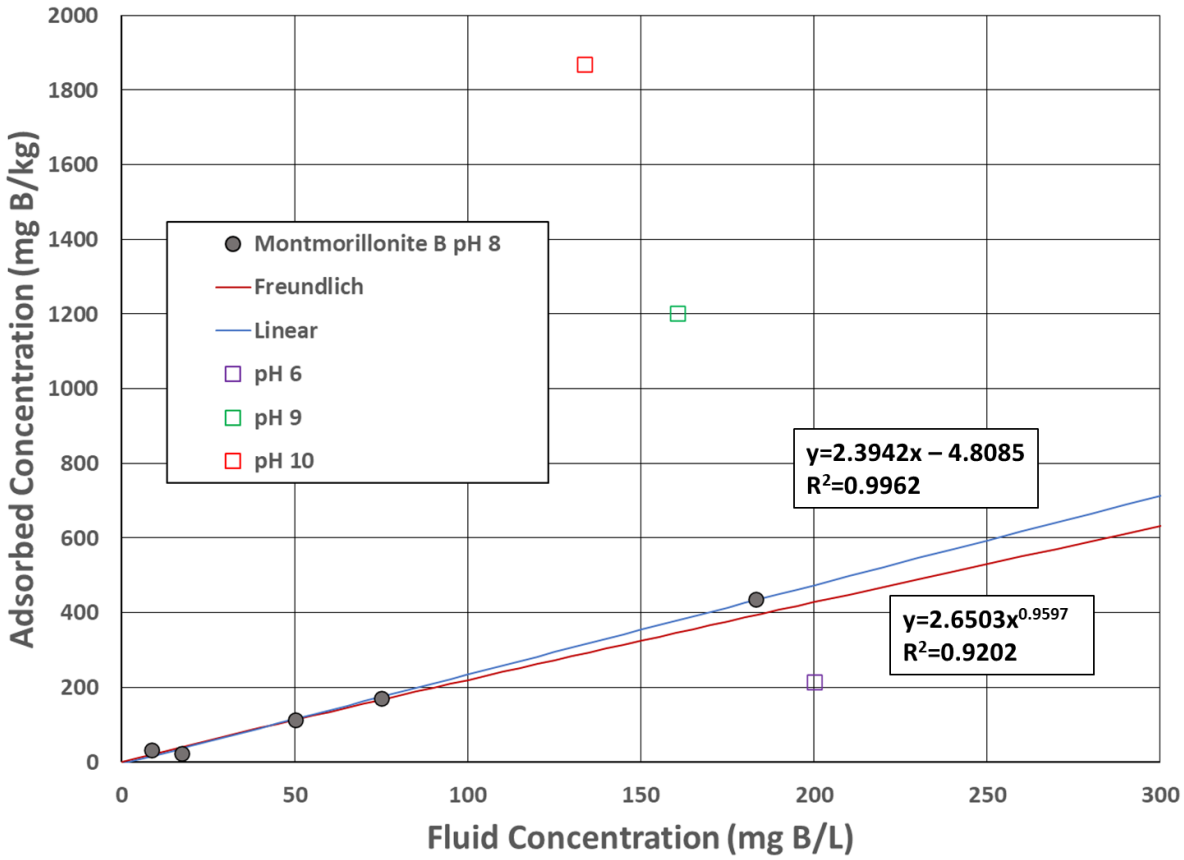

Figure 22: Adsorption isotherms for Montmorillonite B using both Freundlich and Langmuir (linear) fitting

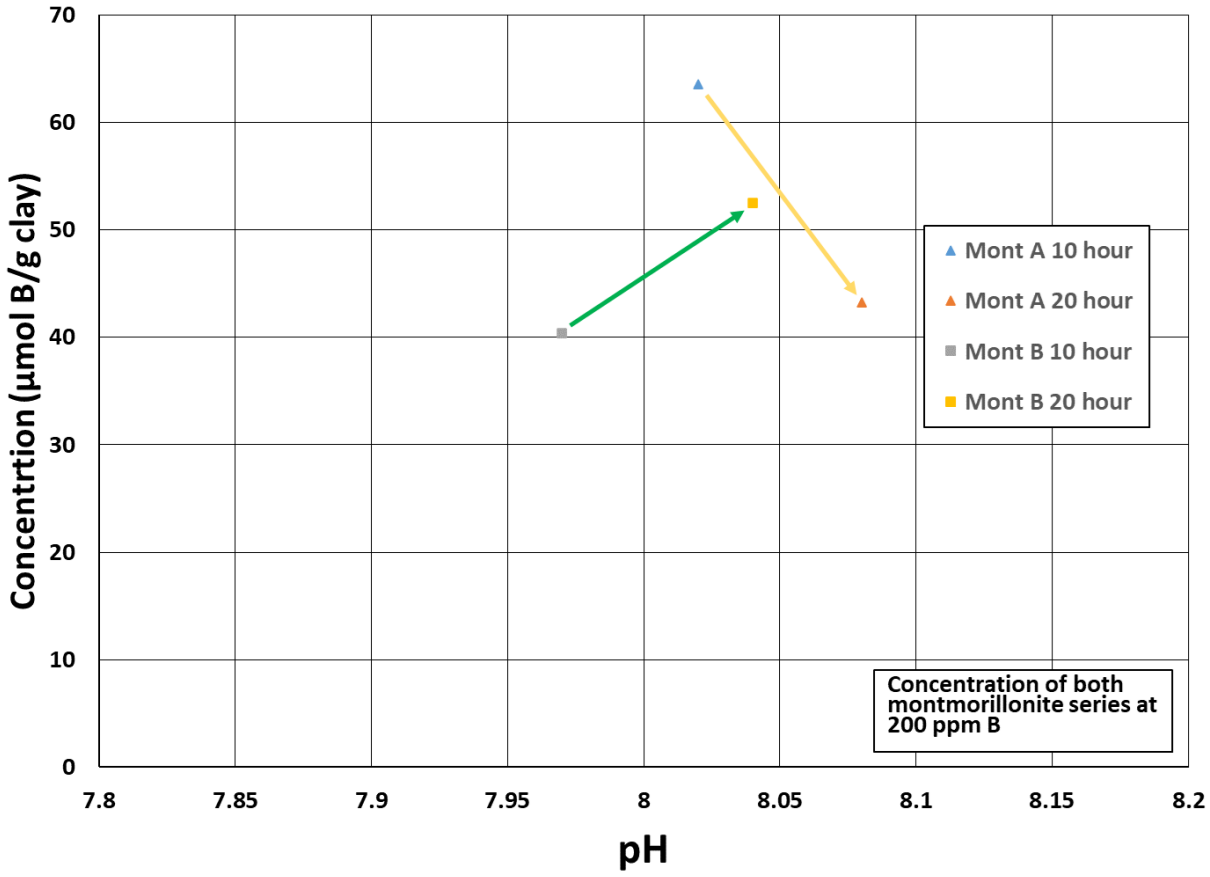

Figure 23: ICP-OES adsorption time effect. Results from second preliminary test displaying the relationship between boron adsorption to the clay and time given for adsorption, showing that adsorption occurs fairly quickly within 10 hours.

For the pH experiments, the pH was varied from 6 to 11 and all were at a concentration of 200 ppm B. This experiment was seeking to replicate past experiments from the literature (*Karahan et al.*, 2006) to determine if the montmorillonite clays used would have a similar peak sorption around pH 8-9. The montmorillonite samples used displayed much more adsorption (**Figure 24**) than the literature In addition to our samples displaying much more adsorption, Montmorillonite B did not display the expected trend from the literature with the expected peak at pH 8-9, while Montmorillonite A was similar. Montmorillonite B instead saw the lowest adsorption at pH 6 and

saw an almost exponential increase in adsorption through pH 11, with the greatest adsorption at 11. Meanwhile, Montmorillonite A saw peak adsorption around a pH of ~8.5, which fitted with previous literature

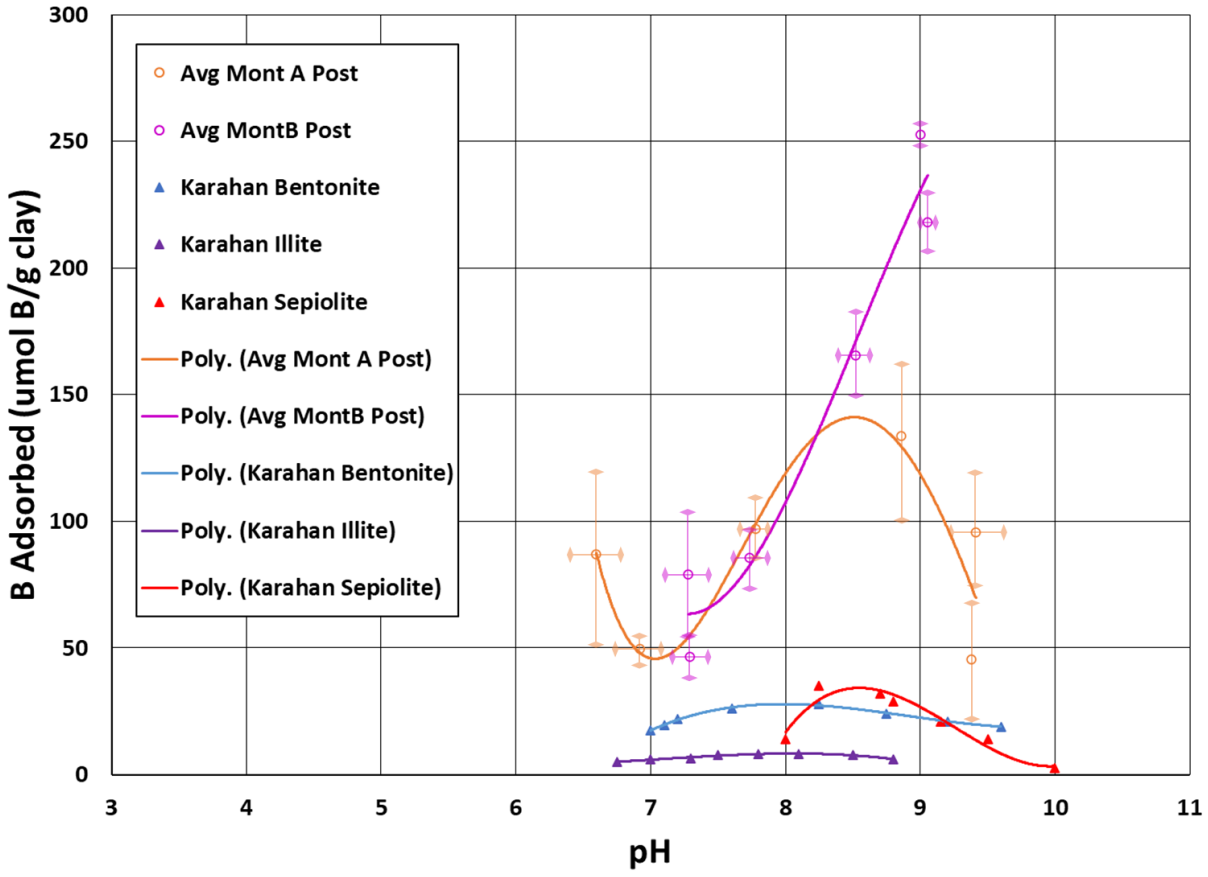

Figure 24: ICP-OES second and third adsorption analysis compared with Karahan. Results from second preliminary test displaying the relationship between boron adsorption to the clay and pH. The Karahan results from the literature are included for reference. Our results for Montmorillonite B did not match the patterns form Karahan, while Montmorillonite A did.

Preliminary LIBS Analysis

The unaltered clay samples and one of the boron-enriched clays from the first adsorption test (>500 ppm B sample) were also analyzed via LIBS for baseline chemistry analysis of the clays

and to check if boron could be detected on the one enriched sample (**Table 10**). The results displayed show that the clay samples used in these experiments cover a wide range of mineral chemistry including high magnesium and high iron clays, in addition to more traditional terrestrial clay chemistries higher in aluminum (**Figure 25A-F**). Within each individual clay standard, the composition is fairly homogeneous. These chemical abundances were backed up by analysis run by ActLabs using ICP-MS (Inductively Coupled Plasma – Mass Spectroscopy) and PGNAA (for measuring boron). The results from LIBS and ICP-MS/PGNAA analyses had some significant differences for sample compositions, though this is attributed to LIBS analysis involving point analysis of and the ICP-MS/PGNAA involving bulk analysis. The Rio Tinto clay sample, which was from the borax mine, was analyzed to contain 0.28 wt% B via LIBS analysis, indicating there was a significant and detectable amount of boron found within this clay sample. The montmorillonite sample from our preliminary test analysis that had been exposed with boron was analyzed and determined to contain 0.67 wt% B (**Figure 26**). This calculates to around 5000-6000 ppm B, which is higher than the ICP-OES determined results of ~3000 ppm; however, ICP-OES also measures the average bulk composition of boron on the material while LIBS analysis measures very fine (~0.5 mm) individual points, therefore some variability is to be expected. The EMPA analysis revealed the boron distribution in the Rio Tinto sample to be scattered variably throughout the sample.

Table 10: LIBS major element analysis of clay samples prior to adsorption.

Target	Point	SiO2	TiO2	Al2O3	FeOT	MgO	CaO	Na2O	K2O	Sum of Oxides	Distance (m)	Laser Power	Spectrum Total
Griffithite	1	44.6	0.78	9.4	11.7	9.1	8.5	2.24	0.36	86.65	1.6	100A/95A/95A	6.33E+14
Griffithite	2	44.1	1.07	9.6	12.2	8.7	9.1	2.42	0.39	87.52	1.6	100A/95A/95A	6.39E+14
Griffithite	3	43.3	3.43	10.1	11.9	7.9	8.5	2.68	0.46	88.28	1.6	100A/95A/95A	6.78E+14
Griffithite	4	44.5	0.79	9.6	12.2	8.5	9.7	2.32	0.39	87.97	1.6	100A/95A/95A	5.87E+14
Griffithite	5	43	1.34	9.9	12.9	8.2	9	2.57	0.41	87.4	1.6	100A/95A/95A	6.28E+14
DC132	1	39.2	0.33	4.6	5.5	30.2	2.9	0.12	0.02	82.84	1.6	100A/95A/95A	6.60E+14
DC132	2	38.4	0.34	5.2	5.7	30.2	3.1	0.17	0.12	83.08	1.6	100A/95A/95A	7.09E+14
DC132	3	38.2	0.38	4.7	5.8	30.3	2.9	0.17	0.03	82.48	1.6	100A/95A/95A	7.07E+14
DC132	4	37.8	0.34	5.1	5.8	29.6	3.4	0.26	0.03	82.43	1.6	100A/95A/95A	6.82E+14
DC132	5	37.8	0.37	4.8	5.9	30	3.2	0.18	0.04	82.19	1.6	100A/95A/95A	6.83E+14
JR901	1	48.1	0.2	0	5.5	34.8	0.9	0.06	0	89.53	1.6	100A/95A/95A	4.61E+14
JR901	2	48.5	0.21	0	5.5	34.8	0.7	0.07	0	89.78	1.6	100A/95A/95A	4.56E+14
JR901	3	48.1	0.2	0	5.5	35	0.7	0.06	0.01	89.59	1.6	100A/95A/95A	4.65E+14
JR901	4	49.1	0.21	0	5.4	34.9	0.7	0.07	0	90.37	1.6	100A/95A/95A	4.35E+14
JR901	5	48.8	0.21	0	5.5	34.5	0.8	0.07	0	89.76	1.6	100A/95A/95A	4.30E+14
WMB24b	1	64.7	0.56	17.7	5.3	4.4	1.9	2.89	0.37	97.78	1.6	100A/95A/95A	2.23E+14
WMB24b	2	65.4	0.53	18.5	4.1	4.5	2.1	2.45	0.32	97.82	1.6	100A/95A/95A	1.96E+14
WMB24b	3	66.5	0.53	18.5	3.3	4.4	1.5	2.66	0.35	97.73	1.6	100A/95A/95A	1.71E+14
WMB24b	4	66.2	0.53	19.7	3.4	4.3	1.5	2.75	0.34	98.81	1.6	100A/95A/95A	1.64E+14
WMB24b	5	66.1	0.53	19.2	3.7	4.3	1.5	2.75	0.38	98.33	1.6	100A/95A/95A	1.78E+14
NAU2b	1	64.3	0.23	6.6	22	1.6	2.7	0.56	0.03	98.01	1.6	100A/95A/95A	5.52E+14
NAU2b	2	63.5	0.24	6.7	21.8	1.6	2.6	0.59	0.05	96.99	1.6	100A/95A/95A	5.19E+14
NAU2b	3	63.8	0.24	6.2	21.9	1.6	2.6	0.5	0.03	96.9	1.6	100A/95A/95A	5.12E+14
NAU2b	4	64.3	0.24	6.7	21.4	1.6	2.5	0.54	0.08	97.43	1.6	100A/95A/95A	4.99E+14
NAU2b	5	64.7	0.24	6.9	20.7	1.5	2.5	0.61	0.07	97.15	1.6	100A/95A/95A	4.56E+14
DC131	1	51.8	0.2	0	5.2	35.4	0.8	0.01	0.05	93.4	1.6	100A/95A/95A	3.71E+14
DC131	2	51.1	0.2	0	5.4	35.5	1	0.02	0	93.13	1.6	100A/95A/95A	3.51E+14
DC131	3	54	0.21	0	5.2	36.6	0.3	0.01	0	96.22	1.6	100A/95A/95A	3.15E+14
DC131	4	52.7	0.21	0	5.3	36.3	0.5	0.01	0	95.01	1.6	100A/95A/95A	3.30E+14
DC131	5	52.7	0.21	0	5.1	36.2	0.3	0.01	0.01	94.51	1.6	100A/95A/95A	3.05E+14
JR902	1	48.7	0.2	0	5.2	36.6	0.2	0	0.04	90.95	1.6	100A/95A/95A	5.56E+14
JR902	2	49.5	0.2	0	5.2	36.9	0.3	0	0.02	92.08	1.6	100A/95A/95A	5.51E+14
JR902	3	49	0.2	0	5.2	37.2	0.3	0	0.02	91.86	1.6	100A/95A/95A	5.16E+14
JR902	4	48.7	0.21	0	5.1	37	0.5	0	0.01	91.54	1.6	100A/95A/95A	5.05E+14
JR902	5	49.8	0.2	0	5.2	36.6	0.5	0.01	0.01	92.42	1.6	100A/95A/95A	4.62E+14
BCS203a	1	52.6	0.2	0	5.4	36.2	0.3	0.01	0	94.69	1.6	100A/95A/95A	2.94E+14
BCS203a	2	51.5	0.2	0	5.3	36.8	0.2	0.01	0	93.95	1.6	100A/95A/95A	2.93E+14
BCS203a	3	51.1	0.2	0	5.3	35.8	0.5	0.01	0	92.84	1.6	100A/95A/95A	3.06E+14
BCS203a	4	51.5	0.21	0	5.3	36.1	0.5	0.01	0	93.67	1.6	100A/95A/95A	3.00E+14
BCS203a	5	50.7	0.46	0	5.9	35.7	0.2	0.07	0.02	92.97	1.6	100A/95A/95A	3.26E+14
MB01	1	66.4	0.51	15.1	3.3	3.6	1.1	3.12	0.32	93.5	1.6	100A/95A/95A	2.07E+14
MB01	2	66	0.7	15.6	4.2	3.8	0.5	3.04	0.26	94.11	1.6	100A/95A/95A	2.12E+14
MB01	3	66.1	0.6	17.2	3.7	3.8	1.5	3.29	0.25	96.4	1.6	100A/95A/95A	2.11E+14
MB01	4	66.8	0.64	14	4	3.6	1.6	2.98	0.46	94.2	1.6	100A/95A/95A	2.12E+14
MB01	5	66.9	0.6	15.9	4	3.4	2.1	3.32	0.46	96.65	1.6	100A/95A/95A	1.99E+14
RTB1	1	48.5	0.28	6.1	6.1	14.4	10.2	1.88	1.16	88.6	1.6	100A/95A/95A	3.27E+14
RTB1	2	53	0.6	6.9	6.2	16.4	4.4	2.68	1.84	92.07	1.6	100A/95A/95A	2.94E+14
RTB1	3	55.8	0.48	6.4	5.8	18.5	2.8	2.36	1.77	93.85	1.6	100A/95A/95A	2.55E+14
RTB1	4	55.1	0.46	6.5	5.8	17.9	3.2	2.41	1.75	93.11	1.6	100A/95A/95A	2.69E+14
RTB1	5	54.4	0.45	6.3	5.9	16.9	4.3	2.38	1.58	92.14	1.6	100A/95A/95A	2.67E+14
JR903	1	46.7	0.2	0.8	5.8	35	0.8	0.11	0	89.34	1.6	100A/95A/95A	3.39E+14
JR903	2	46.7	0.2	1.2	5.8	34.3	0.7	0.09	0	88.93	1.6	100A/95A/95A	3.14E+14
JR903	3	47.4	0.21	0.5	5.6	35	0.5	0.07	0	89.29	1.6	100A/95A/95A	3.35E+14
JR903	4	46.7	0.2	0.2	5.5	34.6	0.7	0.04	0	88.04	1.6	100A/95A/95A	3.72E+14
JR903	5	46	0.2	1.2	5.4	34.2	0.5	0.05	0	87.56	1.6	100A/95A/95A	3.46E+14
WMB24a	1	58.7	0.44	14.4	3.7	9.5	2.1	1.36	0.55	90.8	1.6	100A/95A/95A	3.16E+14
WMB24a	2	61.3	0.62	14.1	4.4	6.2	1	1.73	2.96	92.3	1.6	100A/95A/95A	2.78E+14
WMB24a	3	56.4	0.43	12.1	3.7	7.9	8.1	1.38	0.76	90.74	1.6	100A/95A/95A	3.48E+14
WMB24a	4	58.7	0.47	13.3	3.7	10.9	1.6	1.06	0.59	90.32	1.6	100A/95A/95A	2.98E+14
WMB24a	5	59.4	0.43	15.4	3.8	10.3	2.1	1.26	0.43	93.12	1.6	100A/95A/95A	2.84E+14
SAA1	1	42.9	0.49	8.8	9.2	12.3	10	0.62	0	84.19	1.6	100A/95A/95A	3.95E+14
SAA1	2	45	0.5	9.4	9.8	12	8.7	0.78	0.01	86.27	1.6	100A/95A/95A	3.79E+14
SAA1	3	43.4	0.49	8.6	9.3	12	10.2	0.71	0	84.8	1.6	100A/95A/95A	3.48E+14
SAA1	4	43.6	0.48	8.9	9	11.5	11.2	0.71	0	85.32	1.6	100A/95A/95A	3.55E+14
SAA1	5	44.3	0.55	8.9	10.7	11.3	9.6	0.33	0	85.75	1.6	100A/95A/95A	3.54E+14

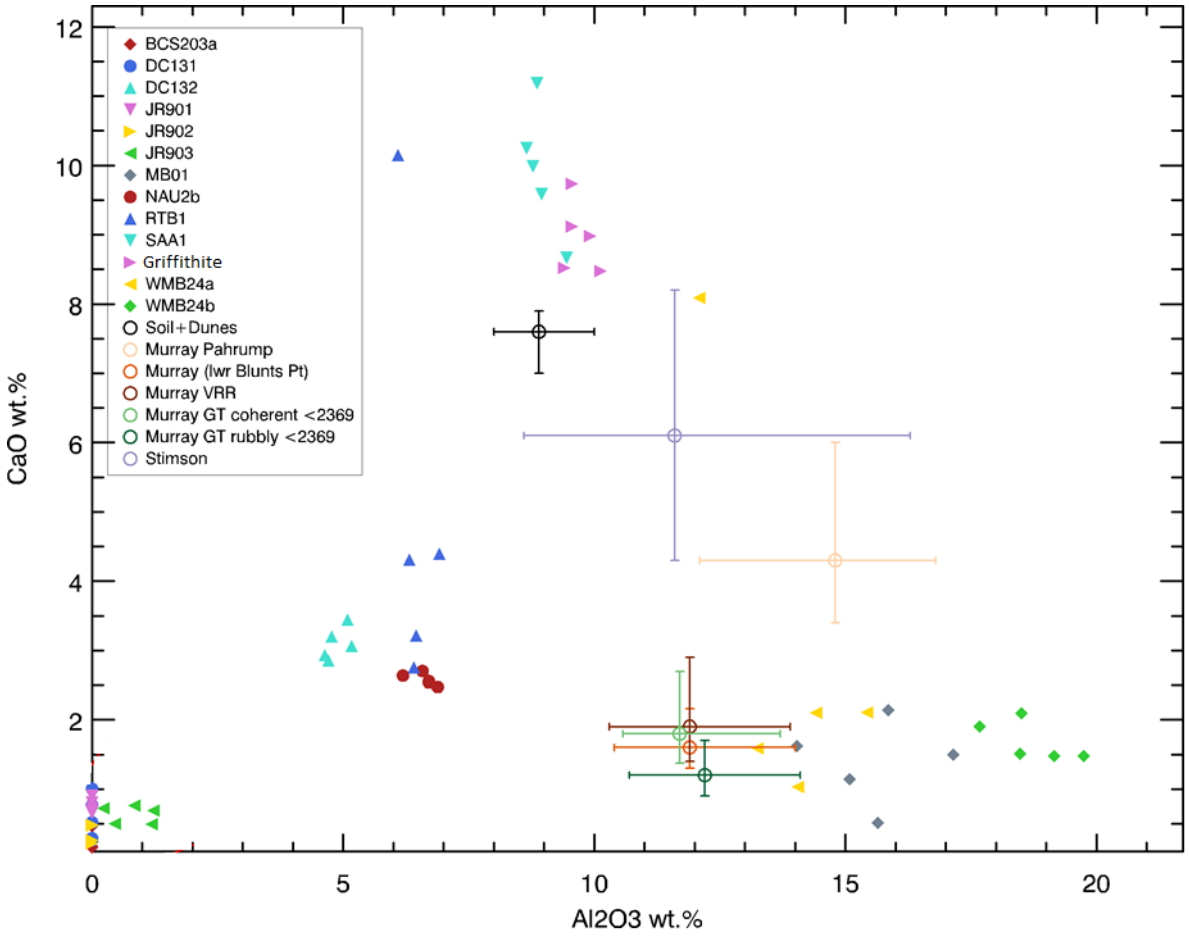

Figure 25 A-F: LIBS analysis clay samples – A) CaO vs Al_2O_3. Chemistry plot comparing sample clays used for boron adsorption analysis with Mars chemistry data from ChemCam LIBS analysis. The Mars samples are represented by the open circles (Soil, Murray, Stimson) and their respective error bars represent the range of variability of Mars chemistry, not instrument error.

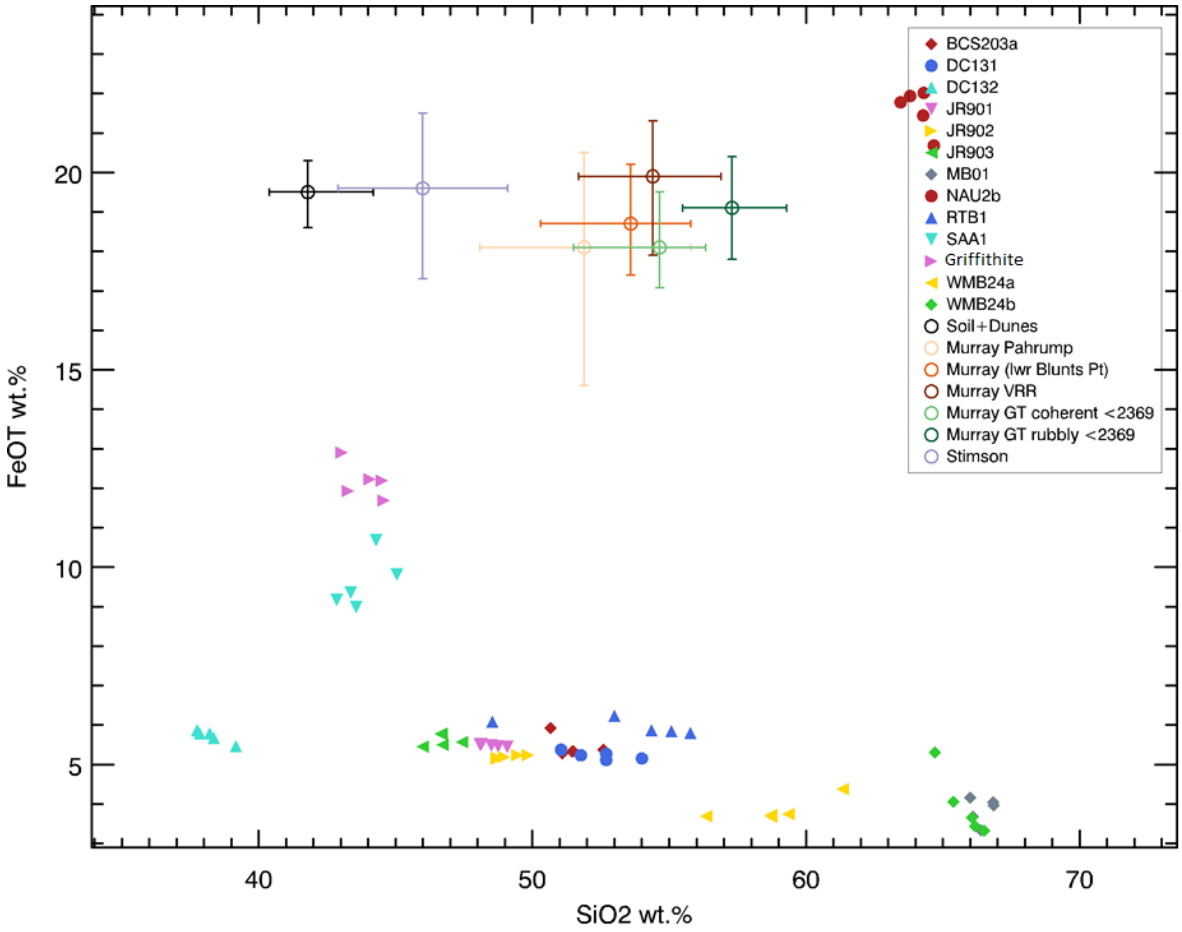

Figure 25 B: LIBS analysis clay sample – FeOT vs SiO_2. Chemistry plot comparing sample clays used for boron adsorption analysis with Mars chemistry data from ChemCam LIBS analysis. The Mars samples are represented by the open circles (Soil, Murray, Stimson) and their respective error bars represent the range of variability of Mars chemistry, not instrument error.

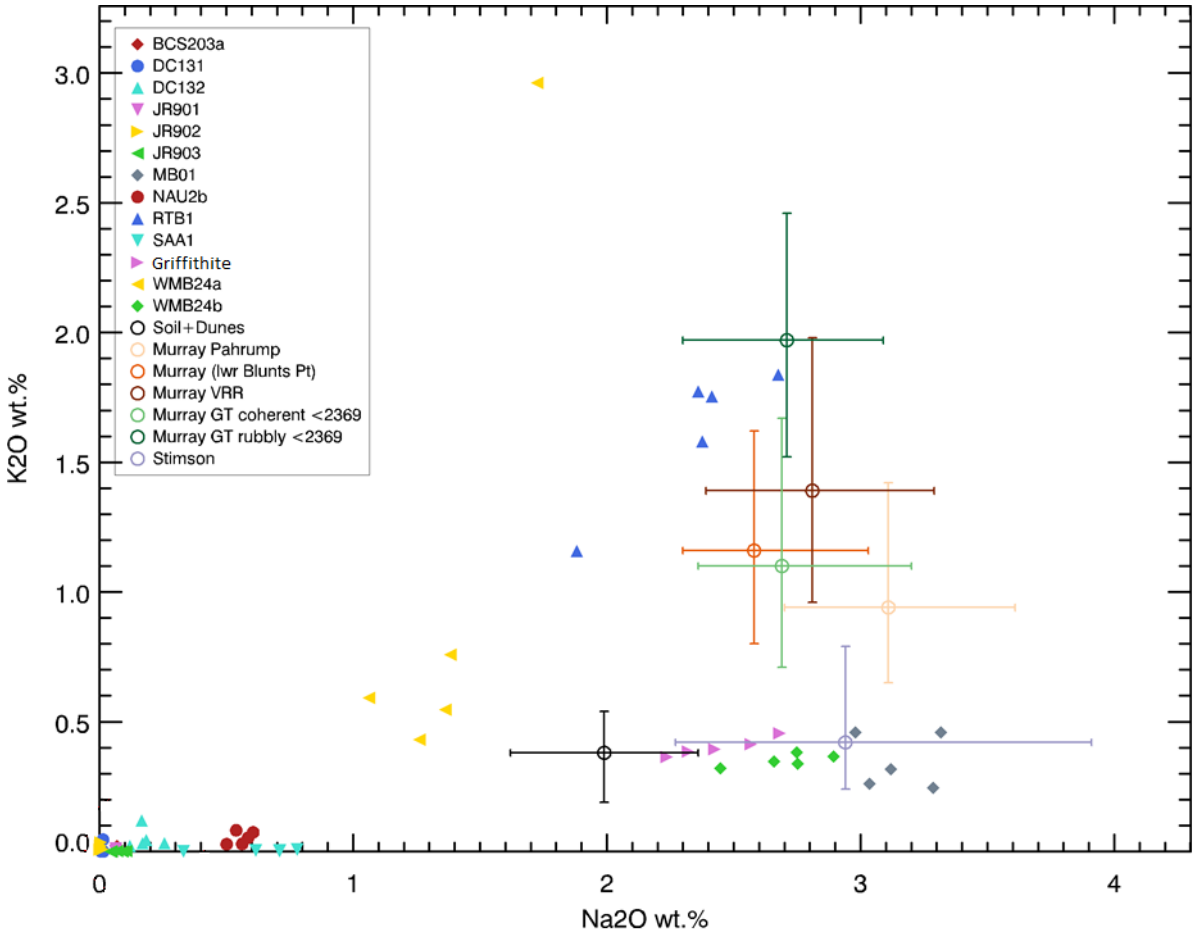

Figure 25 C: LIBS analysis clay simples – K_2O vs Na_2O. Chemistry plot comparing sample clays used for boron adsorption analysis with Mars chemistry data from ChemCam LIBS analysis. The Mars samples are represented by the open circles (Soil, Murray, Stimson) and their respective error bars represent the range of variability of Mars chemistry, not instrument error.

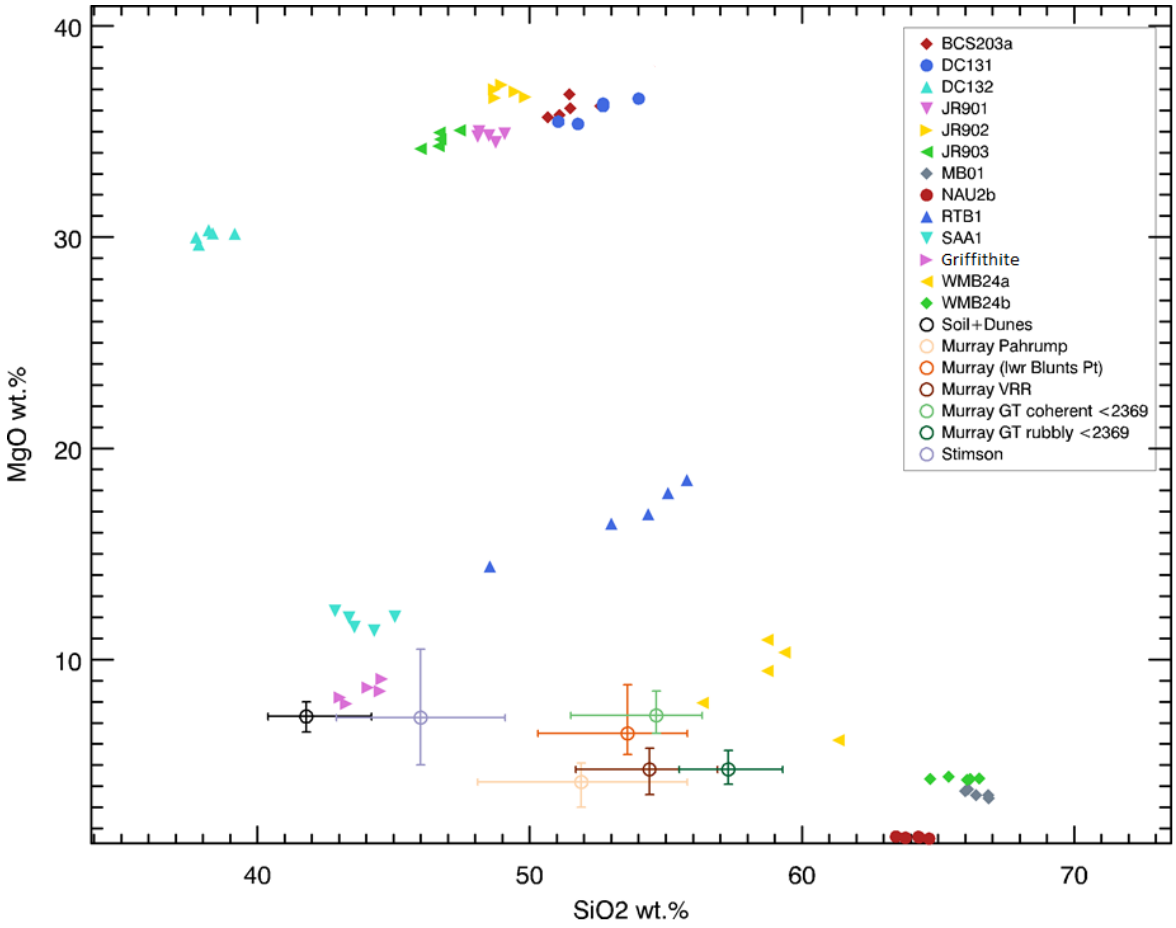

Figure 25 D: LIBS analysis clay simples – MgO vs SiO_2. Chemistry plot comparing sample clays used for boron adsorption analysis with Mars chemistry data from ChemCam LIBS analysis. The Mars samples are represented by the open circles (Soil, Murray, Stimson) and their respective error bars represent the range of variability of Mars chemistry, not instrument error.

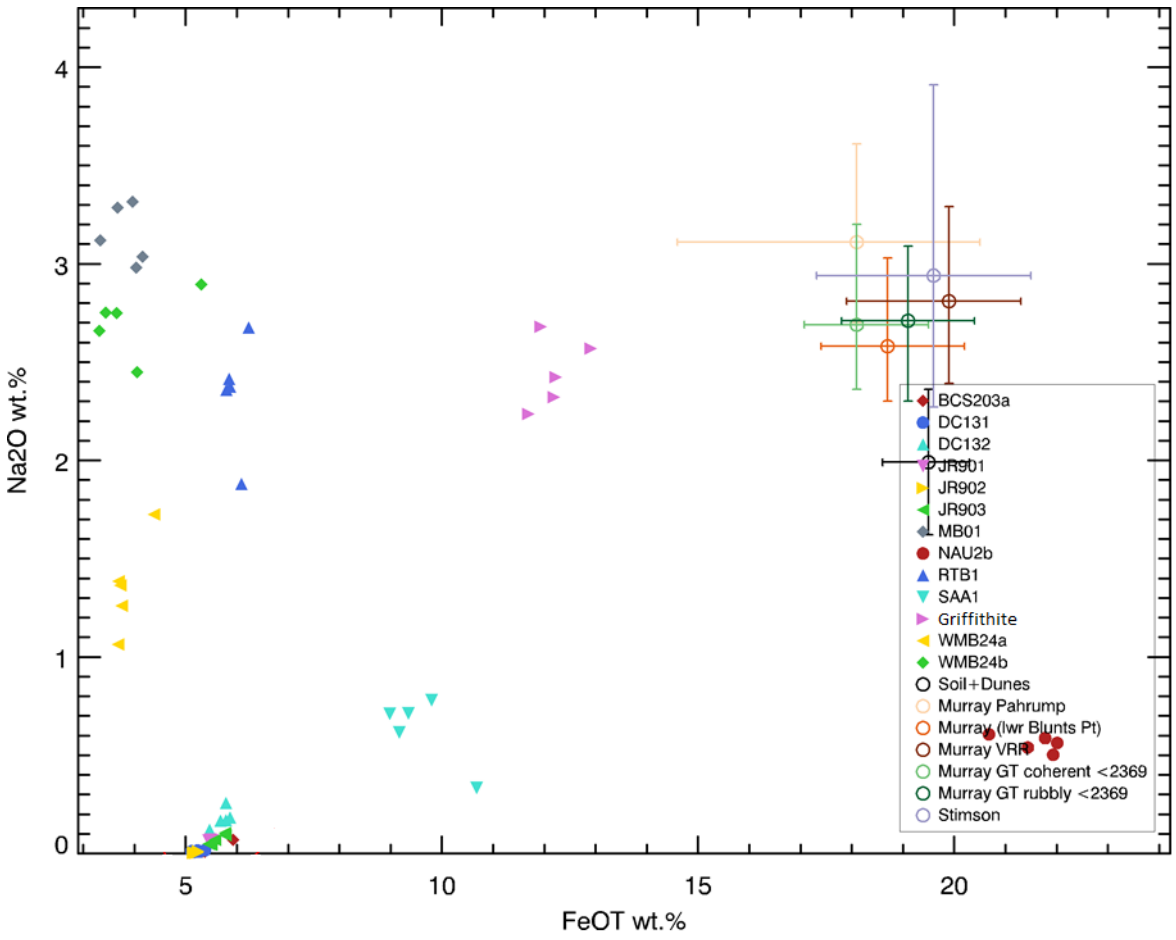

Figure 25 E: LIBS analysis clay simples – Na2O vs FeOT. Chemistry plot comparing sample clays used for boron adsorption analysis with Mars chemistry data from ChemCam LIBS analysis. The Mars samples are represented by the open circles (Soil, Murray, Stimson) and their respective error bars represent the range of variability of Mars chemistry, not instrument error.

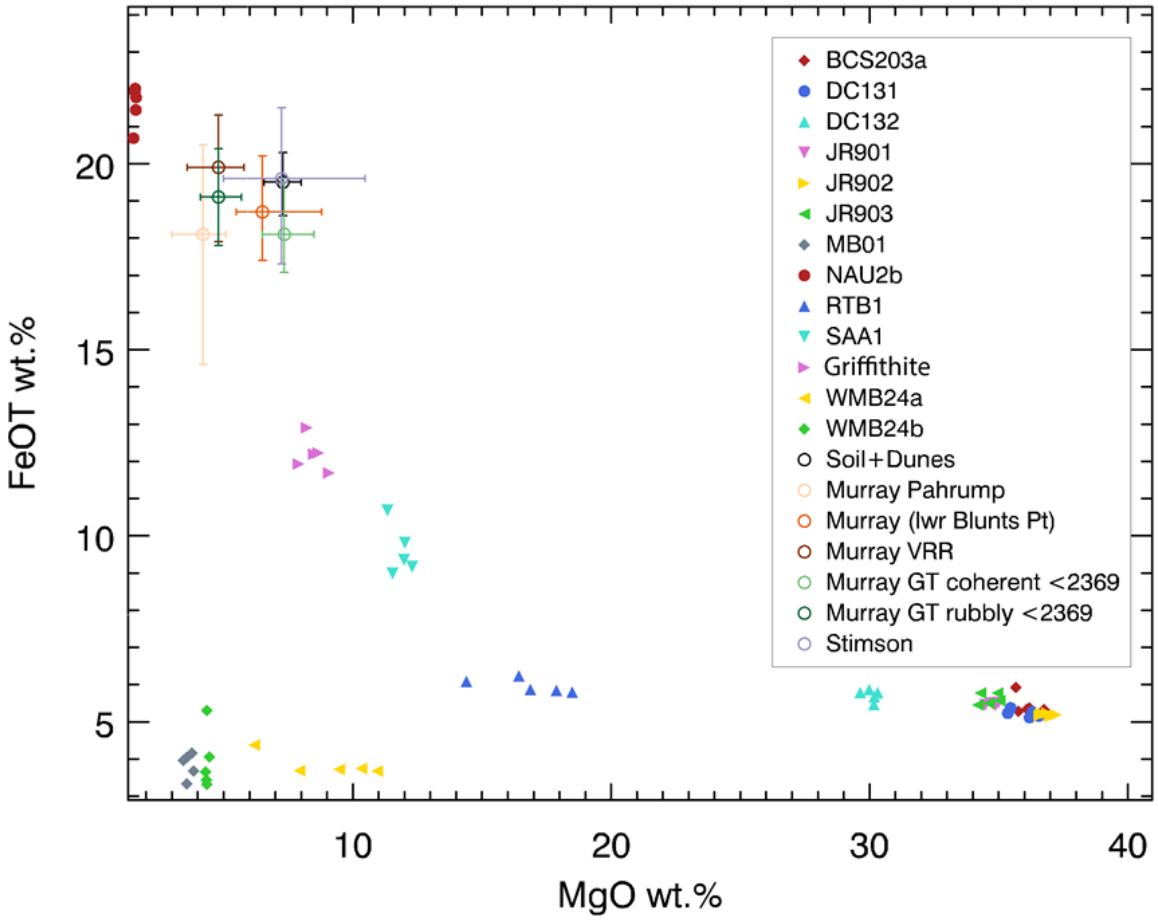

Figure 25 F: LIBS analysis clay simples – FeOT vs MgO. Chemistry plot comparing sample clays used for boron adsorption analysis with Mars chemistry data from ChemCam LIBS analysis. The Mars samples are represented by the open circles (Soil, Murray, Stimson) and their respective error bars represent the range of variability of Mars chemistry, not instrument error.

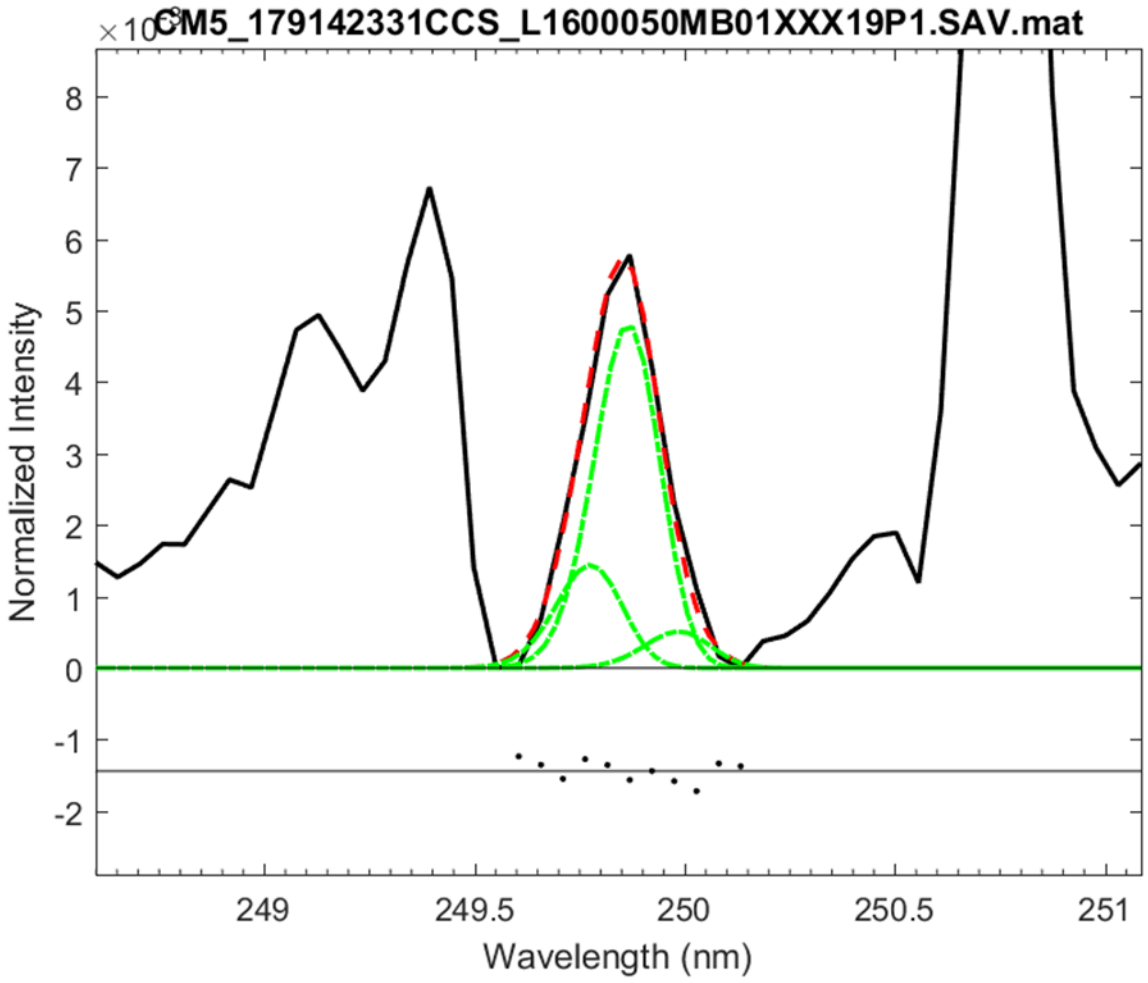

Figure 26: LIBS spectra of boron peak detected from montmorillonite sample sorbed with boron from first preliminary test. The left and center peak are boron peaks, while the right peak is an iron peak.

Beam Analysis – Microbeam

Both SEM and Microprobe were used for analysis of the Rio Tinto clay, but the SEM failed to detect boron and only provided general characterization, while the more sensitive Microprobe was able to detect boron on the sample. The results of the SEM analysis provided contextual close-up images of clay particles (**Figure 27**) of the Rio Tinto clay at high resolution, however the semi-quantitative analysis was unable to detect any boron in the sample (**Figure 28-29**). The analysis

noted significant quantities of Si and Al expected of the sample, being mostly silicate minerals. The analysis also recorded significant quantities of Ca, Na, and K as well as Fe and Mg. This reflects the expected concentration of a phyllosilicate mineral species. As mentioned before, the XRD analysis was unable to identify the clay species in the sample, but the concentration of alkalis and Fe-Mg reflects what would be seen in a typical clay mineral. Some of the calcium is likely attributed to calcite, as the XRD analysis did detect some secondary calcite mixed in with the Rio Tinto sample. However, despite the calculated concentrations lining up relatively well with those calculated by the ActLabs analysis, there was no boron detected in the SEM analysis as it is likely the Z value for boron is too low for the SEM to detect it. Boron, being a low Z element, would have its x-rays easily adsorbed by the sample, preventing detection by the EDS analysis.

The microprobe analysis fared better for boron detection with its EDS analysis. Of the 13 individual analysis points in the probe quantitative analysis (**Table 11**), 6 of the points were able to record detectable amounts of boron. These concentrations range from 0.08 wt% B all the way up to 3.3 wt% B. Four of the six points were low ranging between 0.08 and 0.18 wt% B while the other two points were much higher around 3 wt% B. The average between all 13 points was 0.49 wt% B. Something to consider is that analysis done by ActLabs is a bulk analysis, which takes an average measurement of the whole sample, while the EPMA analysis (and LIBS analysis as well) involves fine point analysis, so the results can vary quite a bit. There is an apparent correlation between boron and calcium and magnesium (**Figure 30 A-C**) from EPMA analysis as the points containing high boron all contained elevated Ca and low Mg, and as Ca decreased in favor of Mg, B all but disappeared. Boron appeared to more likely to be detected on points better reflecting of a clay mineral chemistry (high silica, high Ca/Na, low Fe/Mg). This would indicate that boron is linked with or associated with the clay mineral phases in the sample, potentially via adsorption.

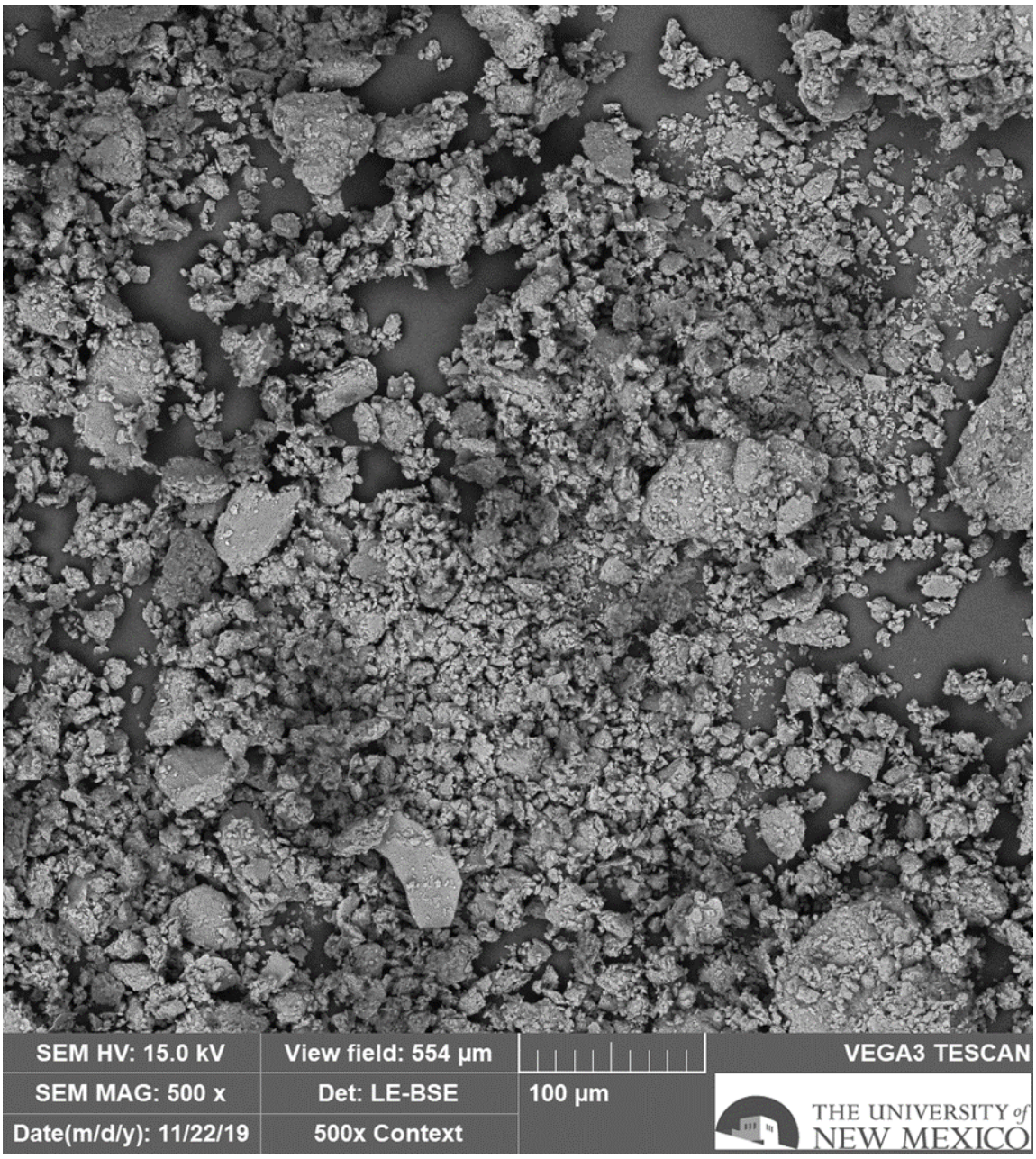

Figure 27: Backscattered SEM image of the Rio Tinto clay sample taken at 500x magnification. This image was taken as a concept image to provide context for the subsequent analysis.

A

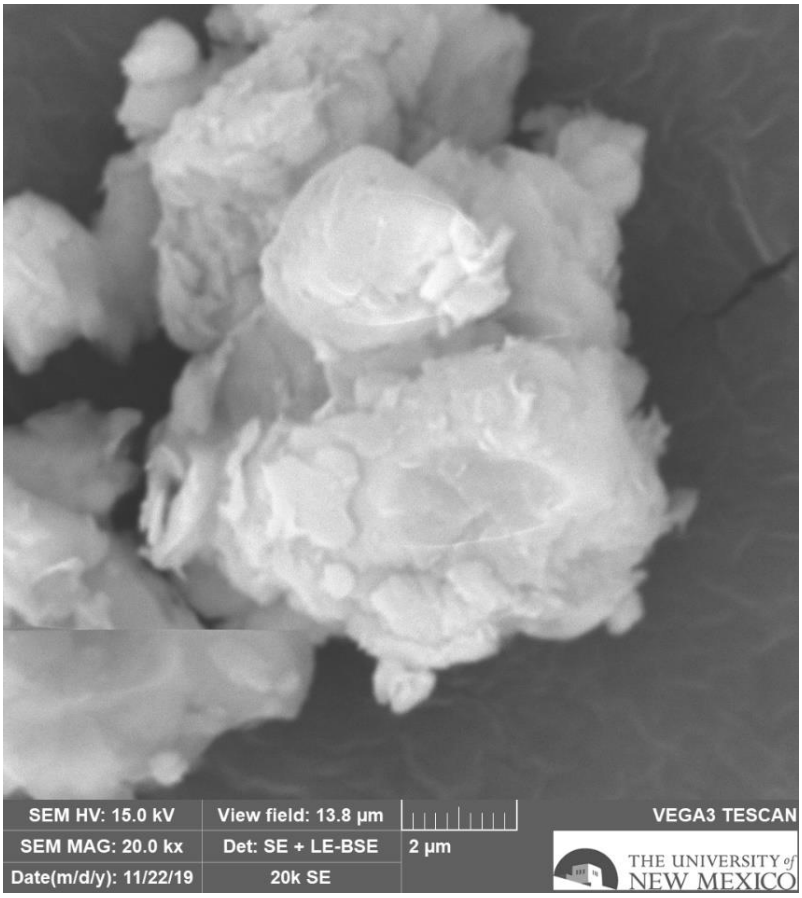

Figure 28: Backscatter SEM of Rio Tinto and EDS scan. A) This depicts a combined secondary electron and backscattered electron image of the Rio Tinto sample where EDS analysis was run. B) This shows the EDS scans showing the elemental peak positions and counts. The Au and Pd can be ignored as this the Au-Pd coating applied to the sample prior to analysis. Much of the Ca is attributed to minor amounts of calcite that was detected during XRD analysis. However, no B was able to be detected in this EDS scan.

B

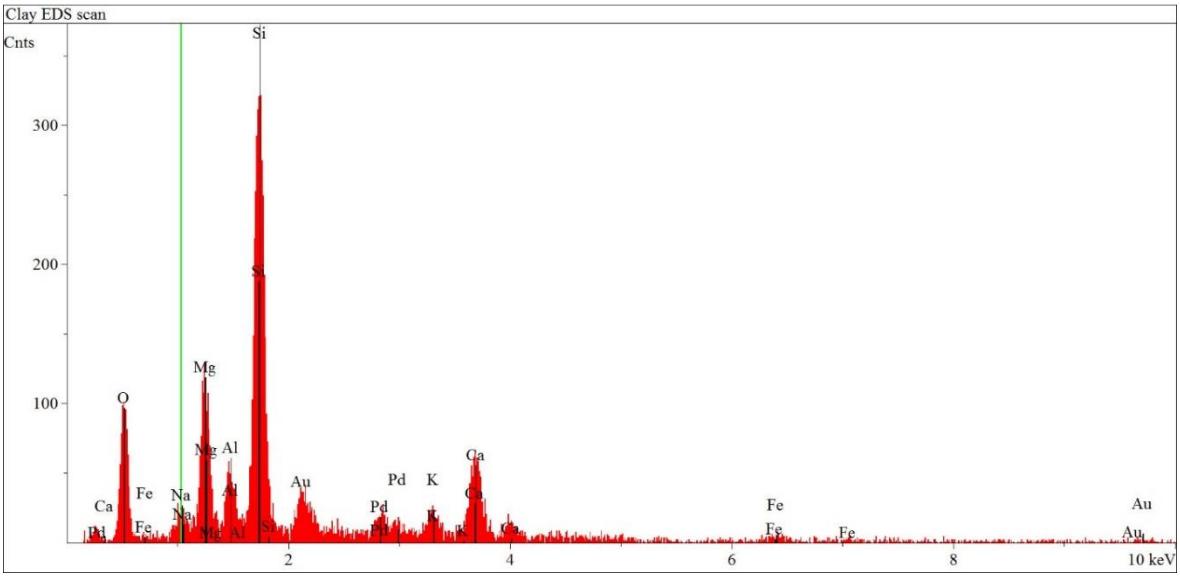

A

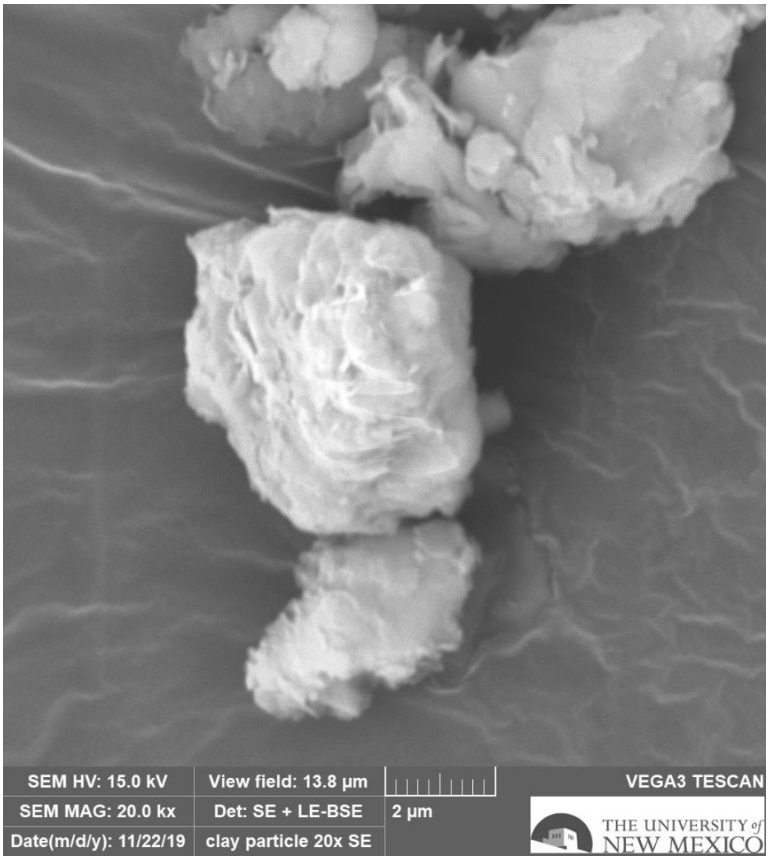

Figure 29: Backscatter SEM of Rio Tinto and EDS scan. A) This depicts a second clay particle under combined secondary electron and backscattered electron image of the Rio Tinto sample where EDS analysis was run. B) This shows the EDS scans showing the elemental peak positions and counts. The Au and Pd can again be ignored as this the Au-Pd coating. Note this particle is likely a purer clay mineral as its Ca peak count is much lower indicating it contains little to none of the additional calcite. However, B was still absent in this EDS scan as well.

B

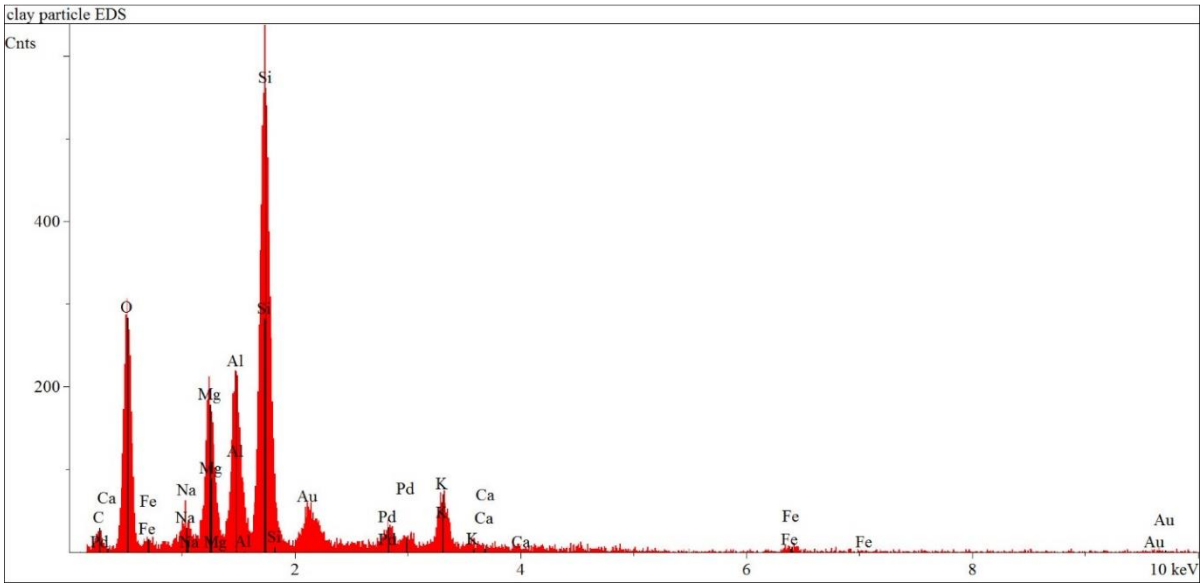

Table 11: EPMA EDS analysis results on the Rio Tinto clay sample covering the abundance of major elements and boron.

SAMPLE	KILO VOLT	CURRENT (pA)	BEAM SIZE (µm)	REL. LINE	Al WT%	Si WT%	K WT%	Ca WT%	B WT%	Fe WT%	Na WT%	Mg WT%	O WT%	Ti WT%	SUM OXIDES
Dravite Standard	15	20	5	1	11.96	15.88	0.06	1.86	3.91	10.94	1.07	5.00	48.04	0.98	99.69
Dravite Standard	15	20	5	2	11.81	15.92	0.06	1.81	3.82	10.94	1.05	4.95	48.30	0.98	99.62
Dravite Standard	15	20	5	3	11.98	15.93	0.05	1.84	3.73	10.76	1.06	5.03	48.26	0.98	99.62
Rio Tinto	15	10	0	1	7.46	25.94	2.00	0.51	0.18	1.73	5.60	5.10	50.52	0.00	99.05
Rio Tinto	15	10	0	3	8.33	25.01	0.55	4.79	3.28	2.33	3.34	0.95	50.99	0.00	99.58
Rio Tinto	15	10	0	4	8.35	20.74	0.49	4.06	2.65	1.77	2.96	0.55	56.43	0.00	98.00
Rio Tinto	15	10	0	5	4.12	27.60	1.87	0.48	0.00	3.07	1.29	8.48	51.92	0.00	98.83
Rio Tinto	15	10	0	6	3.70	28.73	1.46	0.22	0.00	2.52	1.02	6.13	54.57	0.00	98.36
Rio Tinto	15	10	0	7	14.89	22.37	7.83	0.08	0.00	2.01	0.23	1.98	49.70	0.00	99.07
Rio Tinto	15	10	0	8	3.39	25.74	1.82	0.59	0.00	2.29	1.25	9.53	53.70	0.00	98.31
Rio Tinto	15	10	0	9	10.92	32.98	0.99	0.70	0.12	0.60	3.61	1.61	50.53	0.00	102.07
Rio Tinto	15	10	0	12	4.87	23.86	1.88	0.53	0.00	2.19	1.73	8.75	54.28	0.00	98.09
Rio Tinto	15	10	0	13	13.33	22.49	5.21	0.02	0.00	1.52	0.69	3.19	52.18	0.00	98.63
					Al2O3	SiO2	K2O	CaO	B2O3	FeO	Na2O	MgO	O	TiO2	SUM OXIDES
Dravite Standard	15	20	5	1	22.60	33.97	0.07	2.60	12.60	14.07	1.44	8.28	0.00	1.63	97.27
Dravite Standard	15	20	5	2	22.32	34.05	0.07	2.53	12.29	14.07	1.41	8.21	0.00	1.63	96.58
Dravite Standard	15	20	5	3	22.64	34.08	0.06	2.58	12.00	13.85	1.43	8.34	0.00	1.63	96.60
Rio Tinto	15	10	0	1	14.10	55.50	2.41	0.72	0.57	2.23	7.55	8.46	0.00	0.00	91.53
Rio Tinto	15	10	0	3	15.73	53.52	0.67	6.70	10.55	3.00	4.51	1.58	0.00	0.00	96.25
Rio Tinto	15	10	0	4	15.78	44.37	0.59	5.68	8.53	2.27	3.99	0.91	0.00	0.00	82.13
Rio Tinto	15	10	0	5	7.79	59.05	2.25	0.67	0.00	3.95	1.73	14.06	0.00	0.00	89.50
Rio Tinto	15	10	0	6	6.99	61.46	1.76	0.31	0.00	3.25	1.37	10.17	0.00	0.00	85.31
Rio Tinto	15	10	0	7	28.13	47.85	9.43	0.11	0.00	2.58	0.31	3.29	0.00	0.00	91.68
Rio Tinto	15	10	0	8	6.40	55.06	2.19	0.83	0.00	2.95	1.69	15.81	0.00	0.00	84.93
Rio Tinto	15	10	0	9	20.63	70.55	1.19	0.99	0.40	0.77	4.87	2.68	0.00	0.00	102.07
Rio Tinto	15	10	0	12	9.20	51.04	2.26	0.74	0.00	2.82	2.34	14.52	0.00	0.00	82.91
Rio Tinto	15	10	0	13	25.19	48.12	6.28	0.03	0.00	1.96	0.93	5.29	0.00	0.00	87.79

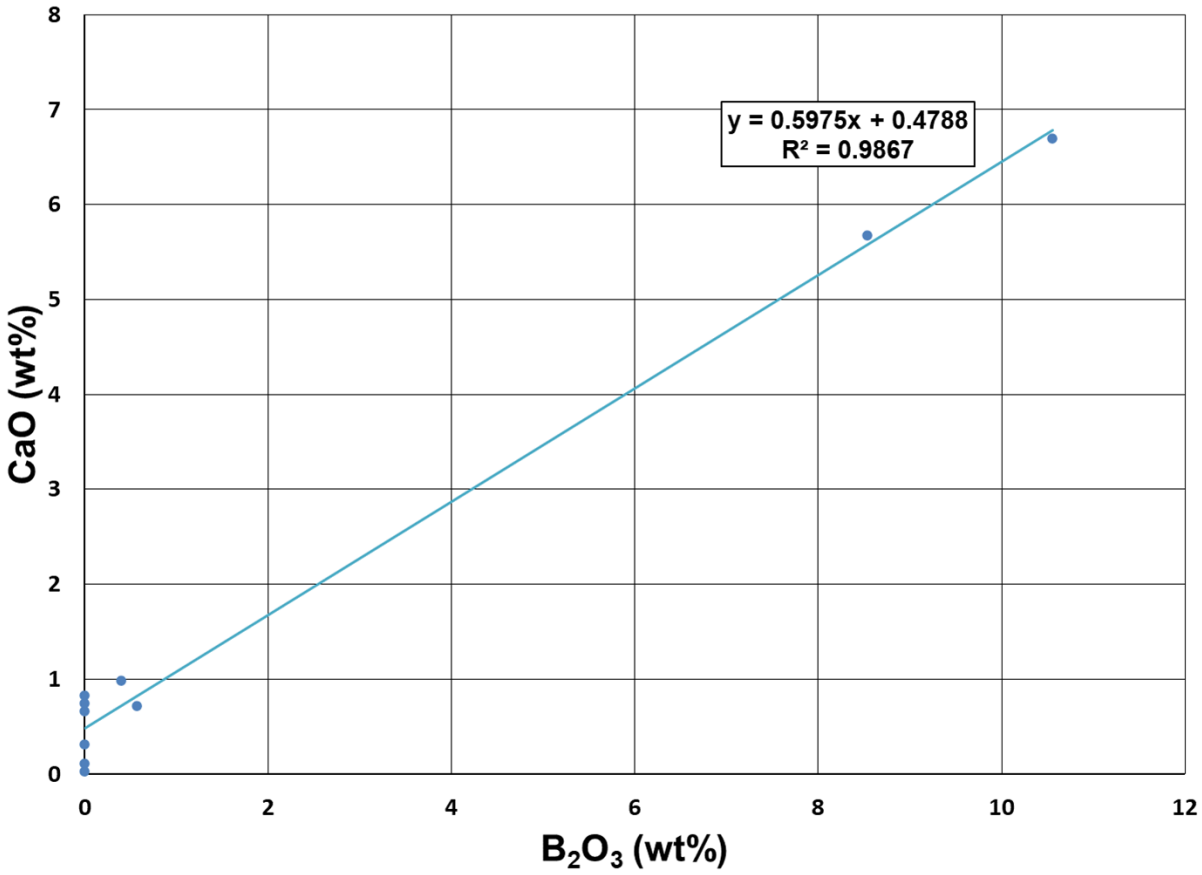

Figure 30 A-C: Rio Tinto EPMA elemental oxide comparison with boron A) Boron correlation with calcium displaying strong positive correlation

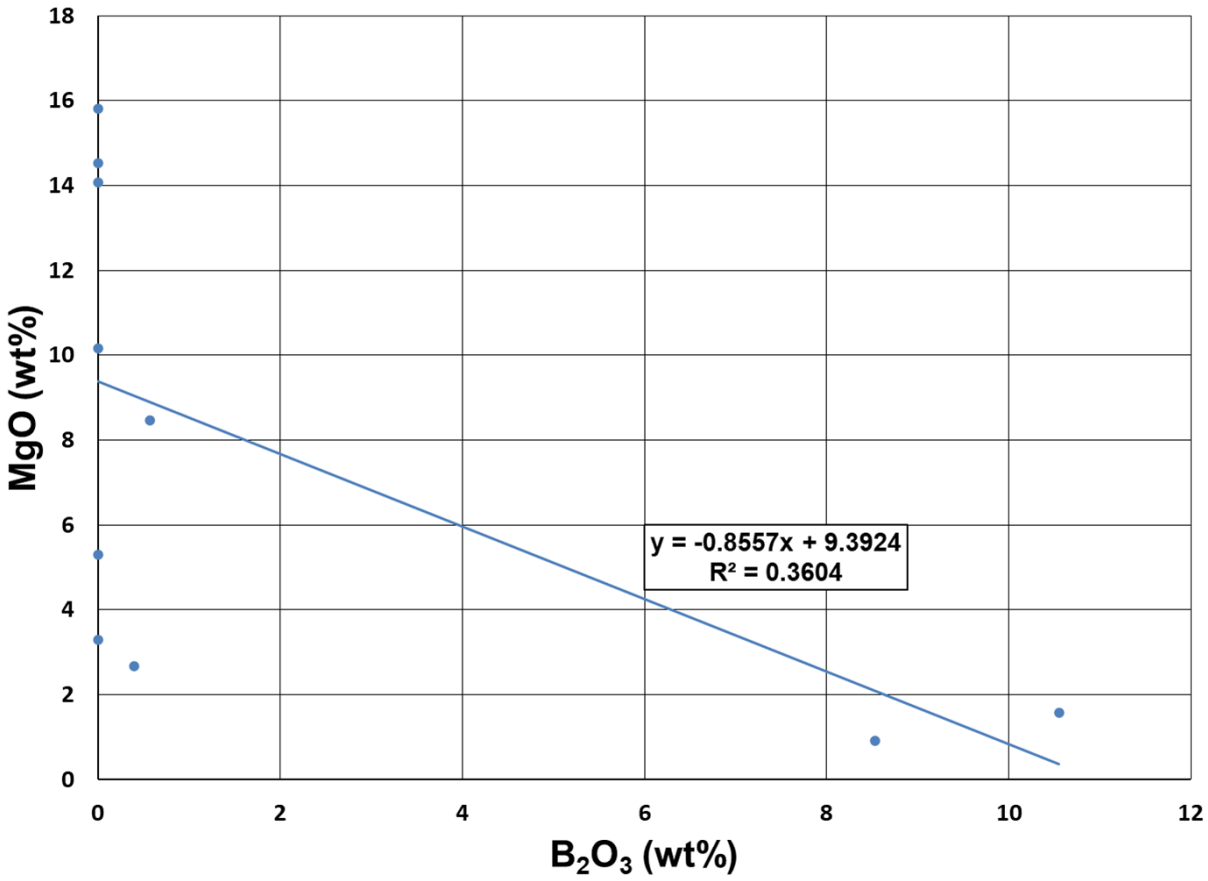

Figure 30B: Boron correlation with magnesium displaying very weak negative correlation

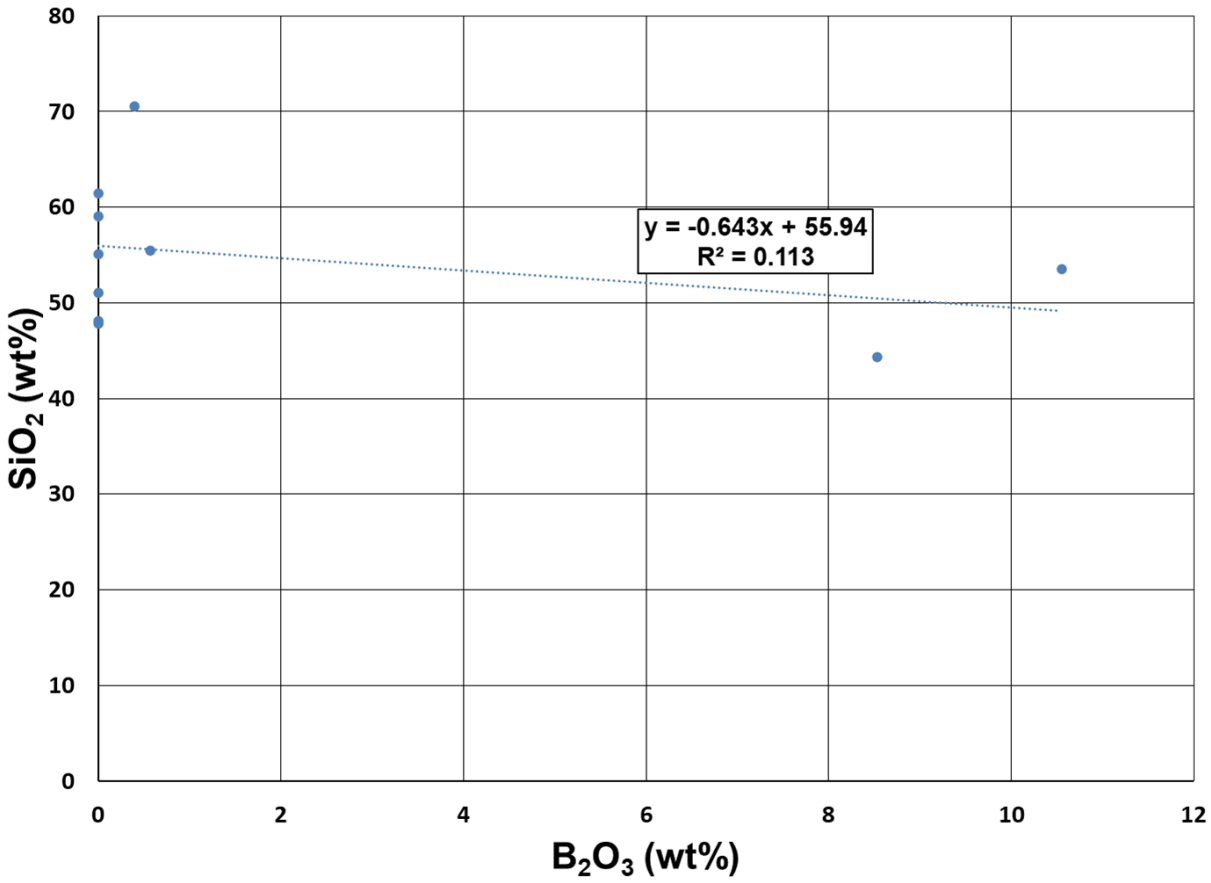

Figure 30C: Boron correlation with silica displaying essentially no correlation

There is also the possibility of boron existing as a borate mineral phase, in association with the clay phases. Additionally, there appears to be a correlation between boron concentration and grain density. In the areas of the sample where the clay grains were more densely packed, the detected concentration of boron was also higher, with it decreasing or disappearing when grains were sparse or when there were gaps in the slide. This indicates that the boron may be linked with the clay and may indicate the boron is either adsorbed to or structurally bound to the clay. If adsorbed, the increased clay particle density creates greater surface area to allow more boron to adsorb to the clay surface. If structurally bound, then the increased quantity of clay will therefore include a

greater detectable amount of boron. In either scenario, it indicates that the boron is linked with the clay and is not likely appearing as a second phase mixed in with the clay.

The first map (**Figure 31**) had an interesting anomaly where high B values were recorded in the gaps where there was not clay, and in the carbon tape. This means either the carbon tape contained a certain amount of boron there was an instrument artifact or calibration standard issue where the instrument is mistaking carbon for boron, or that there was a lot of noise in the signal in relation to the background. The latter two options are more likely as the material used for the carbon coating should not contain any boron, especially in the concentrations indicated by the map scan. Furthermore, prior and subsequent scans run on the EMPA with samples also using carbon tape did not report any elevated boron that could be attributed to contamination in the carbon tape. The second map scan (**Figure 32**) is likely much more representative of the boron concentration throughout the Rio Tinto clay sample. Unlike the other elemental concentrations, which vary throughout the sample, boron is fairly evenly distributed across most of the grains. This would make sense if the boron is assumed to be adsorbed to the surface of the clay grains. The boron is not originally from the clay and was deposited on the surface afterwards, therefore it would have a very even distribution throughout the sample. This is further validated by the boron concentration coinciding with the abundance of clay particles, as if the boron is adsorbed material, it would be seen predominantly in association with the clay.

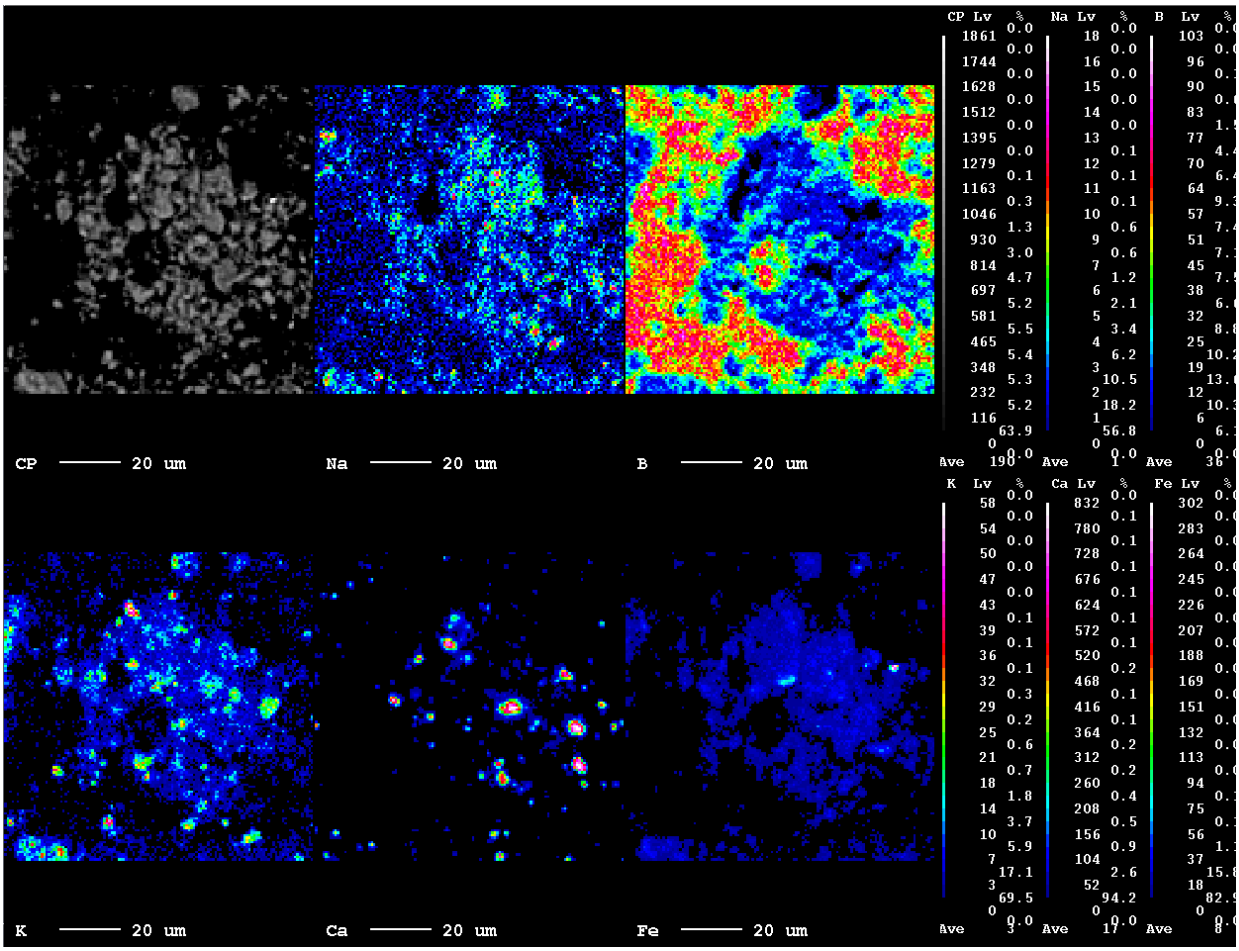

Figure 31: First WDS map scan of Rio Tinto sample on the EPMA, with compositional analysis on Na, B, K, Ca, and Fe. The B map is showing high counts in the regions where the carbon tape is showing, indicating some instrumental calibration error or potential B concentration in the carbon tape itself, though the latter option is unlikely. It may also be possible that the binder used in the carbon stub contains borate.

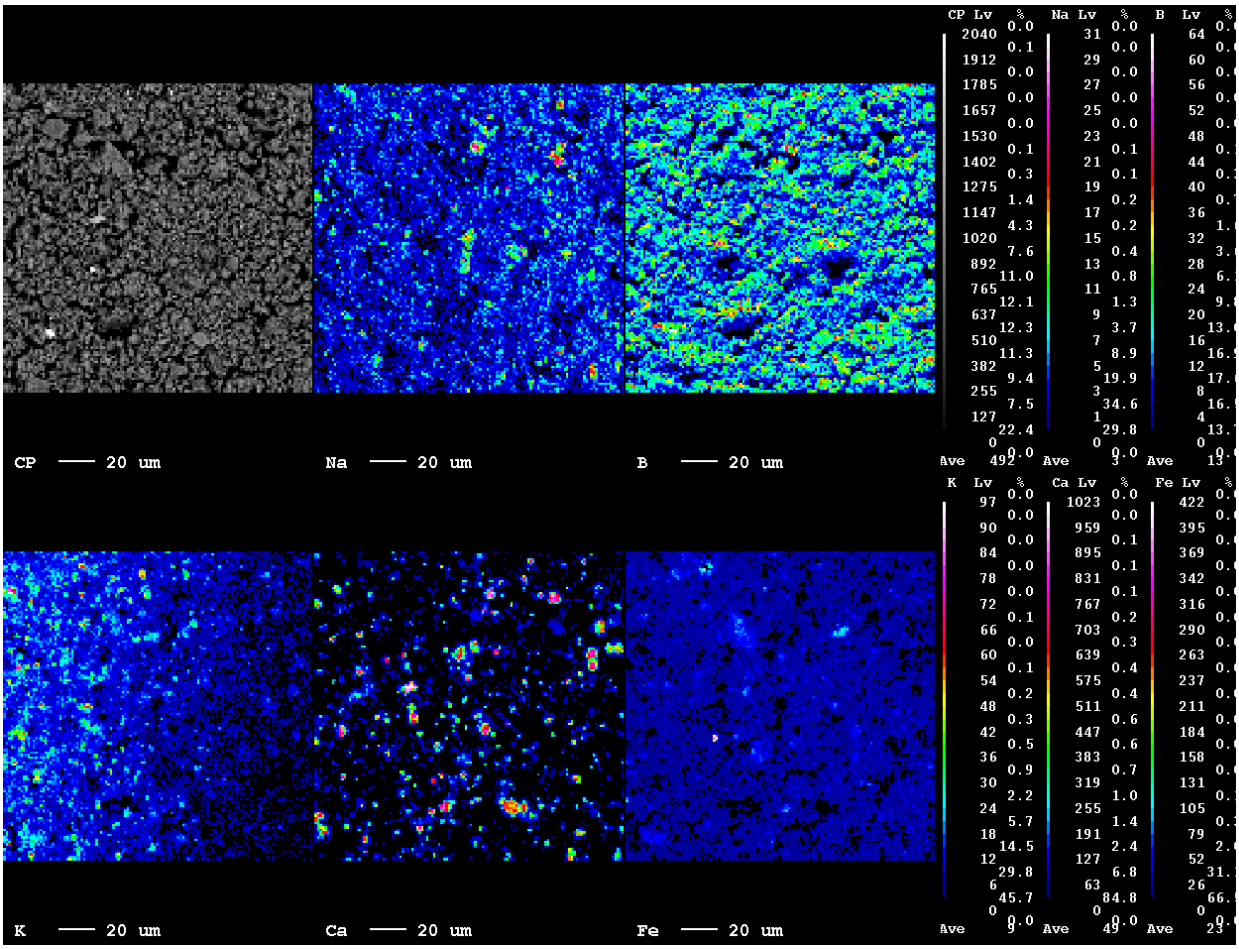

Figure 32: Second WDS map scan of Rio Tinto sample run on the EPMA on the Rio Tinto sample. There is an artifact occurring in the K map on the left side. While the B map shows strong returns throughout the map, they are in reasonable concentrations expected. The even distribution seen throughout the B map across most grains also lends some confirmation that it is indeed a secondary mineral that was deposited on the surface of the already formed clay grains via adsorption.

Geochemical Modeling

The geochemical modeling results revealed that the samples [*Halim et al.*, 2010] consisted of two main classifications: those high in carbonates and those high in sulfates and Cl^-, with both containing high concentrations of alkalis. The comparison plots indicated that boric acid may have a potential correlation with the amount of dissolved Na^+ (**Figure 33**). The plot displaying the relationship between boric acid and Ca^{2+} appeared to show little correlation (**Figure 34**), so the

amount of Ca in solution did not appear to affect the amount of boron in solution or there were enough other ions in solution to mitigate its effect. When analyzing B, Ca, and Na on a ternary diagram (**Figure 35**), while B was much lower than in concentration than the other two, there was a negative correlation between Ca and Na.

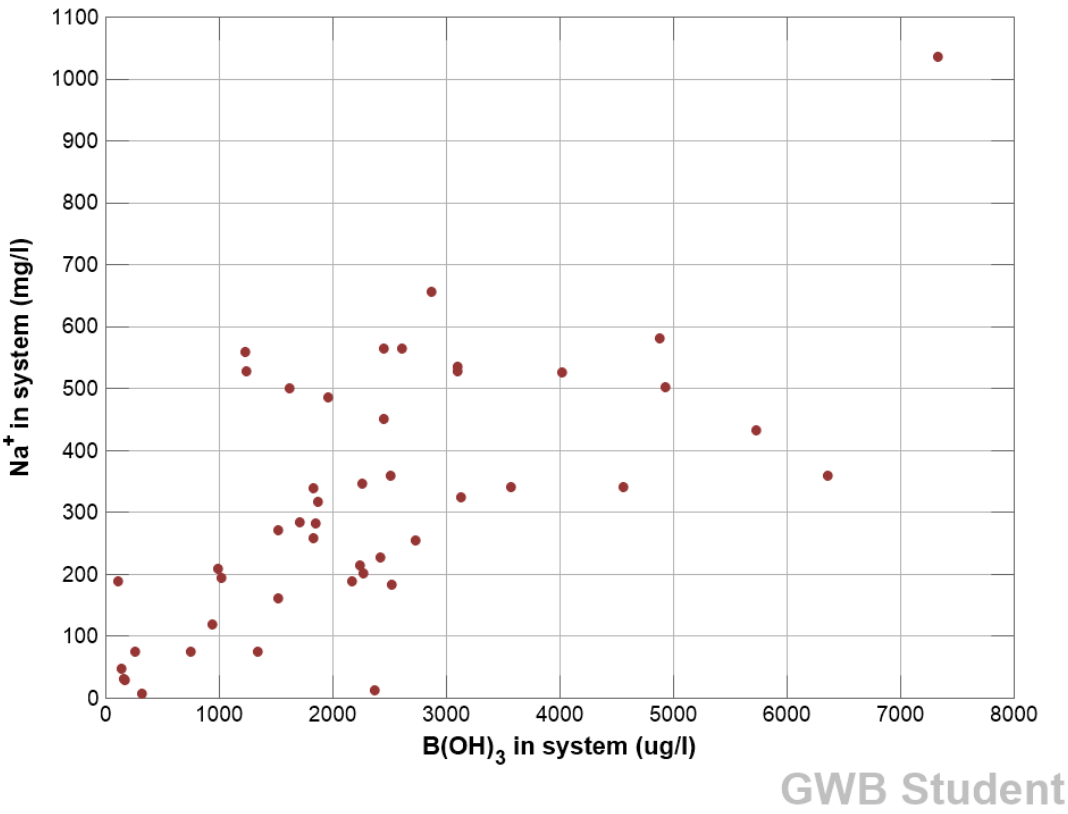

Figure 33: Plot indicating potential positive correlation between B and Na

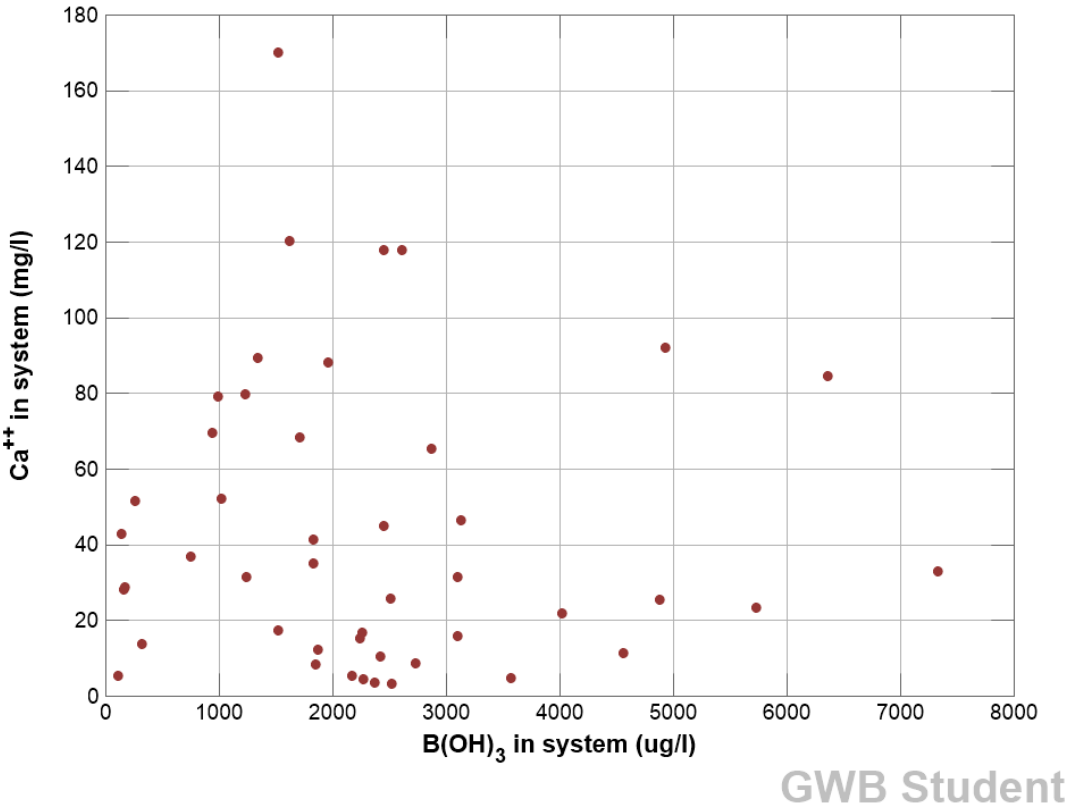

Figure 34: Plot displaying little evidence for direct correlation between B and Ca in solution

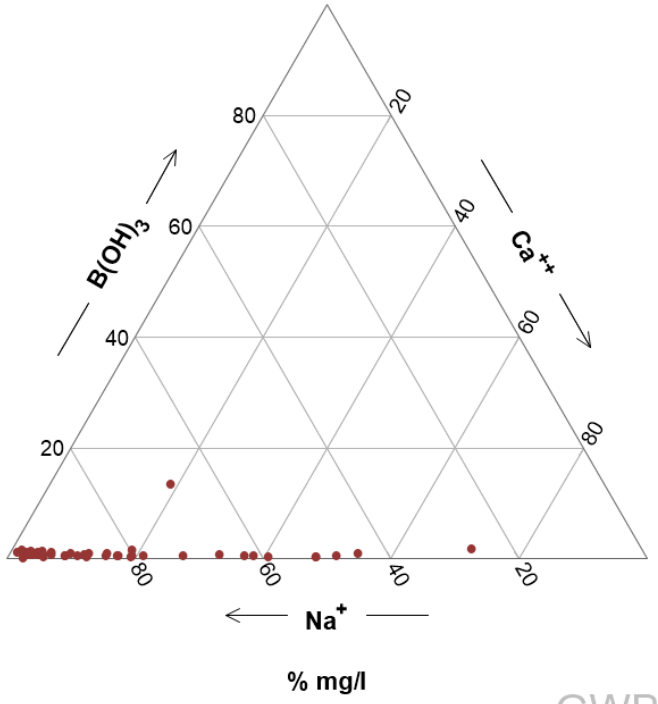

Figure 35: Ternary diagram indicating inverse relationship between the abundance of Ca and Na

Next, geochemical modeling was conducted to determine speciation of boron in solution. Modeling began with generating a piper diagram of the assorted water samples to understand the general geochemistry of the sample suite (**Figure 36**). Then, two speciation diagram series were created to track changing concentrations of boron and calcium chloride (used when creating the adsorption experiments). The first speciation series modeled the variation of the concentration of boron at 10, 25, 50, 100, 200, and 500 ppm B and $CaCl_2$ held at 0.1 M (**Figure 37 A-F**). The dominate species at lower pH was boric acid ($B(OH)_3$) and at higher pH it was $CaB(OH)_4^+$, with

the equilibrium point occurring between pH 7 and 9. The borate ion $B(OH)_4^-$ was also present at higher pH though at only about ~1/6 the abundance of $CaB(OH)_4^+$. Other borate ions were also present, but were insignificant in quantity. The second speciation series modeled the variation of the concentration of $CaCl_2$ in solution at 1 M, 0.5 M, 0.25 M, and 0.1 M with boron concentration held at 200 ppm (**Figure 38 A-D**). While boric acid was again the dominant species at lower pH and $CaB(OH)_4^+$ was the dominate species over $B(OH)_4^-$ at high pH, they began to equalize in concentration at lower $CaCl_2$ levels, with $B(OH)_4^-$ reaching a concentration almost comparable to the calcium borate phase.

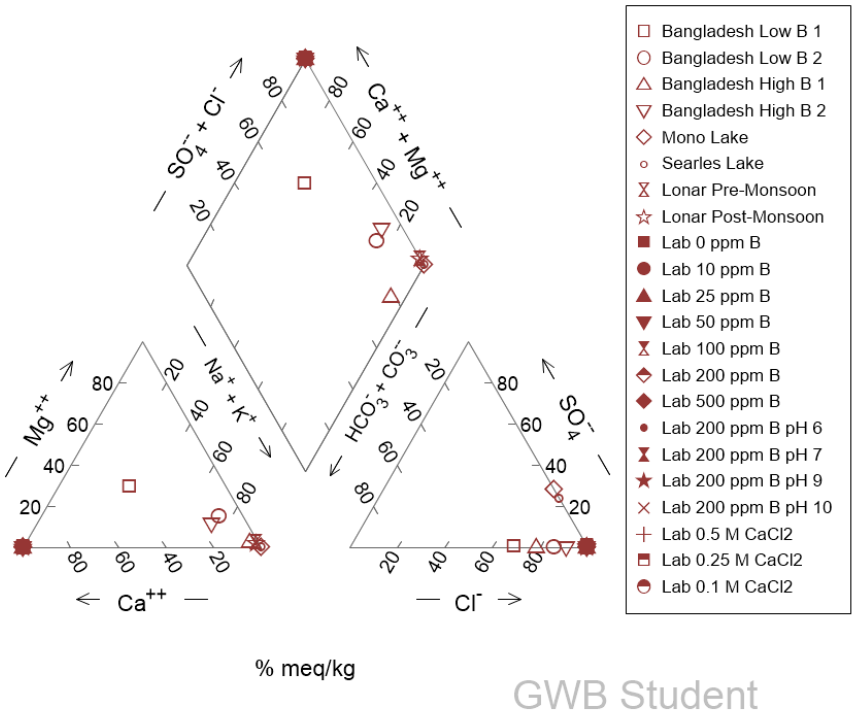

Figure 36: Piper diagram displaying ion chemistry of water samples used for geochemical modeling

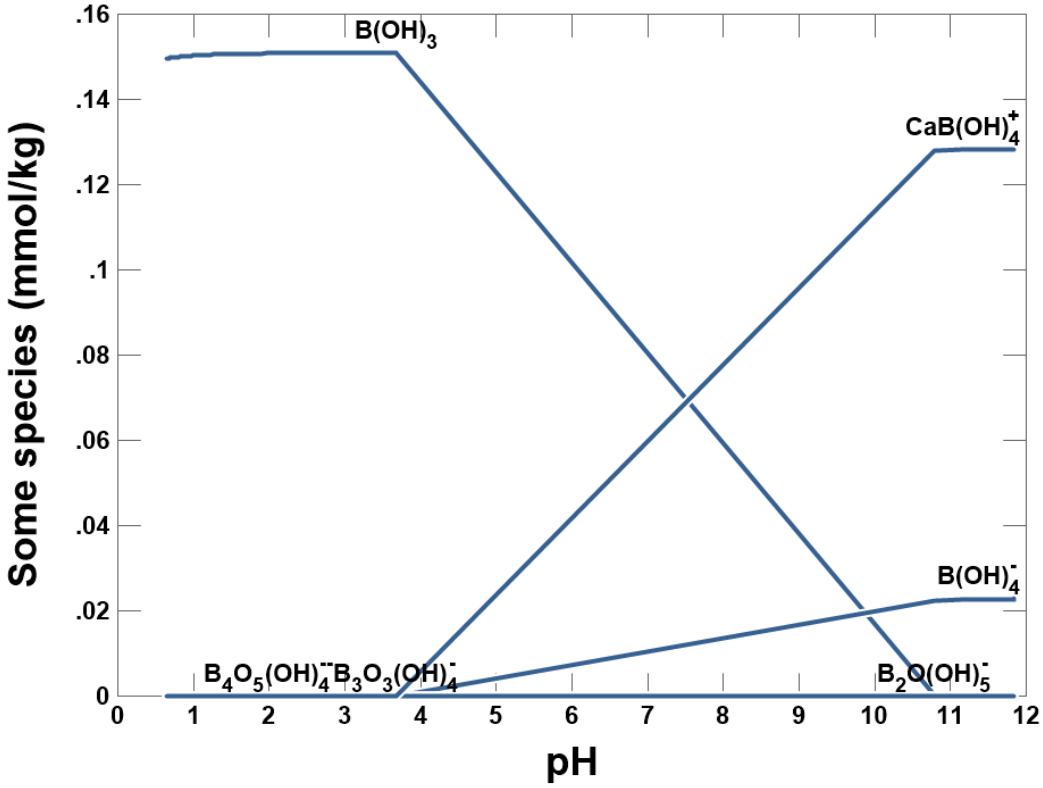

Figure 37: A-F Borate speciation diagrams varying concentration of boron A) The above diagram represents a 10 ppm B solution (Table 4, sample 10). Borate species concentrations are lowest, but boric acid and the calcium borate are the dominant species at low and high pH, respectively.

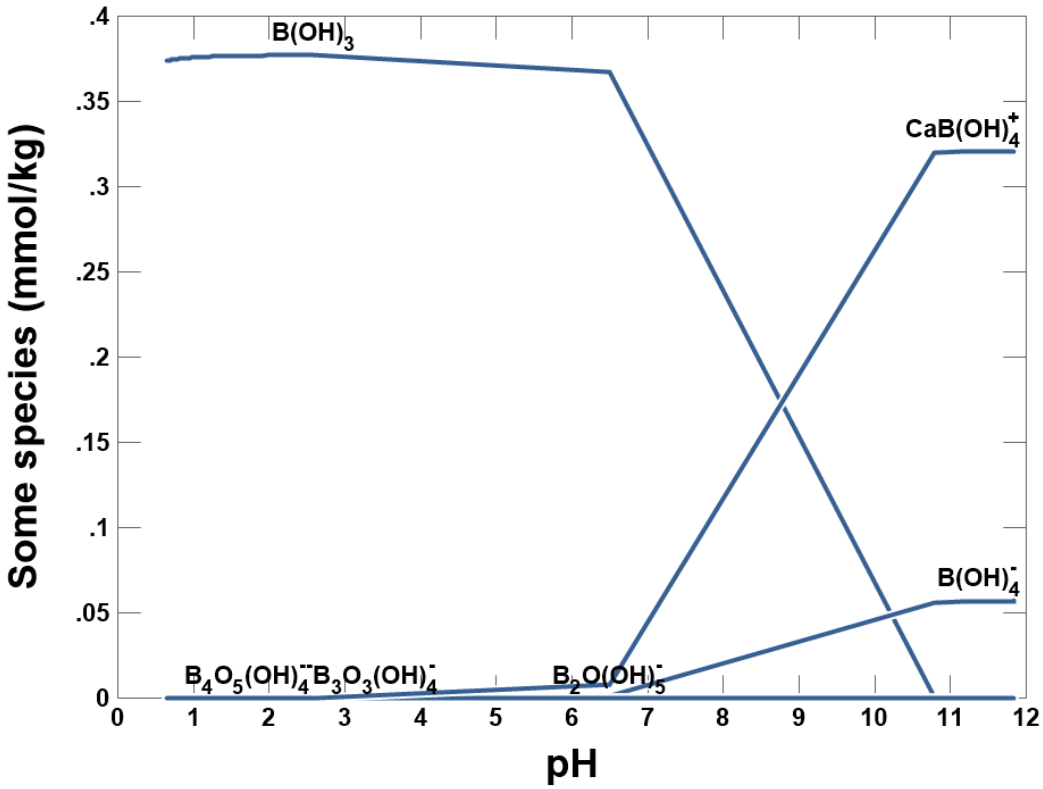

Figure 37B: Borate speciation diagrams varying concentration of boron. The above diagram represents a 25 ppm B solution (Table 4, sample 11). Borate species concentrations are still low, but boric acid and the calcium borate are the dominant species at low and high pH, respectively.

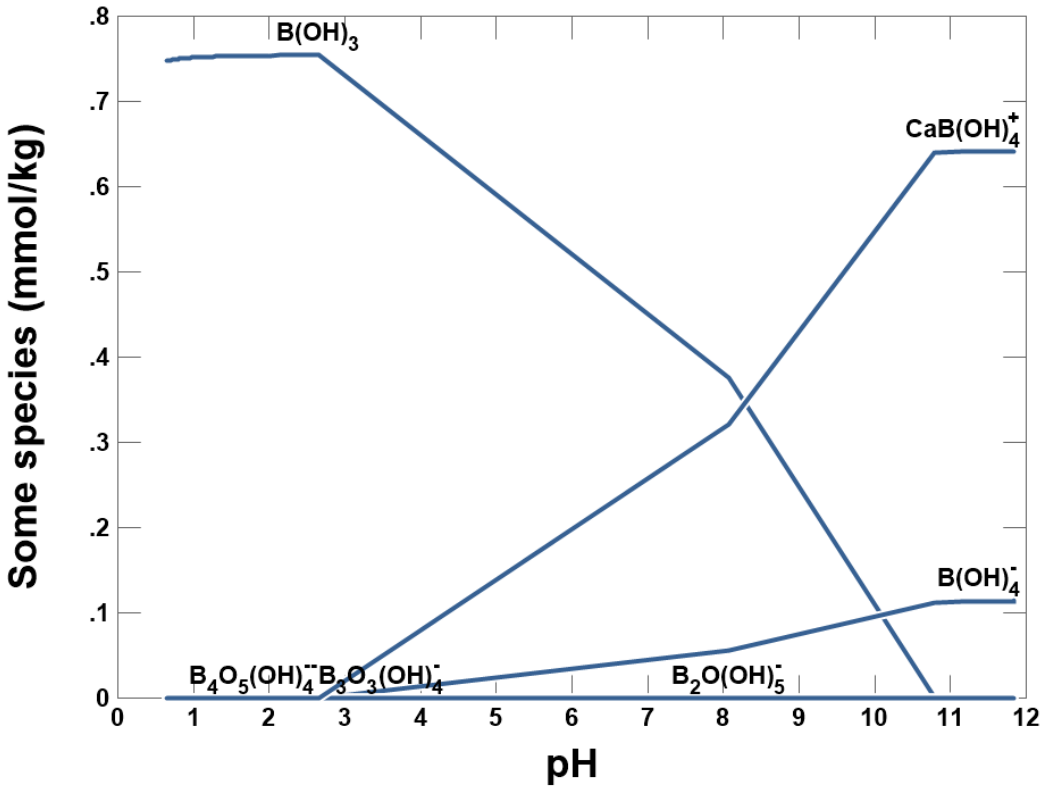

Figure 37C: Borate speciation diagrams varying concentration of boron. The above diagram represents a 50 ppm B solution (Table 4, sample 12). Borate species concentrations are rising, but boric acid and the calcium borate are still the dominant species at low and high pH, respectively.

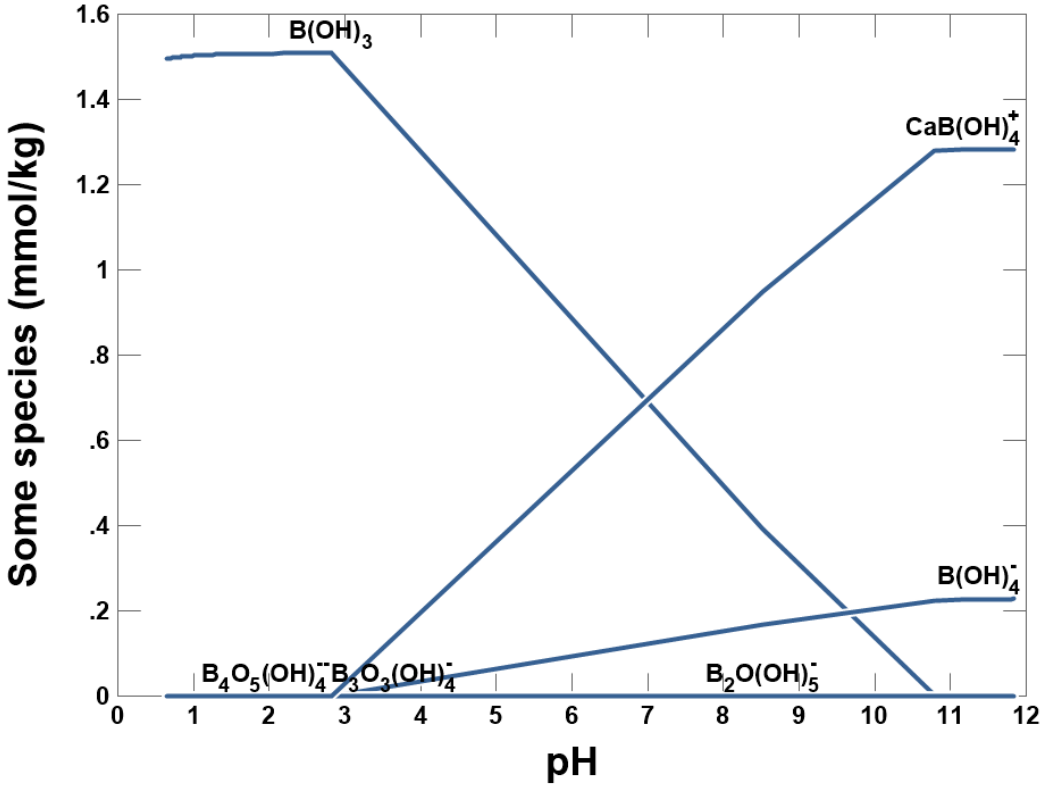

Figure 37D: Borate speciation diagrams varying concentration of boron. The above diagram represents a 100 ppm B solution (Table 4, sample 13). Borate species concentrations are still rising, but boric acid and the calcium borate are still the dominant species at low and high pH, respectively.

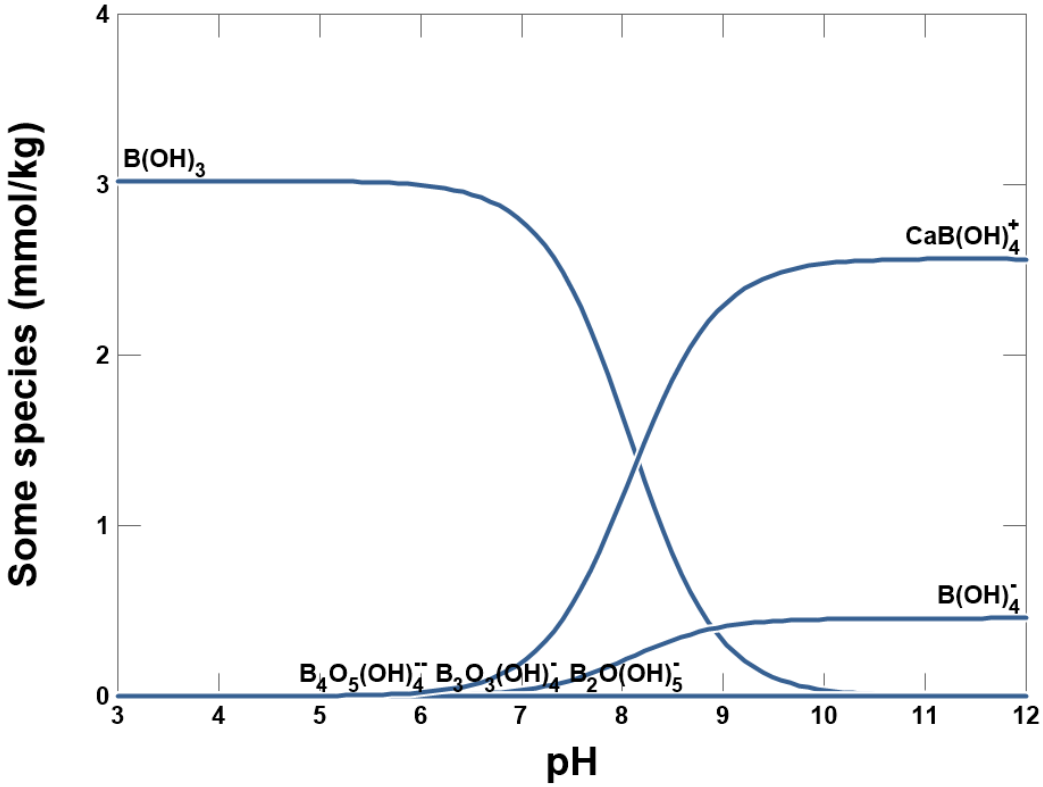

Figure 37E: Borate speciation diagrams varying concentration of boron. The above diagram represents a 200 ppm B solution (Table 4, sample 14). Borate species concentrations are higher, with boric acid and the calcium borate still remaining as the dominant species at low and high pH, respectively.

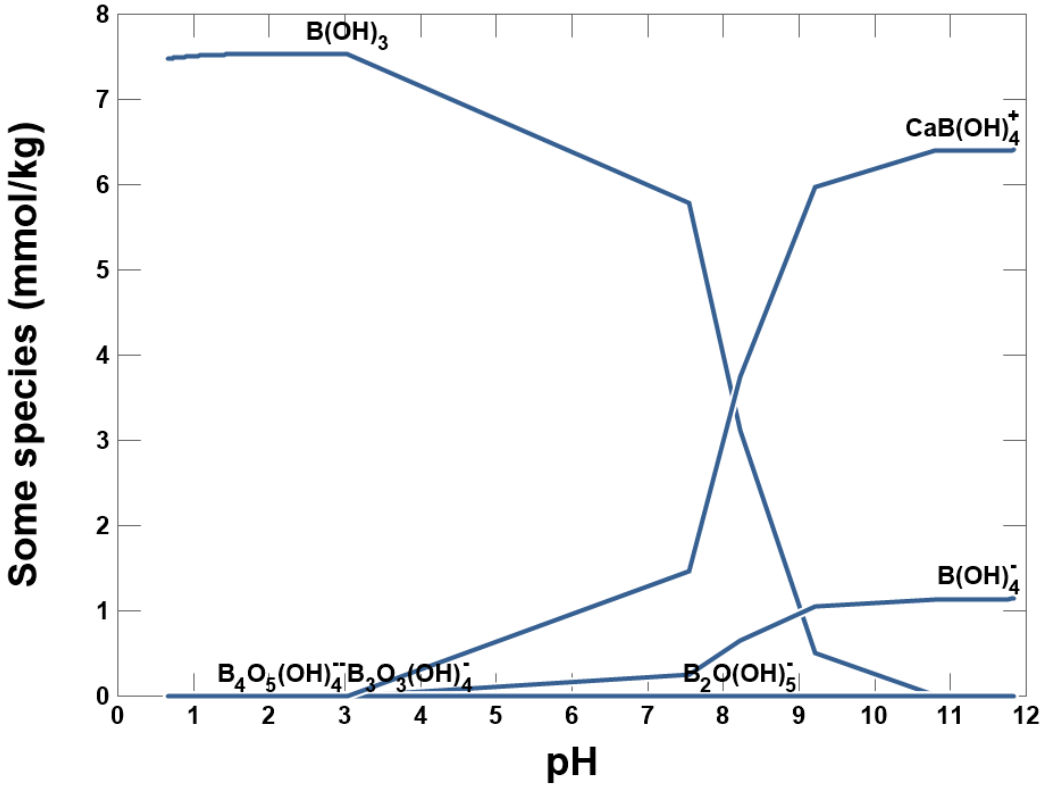

Figure 37F: Borate speciation diagrams varying concentration of boron. The above diagram represents a 500 ppm B solution (Table 4, sample 15). Borate species concentrations are the highest, with boric acid and the calcium borate still being the dominant species at low and high pH, respectively.

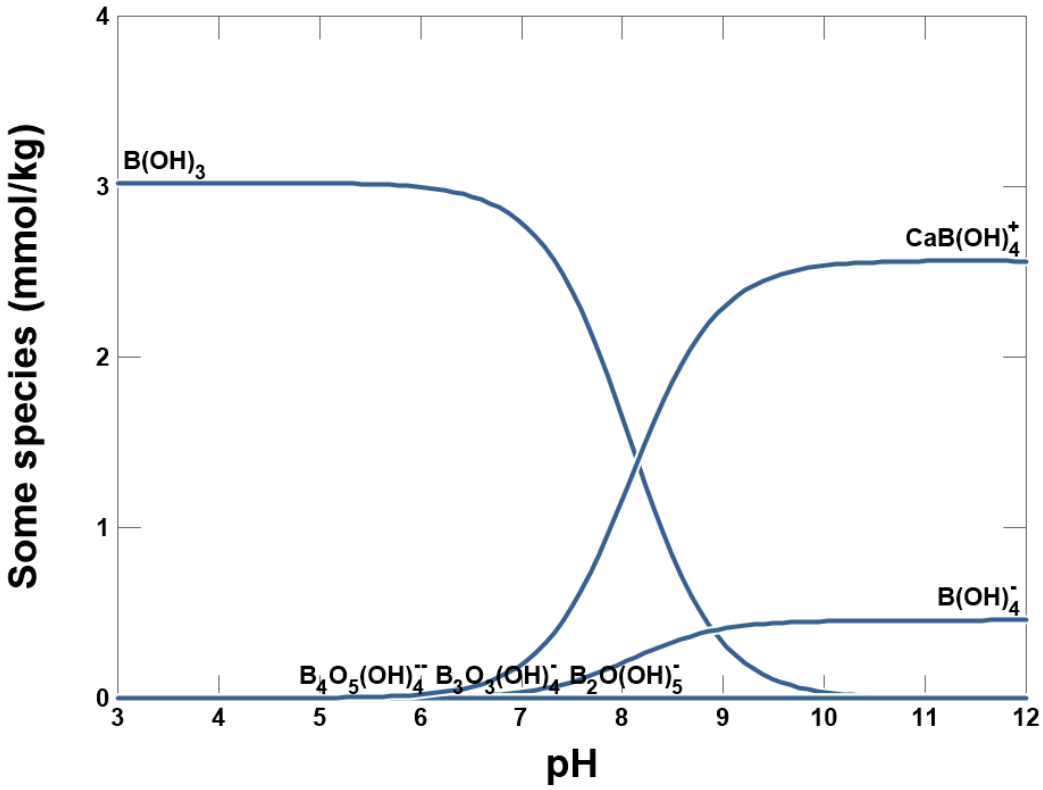

Figure 38 A-D Borate speciation diagrams varying concentration of $CaCl_2$ A) Borate speciation diagram with 1M $CaCl_2$ (Table 4, sample 14), indicating $CaB(OH)_4^+$ as ~5-6 as dominant as $B(OH)_4^-$

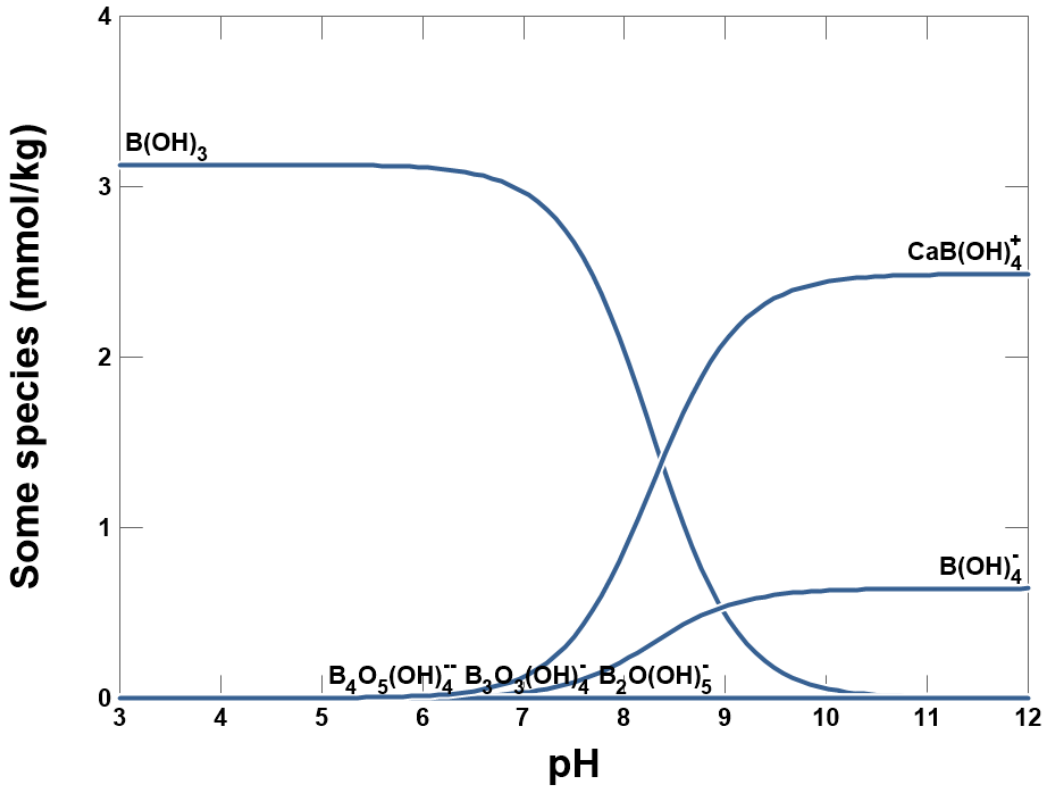

Figure 38B: Borate speciation diagrams varying concentration of $CaCl_2$. Borate speciation diagram with 0.5M $CaCl_2$ (Table 4, sample 20), indicating $CaB(OH)_4^+$ as ~5- as dominant as $B(OH)_4^-$

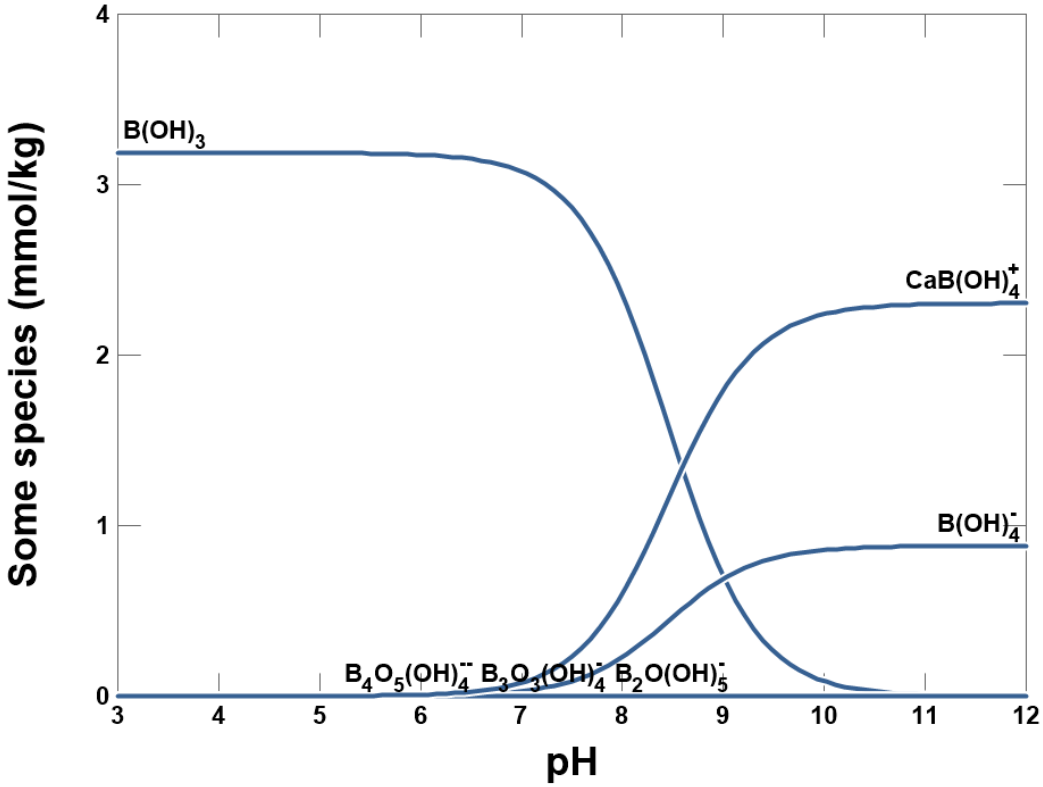

Figure 38C: Borate speciation diagrams varying concentration of $CaCl_2$. Borate speciation diagram with 0.25M $CaCl_2$ (Table 4, sample 21), indicating $CaB(OH)_4^+$ as ~2-3 as dominant as $B(OH)_4^-$

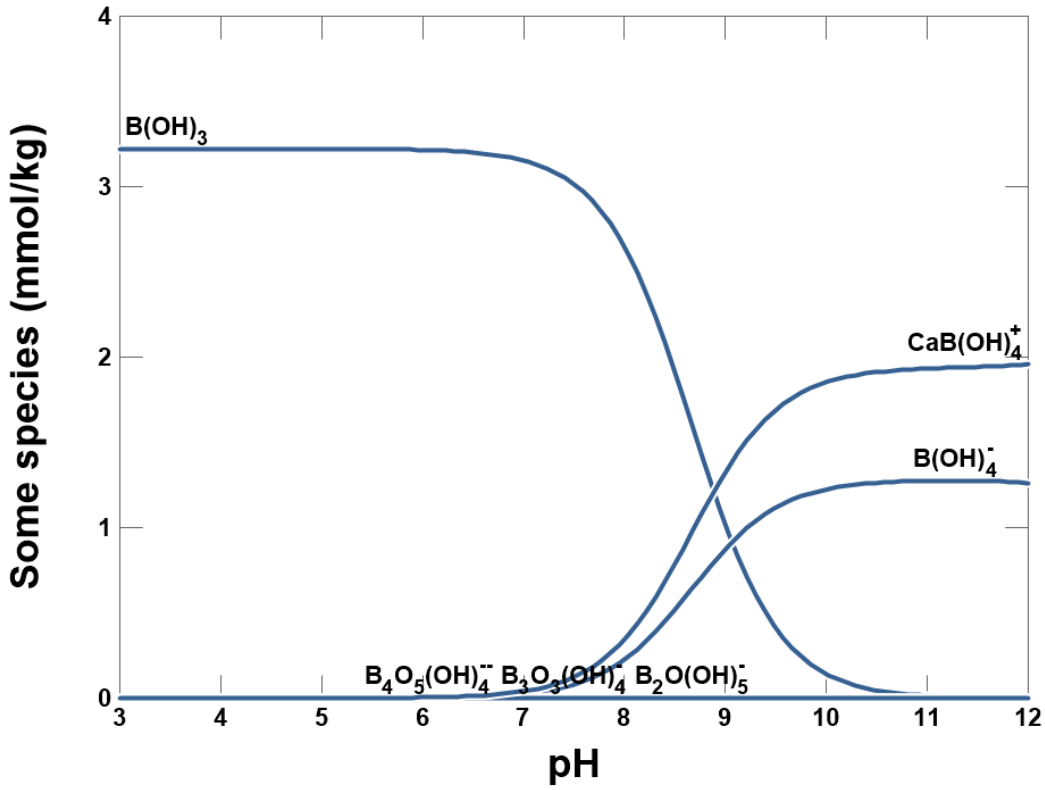

Figure 38D: Borate speciation diagrams varying concentration of $CaCl_2$. Borate speciation diagram with 0.1M $CaCl_2$ (Table 4, sample 22), indicating $CaB(OH)_4^+$ as ~1.5 as dominant as $B(OH)_4^-$

The last speciation model involved comparing water samples from Bangladesh [*Halim et al.*, 2010], Mono Lake [*Domagalski et al.*, 1989], and Searles Lake [*Smith*, 1979] to determine the speciation of boron with some expanded borate species in consideration **(Figure 39**; **Table 12**). The Bangladesh samples, which featured some altered boron concentrations, saw borate speciate almost exclusively as $B(OH)_3$, (boric acid), with trace amounts of the remaining borate species. The Mono Lake sample saw a shift with $B(OH)_4^-$ becoming the most prolific species with ~46% of the boron, followed by ~44% of the boron speciating as $NaB(OH)_4$, with $B(OH)_3$ only accounting for ~8.5% of boron in solution. Searles Lake saw ~76% of the boron speciate as $NaB(OH)_4$, with $B(OH)_4^-$ representing ~20% of boron, and $B(OH)_3$ dropping further to only 2% of boron. Across all five water samples, the remaining six borate species were only present in very trace amounts.

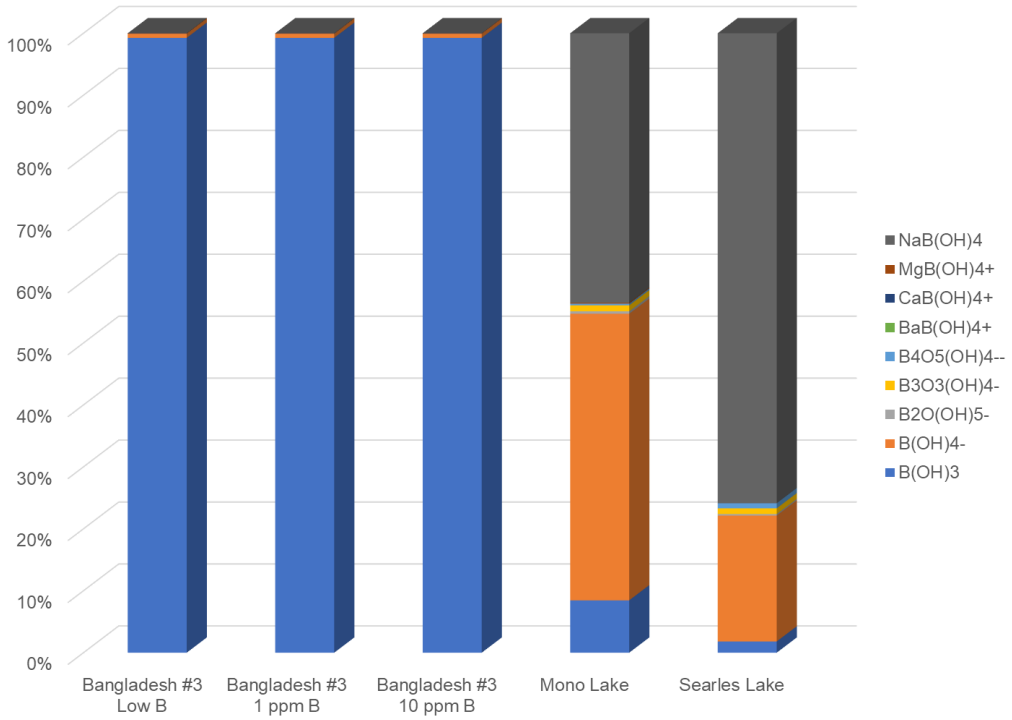

Figure 39: Borate speciation model for natural water samples. Bangladesh samples represent groundwater and therefore speciate as mostly boric acid. Mono Lake and Searles Lake represent saline lakes and therefore boron speciates into borate and sodium borate.

Table 12: Speciation model water samples chemistry and borate species concentrations

Sample ID	Unit	Bangladesh #3 LowB 2	Bangladesh #3 1 ppm B	Bangladesh #3 10 ppm B	Mono Lake	Searles Lake
pH	pH	7	7	7	9.65	9.9
Temperature	C	25	25	25	25	25
HCO3-	mg/l	169.9	169.9	169.9	43200	43200
Cl-	mg/l	599.4	599.4	599.4	11210	98200
SO4--	mg/l	0.96	0.96	0.96	5880	40800
Na+	mg/l	336.8	336.8	336.8	35140	111000
K+	mg/l	8.63	8.63	8.63	1890	17700
Mg++	mg/l	37	37	37	43.7	***0.1***
Ca++	mg/l	41.19	41.19	41.19	5.8	***0.1***
Ba++	ug/l	55.8	55.8	55.8	***1***	***1***
Sr++	ug/l	455.3	455.3	455.3	***1***	***1***
SiO2(aq)	mg/l (as Si)	16.56	16.56	16.56	***1***	33
Fe++	mg/l (as Fe)	0.66	0.66	0.66	***1***	***0.1***
AsO4---	ug/l (as As)	32.8	32.8	32.8	***1***	98000
Mn++	ug/l	81.7	81.7	81.7	***1***	***0.1***
B(OH)3	mg/l (as B)	0.32	***1***	***10***	***1000***	4039
B(OH)3	free mmol/kg	0.02947	0.09211	0.921	7.124	5.373
B(OH)4-	free mmol/kg	1.99E-04	6.21E-04	0.006207	38.99	60.2
B2O(OH)5-	free mmol/kg	4.45E-09	4.35E-08	4.35E-06	0.3326	0.7247
B3O3(OH)4-	free mmol/kg	2.83E-11	8.64E-10	8.64E-07	0.8123	2.749
B4O5(OH)4--	free mmol/kg	1.40E-17	1.34E-15	1.34E-11	0.2309	2.412
BaB(OH)4+	free mmol/kg	1.28E-09	3.99E-09	3.99E-08	8.59E-07	7.74E-07
CaB(OH)4+	free mmol/kg	6.89E-06	2.15E-05	2.15E-04	0.005523	1.63E-04
MgB(OH)4+	free mmol/kg	1.00E-05	3.13E-05	3.13E-04	0.1144	4.69E-04
NaB(OH)4	free mmol/kg	3.81E-06	1.19E-05	1.19E-04	36.67	224.8
Charge imbalance error	percentage	1.92%	1.91%	1.90%	1.10%	2.30%

X values altered to allow model to run when ion not measured. Assumed to be at detection limit

Discussion

XRD Characterization

Given the results provided by the XRD analysis, the clays chosen for Mars analog adsorption should provide strong candidates for good adsorption. Montmorillonite clays have been shown to be strong adsorbers of boron [*Karahan et al.*, 2006; *Keren*, 1981] when exposed to a boron-rich environment. Given the similarities of saponite, nontronite, and griffithite to terrestrial montmorillonites, it is highly likely that they too would be strong adsorbers of boron if presented with similar environmental conditions. While nontronite has dioctahedral coordination, and saponite and griffithite both have trioctahedral coordination, the montmorillonite family of clays contains species of both coordination. Since most montmorillonites are able to adsorb boron regardless of coordination, it is reasonable to assume that both the dioctahedral and trioctahedral species of Mars analog clays would be able to adsorb boron as well. This may indicate that dioctahedral versus trioctahedral coordination does not affect the ability of a clay to adsorb boron, rather that it might affect where the boron is adsorbed and how much is adsorbed.

The XRD analysis also revealed that some of the clay samples, namely the saponite, nontronite, and Rio Tinto samples, were not entirely pure. This can be well applied to the clays seen on Mars as being impure as well [*Vaniman et al.,* 2014]. The clays on Mars are mixed with many other minerals or even a mixture of different clay minerals, and it is therefore very impractical to assume a Martian environment where boron would interact with a singular clay species for adsorption. As the samples used in the study contain minor or trace amounts of other minerals, they reflect a more realistic sample of a clay that would be seen on Earth or on Mars. It can be very helpful to understand how boron will adsorb to clays in the presence of other minerals, as this is the situation that occurs on Mars. In Gale crater, the clay content of the bedrock only averages around ~25-30%

of the rock composition [*Vaniman et al.*, 2014], so this is even more important to know how boron will adsorb to clay minerals when in the presence of other materials.

While the XRD analysis was unable to refine the and identify the exact clay mineral species in the Rio Tinto, griffithite, and saponite samples, it was able to identify a clay mineral species present. XRD analysis detected the distinctive 001 and 060 peaks typically seen amongst phyllosilicate clay minerals. This was a clear indication that there was indeed a phyllosilicate clay present in the sample. The most distinctive diffraction peak for clay minerals is the 001 peak, which for most of the clays was detected at a diffraction angle of 6 2Θ, which translates to a spacing of about ~14.4-14.8 Å. However, the Rio Tinto sample had a 001 diffraction peak of occurring at about 7 2Θ, which translates to a spacing of about 12.6 Å. The Rio Tinto sample 001 peak occurs at a higher diffraction angle due to some difference in the clay, however the difference is small and the peak is still classified as a clay peak. The 060 diffraction peak occurs for phyllosilicate clays occurs around a 2Θ value of around 60-62, of which the Rio Tinto sample falls in the range of at 61. The two trioctahedral clays, the saponite and griffithite, saw their 060 diffraction peaks at a 2Θ angle of ~60 with spacing of 1.535 and 1.537 Å, respectively. The nontronite saw its 060 peak at a 2Θ of ~61 giving a spacing of 1.513 Å. Since the Rio Tinto clay also has the 060 diffraction peak at a 2Θ of ~61, with a spacing of 1.517, it bears a similar diffraction pattern to the dioctahedral nontronite. This may indicate that the clay species within the Rio Tinto sample is also dioctahedral as well, and may help to narrow down the species of phyllosilicate within the sample. The sample will need further treatment and analysis to identify the species of clay present.

The chemical analysis of the Rio Tinto sample run by ActLabs was found to contain boron within it. The analysis indicated that the sample contained over 900 ppm B, which is a significant

amount of boron to be found within the clay. The XRD analysis did not identify any borate minerals within the Rio Tinto sample, although due to the low concentration of boron, any borate mineral abundance would also be low and potentially undetectable via XRD. However, XRD may be able to detect a shift in clay peak position due to potential presence of structural boron, though further analysis is needed to determine this. Another potential situation is that the boron detected via PGNAA by ActLabs is boron that has adsorbed to the clay minerals or other minerals in the sample. If this is the case, this would further indicate that in a boron-rich environment that clay minerals can easily pick up and allow adsorption of boron to their structures. Another possibility is that some or all of the boron is structural boron and formed with the clay. Due to boron's small atomic size, it is extremely difficult and unlikely to determine if the boron is structural using SEM or EPMA, but TEM analysis might be able to detect it. TEM analysis is able to refine structure of very small atomic sizes and would be able to determine if the boron is structurally bound to the clay or adsorbed to the surface.

Experimental Analysis

For the first experimental run, the results indicated that given the conditions of the experiment, a significant initial concentration was needed in order to detect any adsorption onto the clays. The lower concentration sample did not likely see any change in boron because the level was below the detection limits of the ICP-OES, given the test parameters. Given the rougher experimental conditions for this test, as well as the use of borax instead of boric acid for a source of boron, made the degree of boron adsorption less for this experiment. The higher concentration sample had more than enough boron to detect the adsorption from solution. The issues with detecting adsorption at the lower concentrations triggered the attempts to refine adsorption method procedure for the following experiments.

For the second and third set of experiments the results displayed a similar trend when concerning concentration. When initial concentration was decreased, the amount of boron adsorbed to the clay also decreased. In the samples of lower concentration where the clay had potential to adsorb all of the boron out of solution, it did not. This indicates some level of equilibrium state for the boron for how much adsorbs to the clay versus how much remains in solution. This means that boron adsorption concentration may be dependent on the initial fluid concentration. This can be helpful in determining the amount of boron present in a fluid permeating through a rock, if the amount of boron found within the clay or rock is known. This is helpful for application on Mars, as the water-rock fluids have likely long disappeared and the only remaining record of boron is what can be detected in the lithology. It may therefore be possible to predict the boron concentration in the ancient groundwater of Gale crater. This can be done by calculation of the K_d value to determine initial fluid concentration. The K_d calculations in this study showed that K_d increased with increased pH. Since K_d represents the ratio of ion adsorbed to a solid vs ion left in solution, this indicates the clays in this study adsorbed a greater proportion of boron at higher pH than at lower pH. This further provides evidence of more alkaline pH waters favoring borate adsorption.

Understanding the ancient groundwater is important for understanding the past environment on Mars within Gale crater. The presence of borates, either as evaporates or found within other minerals, further indicate an environment that was a lacustrine paleolake environment that eventually dried out over time. Evaporates are typically an indicator of a paleolake setting, however different evaporate minerals indicate different characteristics or about the conditions of the lake when the evaporates formed. Certain chloride salts, such as sodium chloride or potassium chloride, are often some of the first evaporates to precipitate in a drying environment. Due to the

abundance of sodium and potassium in both rock and water settings, these salts also tend to be the most abundant evaporates found in traditional paleolake settings. The presence of borate evaporates, such as those seen in Death Valley, tends to reflect a lacustrine environment that has been drying out for some time as the "early" precipitates such as sodium chloride have already precipitated and the borates represent the remaining salts still left in the paleolake. Borate may also shed some light on the likely range of pH of the lake at the time based on the speciation of boron found. In general, the presence of boron tends to reflect a higher paleosalinity, although this can be further explored by analysis of the species of adsorbed boron present on mineral surfaces. If the boron that adsorbs to clays is found present in the form of predominantly borate or boric acid, it would indicate a water pH of ~8 or lower as boric acid is the speciation of boron at this pH range. If the predominant adsorbed boron species is borate then this would indicate that the pH conditions of the water were likely ~8 or above. Borates can be helpful paleosalinity indicators by both the abundance of their presence and the form of boron which is present.

For the experiments concerning time effect on adsorption, there was no difference in the amount of adsorption between the 10 hour and 20 hour samples. This means that the reaction removing boron from solution and adsorbing it to the clay samples occurs relatively quickly, thus beyond 10 hours, no more significant boron was adsorbed by the clay. Adsorption is typically assumed to occur fairly quickly, so this test reaffirms this assumption. Adsorption occurring quickly may be due to the reaction occurring as an equilibrium reaction process, with the system trying to reach a point of stable equilibrium as quickly as possible. As mentioned prior, not all of the boron available adsorbs to the surface of the clay and some remains in solution. Despite the different samples were created with different concentrations of boron, they all contained 1 g of clay material. The 200 ppm B sample was able to adsorb ~40 μmol B onto the 1 g of

montmorillonite B clay, while the 100 ppm B sample only adsorbed ~16 μmol B onto 1 g of the same clay. At 100 ppm B, the sample had enough boron in solution to adsorb 40 μmol B like the 200 ppm B sample, but it didn't and 16 μmol B is not the threshold for saturation for the clay as the 200 ppm B sample was able to adsorb 40 μmol B at the same amount of clay. This indicates the boron is forming some sense of equilibrium between how much boron is adsorbed on the clay and how much remains in solution. In this case, as the system is trying to reach equilibrium, it will try to balance the system as quickly as possible and therefore adsorption likely happens fairly quickly. Different species of clays may reflect different states of equilibrium with boron as can be seen by the comparison of the two montmorillonites in **Figure 18**, with the two montmorillonites where the correlation between initial boron concentration compared with boron adsorbed is comparable at lower concentrations but begins to deviate at higher concentrations. Once more clays are added to the adsorption series, further analysis can determine the extent to which clay species affects boron equilibrium.

For the experiments concerning the effect of pH on boron adsorption, the results of this study reflected mixed results compared to that which has been seen in the literature. The amount of boron adsorbed to the clays was much higher in this study: this is attributed to this study's experiments having a much higher initial liquid concentration. Prior studies on boron adsorption to clays constrained boron fluid concentrations in the ranges of 1 ppm B up to 50 ppm B [*Karahan et al.*, 2006; *Keren*, 1981; *Couch*, 1968; *Goldberg*, 1997], whereas for this experiment the range of boron concentration in the fluid ranged from 10 ppm up to 200 ppm. As the concentration analysis indicated that boron adsorption increases with increased fluid concentration (**Figure 18**), this, in addition to variability between clay species, may indicate why the results of this analysis yielded boron adsorption values much higher than seen in past literature. More studies are needed to look

at the species in solution with geochemical modeling to address the differences between this study and previous literature results.

Furthermore, the expected peak pattern of the adsorption peak at pH 8 was not seen in one of the montmorillonites (B) while it was seen in the other (A). Montmorillonite B instead saw peak adsorption at pH 11 with decreasing adsorption with declining pH. This difference in peak adsorption conditions between clays, even similar species, could indicate that adsorption is highly dependent on the chemical makeup or structure of the specific clay species, resulting in high variability of adsorption behavior. There is some evidence pointing that phyllosilicate clays with elevated amounts of iron display peak adsorption at higher pH ranges, around 10-11 [*Goldberg et al.*, 1993]. If this is the case, then peak adsorption may be able to fluctuate easily based on differences in chemical composition and structure. It may then be feasible that the species of montmorillonites used in this analysis, while low in Fe, may have some characteristic that shifts the peak adsorption to higher pH. If peak adsorption for these montmorillonites was higher and around pH 10 instead of pH 8, then this could explain the lack of the expected adsorption curve as well. As the parameters for this experiment had a max pH of 10, the expected drop in adsorption potential seen after the peak adsorption would not be seen like in the literature and the results would only indicate steady increase in adsorption potential.

Geochemical Modeling

The model analysis determined that boron activity in water was affected by several different other ions in solution. The amount of boron in the water samples varied from ~0.3 ppm upwards to 1.2 ppm, while the waters were heavily concentrated in carbonates, chlorine, and alkali metals. While the carbonates and chlorine did not appear to have an effect on the boron in solution the alkali metals did appear to. There appeared to be a positive correlation between Na^+ and B (as

$B(OH)_3$) when in solution, so as more Na was dissolved in solution, more B was also able to be dissolved as well. When directly comparing the Ca^{2+} and B, there did not appear to be a direct or clear enough correlation to relate these two elements when in solution, as the data was rather scattered though there was a relationship when in terms of mineral speciation.

The boron speciation modeling (**Figure 37-38**) revealed that boron would appears as boric acid in low pH and as a borate anion in higher pH. The borate anion can vary in species and abundance depending on what else is in solution. Varying the concentration of boron in the initial fluid did not significantly change the speciation of boron, as it almost always appears as $CaB(OH)_4^+$ at 6 to 7 times the concentration of $B(OH)_4^-$ when the $CaCl_2$ is at 1 M concentration. The abundant concentration of Ca in solution from the $CaCl_2$ drastically affects the borate species at high pH into appearing as a calcium-borate anion, rather than a purely borate anion. As the concentration of the $CaCl_2$ solution is decreased, the ratio between the two species begins to decrease and the $B(OH)_4^-$ borate species becomes almost as prevalent as the calcium-bearing phase. Given that calcium clearly has a strong effect on the speciation of borate in solution, it may also have strong implications on the adsorption capability of boron onto clays, however further adsorption modeling is needed to determine the possibility. This was further corroborated by the natural water modeling (**Figure 39**) of the Bangladesh, Mono, and Searles waters. The Bangladesh waters represent groundwater samples and therefore speciated almost exclusively as boric acid, with only trace amounts of any other borate species. The Mono and Searles waters come from much more alkaline and evaporated lakes and therefore have an abundance of dissolved cations in solution. This caused boron to speciate into borate species over boric acid due to the shift in alkalinity of the water and additionally allowed the abundance of a sodium-borate species. This may have strong implications for adsorption as sodium borate is charge neutral and therefore less inclined to adsorb to a clay

surface like a borate anion or calcium borate cation. The amount of Ca or Na in solution greatly affects the speciation of boron and may therefore affect its ability to adsorb to clays.

In relation to Mars, these analyses are important for understanding which ions affect boron in solution as well as understanding the potential speciation of borate minerals given these conditions. As Na, Ca, and Mg are all common rock-forming elements, they are also abundant on Mars within Gale Crater, and would provide some of the necessary materials needed to form borate minerals. As boron has so far been detected within calcium sulfate veins, it may prove that boron is dependent on the calcium in Gale bedrock for either precipitation or adsorption. If increased calcium content facilitates greater formation of borate minerals, this has strong implications for boron adsorption and mineralization being a major process in Gale crater due to the abundance of calcium there. The detected concentration of boron on Mars is in fact higher than what was seen in these water samples, so this would make it easier in the Martian setting to create borates, or allow for borate adsorption, given the excess of boron in solution. As boron is currently not possible to detect in the regular bedrock due to the high Fe content, it can be helpful to know the concentrations of other mobile elements in the system to help estimate what the potential concentration of boron may be. As boron has so far been detected within calcium-sulfate veins, this could help to understand what species of borate minerals may be present given the known chemistry of the ancient Martian groundwater, as well as a better understanding of the water chemistry itself. Given the significant quantity of dissolved Ca, it is highly possible for either colemanite or hydroboracite to be potential borate minerals to have formed in the Martian lithology.

Future Work

Further experiments will produce an array of terrestrial and Mars analog clay standards treated with borate at a series of pH values, ranging from 6 to 11. Running the samples at a wide range of pH will allow better understanding of the correlation between boron adsorption and pH. Literature experiments indicate an increase in boron adsorption at neutral to basic pH with a peak around 8-9, and then a decline in adsorption into higher pH range. This experimental range will provide the optimal pH for boron adsorption for typical Martian clay minerals. These experiments displayed different trends with lower adsorption at low pH with a steady increase with increased pH.

Additional analysis of the clays will also include more XRD analysis in order to understand the mineralogic structure of each of the clays used. This will assist in the analysis of boron adsorption to clays as well as how mineralogic differences affect the effectiveness in adsorbing boron. It is important to have a general understanding of each of the clays structural and chemical differences as these variances can have impacts on how much boron is adsorbed as well how it is adsorbed. The next round of XRD analysis will include oriented mounts in order to get a better grasp on mineralogic makeup of the clay species being used. There will also be attempts to run analysis of some of the boron-enriched clays through TEM (Transmission Electron Microscope) analysis in order to get an even clearer picture of the nature of boron adsorption to the clays.

It is hypothesized that the boron adsorbs to the outer surfaces of clays as well potentially into the interlayer spacing between the outer tetrahedral layers in the clays. The outer surfaces and interlayer spacing provide the most ideal location for there to be available charge for adsorption as well as the most ideal sites for cation exchange [*Drever*, 1997]. This is the motivation and need for XRD analysis of the clays post-adsorption in addition to the pre-adsorption analysis.

Comparing the XRD analysis of the clays before and after adsorption allows for comparison of the clays structure to understand how the addition of boron changes it. If boron is limited to adsorbing to the outside of the clay, then the XRD analysis will pick up the standard clay structure will additional borate attached to the outside, whereas if the boron adsorbs into the interlayer positions, the XRD analysis will be able to detect a change in the interlayer spacing. TEM analysis can provide stronger analysis to pinpoint the exact location of the adsorbed boron on the clays to help further verify this.

This study has prepared the way to generate a series of clays enriched with 100-300 ppm of borate that will be used to improve the ChemCam calibration for targets on Mars. It is predicted the saponite and nontronite samples to adsorb boron in significant values similar to those seen by montmorillonite and bentonite from previous studies and from this studies' experiments. If saponite and nontronite adsorb boron in significant quantities, this will provide insight and knowledge into where boron is housed on Mars outside of calcium-sulfate veins. If boron is therefore able to effectively adsorb onto Martian-like soils, this makes the case for boron-ribose facilitated prebiotic conditions on Mars more viable. Further experiments will be carried out (in related MSL research) by reacting these borate-bearing clay standards with ribose by [*Ricardo et al.*, 2004].

Further analyses will be conducted at Los Alamos National Laboratory (LANL). Some techniques used there will include Laser Induced Breakdown Spectroscopy (LIBS), the method used by ChemCam that detected boron, as well as with Raman Spectroscopy, Nuclear Magnetic Resonance (NMR) spectroscopy, and Gas Chromatography-Mass Spectrometry (GCMS). LIBS spectra collected with the ChemCam engineering unit at LANL can be directly compared with ChemCam on *Curiosity*. Thus, these spectra can be added to the set of standard boron calibration

spectra and improve the quantification of boron in ChemCam Mars data. XRD and Raman will provide mineralogical analysis, NMR will provide organic structural analysis, and GCMS will provide the organic concentration and identification analysis. The organic chemical fraction of these clays will also be analyzed with GCMS [*Gasda et al.*, 2019]. NMR and GCMS will be used for analyzing the ribose-borate interaction in an associated study by LANL to determine boron's feasibility for stabilizing organic materials, like ribose, in a Martian setting. NMR is frequently used for the analysis of organic structures due to its high degree of accuracy in identifying molecular structures. GCMS is a well-established method for identifying materials and measuring their concentration. These methods will characterize these samples and be used for comparison with the current *Curiosity* rover and the future Mars 2020 rover datasets.

Conclusions

In conclusion, understanding borate adsorption onto clays is important for understanding boron on Mars. Boron adsorbs easily to phyllosilicate clays and this is assumed to be of the same case on Mars. XRD analysis indicates that the clays chosen as Mars analogs for adsorption analysis should prove to be excellent candidates for boron adsorption based on structures and additionally how their impurity can be useful for comparing with Mars environments. Adsorption analysis indicated a link between initial boron concentration and boron adsorption concentration showing positive correlation between the two. While adsorption curves did not match expected previous trends from the literature, differences in clay species and boron concentration may have contributed to these different results, although further experimentation with Mars-analog samples is required for confirmation. Boron adsorption to Mars-like clays is expected to be comparable to terrestrial clays, with further experimental analysis looking to validate this.

This study represents the first boron-clay adsorption experiments for Mars-like clays, which will provide new insight on the geochemical behavior of borate in Martian groundwater and allow inference into the amount of boron that could be present in Martian bedrock. Understanding boron-clay relationships will allow better comparisons between terrestrial and Martian boron-enriched clays and improve techniques for boron detection on Mars. Boron-clay relationships will form the basis for later work on the impact of boron-enriched clays on prebiotic processes on Mars [*Ricardo et al.*, 2004]. Evidence supports there being multiple diagenetic episodes [*Grotzinger et al.*, 2014] on Mars and boron may provide clues to the timing and origin of groundwater activity on Mars and how this relates to habitability in Gale crater. MSL has been exploring the clay unit in Gale Crater (see **Figure 40**), which has been seen from orbit to be abundant in phyllosilicate clay minerals [*Milliken et al.*, 2010], so this research will be very applicable to being able to understand if the rover's current location may contain abundant boron and therefore have strong potential for prebiotic conditions and habitability.

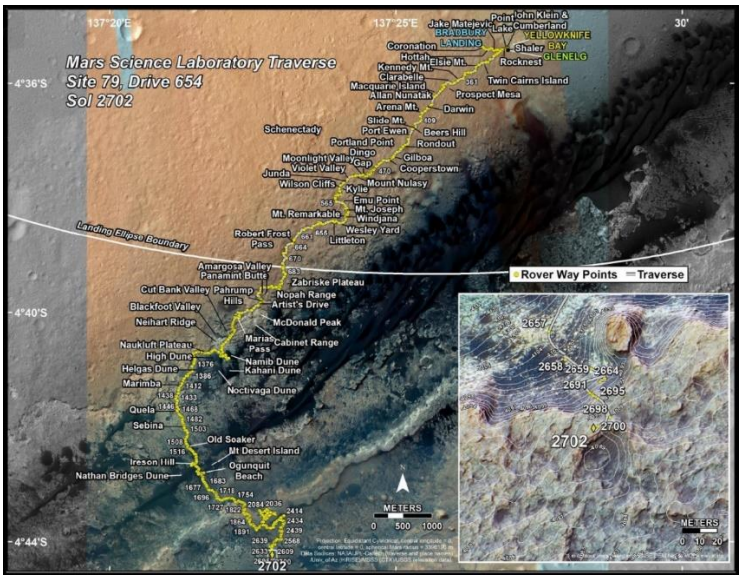

Figure 40: MSL traverse along with some of the future planned traverse. The rover has been traversing what has been called the clay unit, as spectroscopically seen from orbit. As this unit is supposed to be rich in clay minerals, this unit could be of high interest in searching for boron as well as learning about the clay mineral lithology in Gale Crater.

References:

Ayawei, N., Ebelegi, A.N., and Wankasi, D., 2017, Modelling and Interpretation of Adsorption Isotherms: Journal of Chemistry, v. 2017, p. 1–11, doi: 10.1155/2017/3039817.

Becker, S., Feldmann, J., Wiedemann, S., Okamura, H., Schneider, C., Iwan, K., et al., 2019, Unified prebiotically plausible synthesis of pyrimidine and purine RNA ribonucleotides. *Science*, *366*(6461), 76–82. https://doi.org/10.1126/science.aax2747

Bernhardt, H., Williams, D.A., and Hiesinger, H., 2018, Neukum crater and surrounding eastern Noachis Terra: Integrated local and regional photogeologic mapping of Mars' ancient highlands: American Geophysical Union, abstract #P53F-3029.

Bethke, C.M., 2011, Geochemical and biogeochemical reaction modeling: New York, Cambridge University Press.

Birkeland, P.W., 1999, Soils and geomorphology: New York, Oxford University Press.

Bristow, T. F., Bish, D. L., Vaniman, D. T., Morris, R. V., Blake, D. F., Grotzinger, J. P., et al., 2015, The origin and implications of clay minerals from Yellowknife Bay, Gale crater, Mars. *American Mineralogist*, *100*(4), 824–836. https://doi.org/10.2138/am-2015-5077CCBYNCND

Bristow, T.F., Rampe, E.B., Achilles, C.N., Blake, D.F., Chipera, S.J., Craig, P., Crisp, J.A., Marais, D.J.D., Downs, R.T., Gellert, R., Grotzinger, J.P., Gupta, S., Hazen, R.M., Horgan, B., et al., 2018, Clay mineral diversity and abundance in sedimentary rocks of Gale crater, Mars: Science Advances, v. 4, doi: 10.1126/sciadv.aar3330.

Cafferty, B.J., Hud, N.V., 2014. Abiotic synthesis of RNA in water: a common goal of prebiotic chemistry and bottom-up synthetic biology. Current Opinion in Chemical Biology 22, 146–157. doi:10.1016/j.cbpa.2014.09.015.

Chapelle, S., & Verchere, J.-F., 1988, A 11B and 13C NMR determination of the structures of borate complexes of pentoses and related sugars. *Tetrahedron*, *44*(14), 4469–4482. https://doi.org/10.1016/S0040-4020(01)86149-4

Chaussidon, M., and Jambon, A., 1994, Boron content and isotopic composition of oceanic basalts: Geochemical and cosmochemical implications: Earth and Planetary Science Letters, v. 121, p. 277–291, doi: 10.1016/0012-821x(94)90073-6.

Chen, W.-T., Ho, S.-B., and Lee, D.-Y., 2009, Effect of pH on Boron Adsorption-Desorption Hysteresis of Soils: Soil Science, v. 174, p. 330–338, doi: 10.1097/ss.0b013e3181a7e72e.

Clegg, S.M., Wiens, R.C., Anderson, R., Forni, O., Frydenvang, J., Lasue, J., Cousin, A., Payré, V., Boucher, T., Dyar, M.D., Mclennan, S.M., Morris, R.V., Graff, T.G., Mertzman, S.A., et al., 2017, Recalibration of the Mars Science Laboratory ChemCam instrument with an expanded geochemical database: Spectrochimica Acta Part B: Atomic Spectroscopy, v. 129, p. 64–85, doi: 10.1016/j.sab.2016.12.003.

Couch, E.L., 1968. Boron Fixation by Illites. Clays and Clay Minerals 16, 249–256. doi:10.1346/ccmn.1968.0160307.

Cousin, A., Sautter, V., Payré, V., Forni, O., Mangold, N., Gasnault, O., Deit, L.L., Johnson, J., Maurice, S., Salvatore, M., Wiens, R.C., Gasda, P., and Rapin, W., 2017, Classification of igneous rocks analyzed by ChemCam at Gale crater, Mars: Icarus, v. 288, p. 265–283, doi: 10.1016/j.icarus.2017.01.014.

Crowley, J.K., 1993, Mapping playa evaporite minerals with AVIRIS data: A first report from Death Valley, California: Remote Sensing of Environment, v. 44, p. 337–356, doi: 10.1016/0034-4257(93)90025-s.

Das, D., Gasda, P.J., Wiens, R.C., Leveille, R.J., Berlo, K., 2019, Measurement of boron in Gale Crater near Vera Rubin Ridge: Houston, Texas, Lunar & Planetary Institute, Lunar and Planetary Science L, abstract 2132.

Das, D., 2020, Boron and Lithium in Calcium Sulfate Veins: Tracking Precipitation of Diagenetic Materials in Vera Rubin Ridge, Gale Crater, Journal of Geophysical Research: Planets, in press.

Domagalski, J.L., Orem, W.H., and Eugster, H.P., 1989, Organic geochemistry and brine composition in Great Salt, Mono, and Walker Lakes: Geochimica et Cosmochimica Acta, v. 53, p. 2857–2872, doi: 10.1016/0016-7037(89)90163-4.

Dravite, Dravite: Mineral information, data and localities., https://www.mindat.org/min-1318.html (accessed December 2019).

Drever, J.I., 1997, *The geochemistry of natural waters*: New Jersey, Prentice Hall, 436 p.

Ehlmann, B. L., & Buz, J., 2015, Mineralogy and fluvial history of the watersheds of Gale, Knobel, and Sharp craters: A regional context for the Mars Science Laboratory Curiosity's exploration: Gale-Knobel-Sharp Watershed. *Geophysical Research Letters*, *42*(2), 264–273. https://doi.org/10.1002/2014GL062553

EPA, Understanding Variation In Partition Coefficient, Kd, Values. (1999). *United States Environmental Protection Agency*.

Fraeman, A.A., Ehlmann, B.L., Arvidson, R.E., Edwards, C.S., Grotzinger, J.P., Milliken, R.E., Quinn, D.P., and Rice, M.S., 2016, The stratigraphy and evolution of lower Mount Sharp from spectral, morphological, and thermophysical orbital data sets: Journal of Geophysical Research: Planets, v. 121, p. 1713–1736, doi: 10.1002/2016je005095.

Fleet, M. E. L., 1965, Preliminary investigations into the sorption of boron by clay minerals. *Clay Minerals*, *6*(3).

Frydenvang, J., Gasda, P.J., Hurowitz, J.A., Grotzinger, J.P., Wiens, R.C., Newsom, H.E., Edgett, K.S., Watkins, J., Bridges, J.C., Maurice, S., Fisk, M.R., Johnson, J.R., Rapin, W.,

Stein, N.T., et al., 2017, Diagenetic silica enrichment and late-stage groundwater activity in Gale crater, Mars: Geophysical Research Letters, v. 44, p. 4716–4724.

Furukawa, Y., Horiuchi, M., & Kakegawa, T., 2013, Selective Stabilization of Ribose by Borate. *Origins of Life and Evolution of Biospheres*, *43*(4–5), 353–361. https://doi.org/10.1007/s11084-013-9350-5

Furukawa, Y., & Kakegawa, T., 2017, Borate and the Origin of RNA: A model for the Precursors to Life. *Elements*, *13*, 261–265. https://doi.org/10.2138/gselements.13.4.261

Gasda, P.J., Haldeman, E.B., Wiens, R.C., Rapin, W., Bristow, T.F., Bridges, J.C., Schwenzer, S.P., Clark, B., Herkenhoff, K., Frydenvang, J., Lanza, N.L., Maurice, S., Clegg, S., Delapp, D.M., Sanford, V.L., Bodine, M.R., Mcinroy, R., 2017. In situ detection of boron by ChemCam on Mars. Geophysical Research Letters 44, 8739–8748. Doi:10.1002/2017gl074480.

Gasda P.J., Parsons, B., Nellessen, M.A., Crossey, L., Peterson, E., Lanza, N., Yeager, C., Labouriau, A., Wiens, R.C., Clegg, S., 2019, Prebiotic chemistry of borate-bearing clays: a potential Mars biosignature: Carlsbad, New Mexico, Lunar & Planetary Institute, Mars Extant Life: What's Next?, abstract 5034.

Georgelin, T., Jaber, M., Fournier, F., Laurent, G., Costa-Torro, F., Maurel, M.-C., Lambert, J.-F., 2015. Stabilization of ribofuranose by a mineral surface. Carbohydrate Research 402, 241–244. Doi:10.1016/j.carres.2014.07.018.

Goldberg, S., Forster, H. S., & Heick, E. L., 1993, Boron Adsorption Mechanisms on Oxides, Clay Minerals, and Soils Inferred from Ionic Strength Effects. *Soil Science Society of America Journal*, *57*(3), 704. https://doi.org/10.2136/sssaj1993.03615995005700030013x

Goldberg, S., Forster, H.S., Lesch, S.M., and Heick, E.L., 1996, Influence Of Anion Competition On Boron Adsorption By Clays And Soils: Soil Science, v. 161, p. 99–103, doi: 10.1097/00010694-199602000-00003.

Goldberg, S., 1997, Reactions of boron with soils. *Plant and Soil*, *193*(1), 35–48. https://doi.org/10.1023/A:1004203723343

Goldberg, S., Suarez, D. L., & Shouse, P. J., 2008, INFLUENCE OF SOIL SOLUTION SALINITY ON BORON ADSORPTION BY SOILS: *Soil Science*, *173*(6), 368–374. https://doi.org/10.1097/SS.0b013e3181773a0e

Grew, E.S., Bada, J.L., Hazen, R.M., 2011. Borate Minerals and Origin of the RNA World. Origins of Life and Evolution of Biospheres 41, 307–316. doi:10.1007/s11084-010-9233-y.

Grotzinger, J.P., Crisp, J., Vasavada, A.R., Anderson, R.C., Baker, C.J., Barry, R., Blake, D.F., Conrad, P., Edgett, K.S., Ferdowski, B., Gellert, R., Gilbert, J.B., Golombek, M., Gómez-Elvira, J., et al., 2012, Mars Science Laboratory Mission and Science Investigation: Mars Science Laboratory, p. 5–56, doi: 10.1007/978-1-4614-6339-9_3.

Grotzinger, J.P., Sumner, D.Y., Kah, L.C., Stack, K., Gupta, S., Edgar, L., Rubin, D., Lewis, K., Schieber, J., Mangold, N., Milliken, R., Conrad, P.G., Des Marais, D., Farmer, J., et al.,

2014, A Habitable Fluvio-Lacustrine Environment at Yellowknife Bay, Gale Crater, Mars: Science, v. 343, doi:10.1126/science.1242777.

Halim, M., Majumder, R., Nessa, S., Hiroshiro, Y., Sasaki, K., Saha, B., Saepuloh, A., and Jinno, K., 2010, Evaluation of processes controlling the geochemical constituents in deep groundwater in Bangladesh: Spatial variability on arsenic and boron enrichment: Journal of Hazardous Materials, v. 180, p. 50–62, doi: 10.1016/j.jhazmat.2010.01.008.

Harder, H., 1970, Boron content of sediments as a tool in facies analysis. *Sedimentary Geology*, *4*(1–2), 153–175. https://doi.org/10.1016/0037-0738(70)90009-6

Hashizume, H., 2015. Adsorption of Nucleic Acid Bases, Ribose, and Phosphate by Some Clay Minerals. Life 5, 637–650. doi:10.3390/life5010637.

Horgan, B. H. N., Anderson, R. B., Dromart, G., Amador, E. S., & Rice, M. S., 2020, The mineral diversity of Jezero crater: Evidence for possible lacustrine carbonates on Mars. *Icarus*, *339*, 113526. https://doi.org/10.1016/j.icarus.2019.113526

Hynek, B. M., Osterloo, M. K., & Kierein-Young, K. S., 2015, Late-stage formation of Martian chloride salts through ponding and evaporation. *Geology*, *43*(9), 787–790. https://doi.org/10.1130/G36895.1

Ishikawa, T., and Nakamura, E., 1992, Boron isotope geochemistry of the oceanic crust from DSDP/ODP Hole 504B: Geochimica et Cosmochimica Acta, v. 56, p. 1633–1639, doi: 10.1016/0016-7037(92)90230-g.

Karahan, S., Yurdakoç, M., Seki, Y., Yurdakoç, K., 2006. Removal of boron from aqueous solution by clays and modified clays. Journal of Colloid and Interface Science 293, 36–42. Doi:10.1016/j.jcis.2005.06.048.

Kasemann, S.A., Meixner, A., Erzinger, J., Viramonte, J.G., Alonso, R.N., and Franz, G., 2004, Boron isotope composition of geothermal fluids and borate minerals from salar deposits (central Andes/NW Argentina): Journal of South American Earth Sciences, v. 16, p. 685–697, doi: 10.1016/j.jsames.2003.12.004.

Keeling, J.L., 2000, Geology and Characterization of Two Hydrothermal Nontronites from Weathered Metamorphic Rocks at the Uley Graphite Mine, South Australia: Clays and Clay Minerals, v. 48, p. 537–548, doi: 10.1346/ccmn.2000.0480506.

Keren, R., 1981. Boron Adsorption by Clay Minerals Using a Phenomenological Equation1. Clays and Clay Minerals 29, 198–204. Doi:10.1346/ccmn.1981.0290305.

Keren, R., Grossl, P.R., Sparks, D.L., 1994. Equilibrium and Kinetics of Borate Adsorption-Desorption on Pyrophyllite in Aqueous Suspensions. Soil Science Society of America Journal 58, 1116. Doi:10.2136/sssaj1994.03615995005800040016x.

Larralde, R., Robertson, M.P., Miller, S.L., 1995. Rates of decomposition of ribose and other sugars: implications for chemical evolution. Proceedings of the National Academy of Sciences 92, 8158–8160. Doi:10.1073/pnas.92.18.8158.

Lowenstein, T.K., Li, J., Brown, C., Roberts, S.M., Ku, T.-L., Luo, S., and Yang, W., 1999, 200 k.y. paleoclimate record from Death Valley salt core: Geology, v. 27, p. 3, doi: 10.1130/0091-7613(1999)0272.3.co;2.

Martin, T.D., Creed, J.T., and Brockhoff, C.A., 1996, Sample Preparation Procedure For Spectrochemical Determination Of Total Recoverable Elements: Methods for the Determination of Metals in Environmental Samples, p. 12–23, doi: 10.1016/b978-0-8155-1398-8.50008-2.

Maurice, S., Wiens, R.C., Saccoccio, M., Barraclough, B., Gasnault, O., Forni, O., Mangold, N., Baratoux, D., Bender, S., Berger, G., Bernardin, J., Berthé, M., Bridges, N., Blaney, D., et al., 2012, The ChemCam Instrument Suite on the Mars Science Laboratory (MSL) Rover: Science Objectives and Mast Unit Description: Mars Science Laboratory, p. 95–166, doi: 10.1007/978-1-4614-6339-9_6.

Milliken, R.E., Grotzinger, J.P., and Thomson, B.J., 2010, Paleoclimate of Mars as captured by the stratigraphic record in Gale Crater: Geophysical Research Letters, v. 37, doi: 10.1029/2009gl041870.

Mohan, M.R., Kamber, B.S., and Piercey, S.J., 2008, Boron and arsenic in highly evolved Archean felsic rocks: Implications for Archean subduction processes: Earth and Planetary Science Letters, v. 274, p. 479–488, doi: 10.1016/j.epsl.2008.07.042.

Moore, D.M., and Reynolds, R.C., 1997, X-ray diffraction and identification and analysis of clay minerals: Oxford …, Oxford University Press.

Molecular Investigation of Sulfate Complexation in Solution and on Fe-Oxide Surfaces Princeton University, http://geoweb.princeton.edu/research/geochemistry/research/aqueous-sulfate.html (accessed June 2020).

Morris, R.V., Vaniman, D.T., Blake, D.F., Gellert, R., Chipera, S.J., Rampe, E.B., Ming, D.W., Morrison, S.M., Downs, R.T., Treiman, A.H., Yen, A.S., Grotzinger, J.P., Achilles, C.N., Bristow, T.F., et al., 2016, Silicic volcanism on Mars evidenced by tridymite in high-SiO2 sedimentary rock at Gale crater: Proceedings of the National Academy of Sciences, v. 113, p. 7071–7076, doi: 10.1073/pnas.1607098113.

Morrison, S.M., Downs, R.T., Blake, D.F., Vaniman, D.T., Ming, D.W., Hazen, R.M., Treiman, A.H., Achilles, C.N., Yen, A.S., Morris, R.V., Rampe, E.B., Bristow, T.F., Chipera, S.J., Sarrazin, P.C., et al., 2018, Crystal chemistry of Martian minerals from Bradbury Landing through Naukluft Plateau, Gale crater, Mars: American Mineralogist, v. 103, p. 857–871, doi: 10.2138/am-2018-6124.

Nachon, M., Clegg, S.M., Mangold, N., Schröder, S., Kah, L.C., Dromart, G., Ollila, A., Johnson, J.R., Oehler, D.Z., Bridges, J.C., Mouélic, S.L., Forni, O., Wiens, R., Anderson, R.B., et al., 2014, Calcium sulfate veins characterized by ChemCam/Curiosity at Gale crater, Mars: Journal of Geophysical Research: Planets, v. 119, p. 1991–2016, doi: 10.1002/2013je004588.

Nachon, M., Mangold, N., Forni, O., Kah, L., Cousin, A., Wiens, R., Anderson, R., Blaney, D., Blank, J., Calef, F., Clegg, S., Fabre, C., Fisk, M., Gasnault, O., et al., 2017, Chemistry of diagenetic features analyzed by ChemCam at Pahrump Hills, Gale crater, Mars: Icarus, v. 281, p. 121–136, doi: 10.1016/j.icarus.2016.08.026.

Newsom, H.E., Mangold, N., Kah, L.C., Williams, J.M., Arvidson, R.R., Stein, N., Ollila, A.M., Bridges, J.C., Schwenzer, S.P., King, P.L., Grant, J.A., Pinet, P., Bridges, N.T., Calef, F., et al., 2015, Gale crater and impact processes – Curiosity's first 364 Sols on Mars: Icarus, v. 249, p. 108–128.

Okay, O., Güçlü, H., Soner, E., Balkaş, T., 1985. Boron pollution in the Simav River, Turkey and various methods of boron removal. Water Research 19, 857–862. doi:10.1016/0043-1354(85)90143-5.

Osterloo, M. M., Hamilton, V. E., Bandfield, J. L., Glotch, T. D., Baldridge, A. M., Christensen, P. R., et al., 2008. Chloride-Bearing Materials in the Southern Highlands of Mars. *Science*, *319*(5870), 1651–1654. https://doi.org/10.1126/science.1150690

Osterloo, M. M., Anderson, F. S., Hamilton, V. E., & Hynek, B. M., 2010. Geologic context of proposed chloride-bearing materials on Mars. *Journal of Geophysical Research*, *115*(E10). https://doi.org/10.1029/2010JE003613

Pawar, A.L., 2010, Seasonal Variation in Physicochemical quality of Lonar Lake Water: Journal of Chemical and Pharmaceutical Research, v. 2, p. 225–231.

Payre, V., Siebach, K.L., Dasgupta, R., Udry, A., Rampe, E.B., and Morrison, S.M., 2020, Investigation of Magmatic Activities on Early Mars Using Igneous Mineral Chemistry in Gale Crater, Mars: NASA Technical Reports Server.

Perry, E. A., 1972. Diagenesis and the validity of the boron paleosalinity technique. *American Journal of Science*, *272*, 150–160.

Poppe, L., Paskevich, V., Hathaway, J., and Blackwood, D., 2001, A laboratory manual for X-ray powder diffraction: Open-File Report, doi: 10.3133/ofr0141.

Pytte, A.M., and Reynolds, R.C., 1989, The Thermal Transformation of Smectite to Illite: Thermal History of Sedimentary Basins, p. 133–140, doi: 10.1007/978-1-4612-3492-0_8.

Rampe, E., Ming, D., Blake, D., Bristow, T., Chipera, S., Grotzinger, J., Morris, R., Morrison, S., Vaniman, D., Yen, A., Achilles, C., Craig, P., Marais, D.D., Downs, R., et al., 2017, Mineralogy of an ancient lacustrine mudstone succession from the Murray formation, Gale crater, Mars: Earth and Planetary Science Letters, v. 471, p. 172–185, doi: 10.1016/j.epsl.2017.04.021.

Rampe, E.B., Bristow, T.F., Blake, D.F., Vaniman, D.T., Morrison, S.M., Ming, D.W., Morris, R.V., Achilles, C.N., Chipera, S.J., and Downs, R.T., 2019, New Perspectives of Ancient Mars: Mineral Diversity and Crystal Chemistry at Gale Crater, Mars from the CheMin X-Ray Diffractometer: NASA Technical Reports Server.

Rapin, W., Ehlmann, B.L., Dromart, G., Schieber, J., Thomas, N.H., Fischer, W.W., Fox, V.K., Stein, N.T., Nachon, M., Clark, B.C., Kah, L.C., Thompson, L., Meyer, H.A., Gabriel, T.S.J., et al., 2019, An interval of high salinity in ancient Gale crater lake on Mars: Nature Geoscience, v. 12, p. 889–895, doi: 10.1038/s41561-019-0458-8.

Ricardo, A., 2004, Borate Minerals Stabilize Ribose: Science, v. 303, p. 196–196, doi: 10.1126/science.1092464.

Sautter, V., Payré, V., Paratoux, D., Toplis, M., Cousin, A., Bouley, S., Beck, P., and Krämer Rugiu, L., 2019, Remanan of Early Noachian Crust on Mars from Martian Meteorites, In Situ and Remote Sensing Data: Ninth International Conference on Mars, LPI Contribution No. 2089, id.6020.

Schott, J., Kretzschmar, J., Acker, M., Eidner, S., Kumke, M.U., Drobot, B., Barkleit, A., Taut, S., Brendler, V., and Stumpf, T., 2014, Formation of a Eu(iii) borate solid species from a weak Eu(iii) borate complex in aqueous solution: Dalton Trans., v. 43, p. 11516–11528, doi: 10.1039/c4dt00843j.

Schwenzer, S., Abramov, O., Allen, C., Bridges, J., Clifford, S., Filiberto, J., Kring, D., Lasue, J., Mcgovern, P., Newsom, H., Treiman, A., Vaniman, D., Wiens, R., and Wittmann, A., 2012, Gale Crater: Formation and post-impact hydrous environments: Planetary and Space Science, v. 70, p. 84–95, doi: 10.1016/j.pss.2012.05.014.

Schwenzer, S.P., Bridges, J.C., Wiens, R.C., Conrad, P.G., Kelley, S.P., Leveille, R., Mangold, N., Martín-Torres, J., Mcadam, A., Newsom, H., Zorzano, M.P., Rapin, W., Spray, J., Treiman, A.H., et al., 2016, Fluids during diagenesis and sulfate vein formation in sediments at Gale crater, Mars: Meteoritics & Planetary Science, v. 51, p. 2175–2202, doi: 10.1111/maps.12668.

Scorei, R., Cimpoiaşu, V.M., 2006. Boron Enhances the Thermostability of Carbohydrates. Origins of Life and Evolution of Biospheres 36, 1–11. doi:10.1007/s11084-005-0562-1.

Scorei, R., 2012, Is Boron a Prebiotic Element? A Mini-review of the Essentiality of Boron for the Appearance of Life on Earth: Origins of Life and Evolution of Biospheres, v. 42, p. 3–17, doi: 10.1007/s11084-012-9269-2.

Smith, G.I., 1979, Subsurface Stratigraphy and Geochemistry of Late Quaternary Evaporites, Searles Lake, California: Geological Survey Professional Paper, v. 1043.

Spivack, A., and Edmond, J., 1987, Boron isotope exchange between seawater and the oceanic crust: Geochimica et Cosmochimica Acta, v. 51, p. 1033–1043, doi: 10.1016/0016-7037(87)90198-0.

Spivack, A. J., Palmer, M. R., & Edmond, J. M., 1987. The sedimentary cycle of the boron isotopes. *Geochimica et Cosmochimica Acta*, *51*(7), 1939–1949. https://doi.org/10.1016/0016-7037(87)90183-9

Swadling, J.B., Coveney, P.V., Greenwell, H.C., 2010. Clay Minerals Mediate Folding and Regioselective Interactions of RNA: A Large-Scale Atomistic Simulation Study. Journal of the American Chemical Society 132, 13750–13764. doi:10.1021/ja104106y.

Tanner, L.H., 2002, Borate formation in a perennial lacustrine setting: Miocene–Pliocene Furnace Creek Formation, Death Valley, California, USA: Sedimentary Geology, v. 148, p. 259–273, doi: 10.1016/s0037-0738(01)00221-4.

Treiman, A. H., Morris, R. V., Agresti, D. G., Graff, T. G., Achilles, C. N., Rampe, E. B., et al., 2014. Ferrian saponite from the Santa Monica Mountains (California, U.S.A., Earth): Characterization as an analog for clay minerals on Mars with application to Yellowknife Bay in Gale Crater. *American Mineralogist*, *99*(11–12), 2234–2250. https://doi.org/10.2138/am-2014-4763

Vaniman, D., Dyar, M.D., Wiens, R., Ollila, A., Lanza, N., Lasue, J., Rhodes, J.M., Clegg, S., and Newsom, H., 2012, Ceramic ChemCam Calibration Targets on Mars Science Laboratory: Space Science Reviews, v. 170, p. 229–255, doi: 10.1007/s11214-012-9886-0.

Vaniman, D.T., Bish, D.L., Ming, D.W., Bristow, T.F., Morris, R.V., Blake, D.F., Chipera, S.J., Morrison, S.M., Treiman, A.H., Rampe, E.B., Rice, M., Achilles, C.N., Grotzinger, J.P., McLennan, S.M., et al., 2014, Mineralogy of a Mudstone at Yellowknife Bay, Gale Crater, Mars: Science, v. 343, doi: 10.1126/science.1243480.

Wiens, R.C., Maurice, S., Barraclough, B., Saccoccio, M., Barkley, W.C., Bell, J.F., Bender, S., Bernardin, J., Blaney, D., Blank, J., Bouyé, M., Bridges, N., Bultman, N., Caïs, P., et al., 2012, The ChemCam Instrument Suite on the Mars Science Laboratory (MSL) Rover: Body Unit and Combined System Tests: Mars Science Laboratory, p. 167–227, doi: 10.1007/978-1-4614-6339-9_7.

Williams, L. B., Hervig, R. L., Holloway, J. R., & Hutcheon, I., 2001. Boron isotope geochemistry during diagenesis. Part I. Experimental determination of fractionation during illitization of smectite. *Geochimica et Cosmochimica Acta*, *65*(11), 1769–1782. https://doi.org/10.1016/S0016-7037(01)00557-9

Yingkai, X., & Lan, W., 2001. The effect of pH and temperature on the isotopic fractionation of boron between saline brine and sediments. *Chemical Geology*, *171*, 253–261.

You, C.-F., Spivack, A. J., Gieskes, J. M., Martin, J. B., & Davisson, M. L., 1996. Boron contents and isotopic compositions in pore waters: a new approach to determine temperature induced artifacts—geochemical implications. *Marine Geology*, *129*(3–4), 351–361. https://doi.org/10.1016/0025-3227(96)83353-6